Impact of aerosols on cloud and precipitation in the Amazon

Dissertation

zur Erlangung des Grades

‘Doktor rerum naturalium (Dr. rer. nat.)’

im Promotionsfach Chemie

am Fachbereich Chemie, Pharmazie, Geographie und Geowissenschaften

der Johannes Gutenberg-Universität in Mainz

Lixia Liu

geb. in Shandong, China

Mainz, March 2021

1. Berichterstatter: Prof. Dr. Ulrich Pöschl

2. Berichterstatter: Prof. Dr. Thorsten Hoffmann

Tag der mündlichen Prüfung: May 20th, 2021

I hereby declare that I wrote the dissertation submitted without any unauthorized external assistance and used only sources acknowledged in the work. All textual passages which are appropriated verbatim or paraphrased from published and unpublished texts as well as all information obtained from oral sources are duly indicated and listed in accordance with bibliographical rules. In carrying out this research, I complied with the rules of standard scientific practice as formulated in the statutes of Johannes Gutenberg University Mainz to insure standard scientific practice.

Abstract

Clouds and precipitation play crucial roles in the radiation balance and hydrological cycle on the Earth. Their properties can be changed by atmospheric aerosols through aerosol-radiation interactions (ARIs) and aerosol-cloud interactions (ACIs). The understanding of how and to what extent aerosols can modify clouds and precipitation is important for weather and climate prediction, yet it still has large uncertainty. This dissertation investigates the role of aerosols in shaping the cloud and precipitation in the Amazon during the dry season using an online coupled meteorology-chemistry model, WRF-Chem, based on which deeper insights are gained concerning the individual and joint effects of ARIs and ACIs on the clouds and precipitation from cloud microphysical to regional scales.

A comprehensive assessment was first made for the impacts of biomass burning (BB) aerosols, the most important aerosol component recognized in the Amazon during the dry season, on the Amazon clouds and precipitation through ARIs and ACIs and their sensitivity to the inter-annual variations of BB aerosol emissions. The ARIs of BB aerosols tend to suppress low-level liquid clouds by local warming and increased evaporation and to facilitate the formation of high-level ice clouds by enhancing updrafts and condensation at high altitudes. In contrast, the ACIs of BB aerosol particles tend to enhance the formation and lifetime of low-level liquid clouds by providing more cloud condensation nuclei (CCN) and to suppress the formation of high-level ice clouds by reducing updrafts and condensable water vapor at high altitudes (> 8 km). For scenarios representing the lower and upper limits of BB emission estimates for recent years (2002–2016), total regional BB aerosol radiative forcings of –0.2 and 1.5 W m^{-2} were obtained, respectively, showing that the influence of BB aerosols on the regional energy balance can range from modest cooling to strong warming. ACIs dominate at low BB emission rates and low aerosol optical depth (AOD), leading to an increased cloud liquid water path (LWP) and negative radiative forcing, whereas ARIs dominate at high BB

emission rates and high AOD, leading to a reduction of LWP and positive radiative forcing. In all scenarios, BB aerosols led to a decrease in the frequency of occurrence and rate of precipitation, caused primarily by ACI effects at low aerosol loading and by ARI effects at high aerosol loading. The dependence of precipitation reduction on BB aerosol loading is greater in a strong convective regime than under weakly convective conditions. Overall, the results show that ACIs tend to saturate at high aerosol loading, whereas the strength of ARIs continues to increase and plays a more important role in highly polluted conditions.

As the ARI effect of BB aerosols can be significant in modulating the clouds and precipitation in the Amazon, in the second part of this dissertation, a process analysis study for the biomass burning episodes in 2010 and 2012 was conducted to advance the understanding of the ARI effect on precipitation from a macrophysical scale to a cloud microphysical scale. A microphysical process analysis module was developed and implemented into the Lin et al. microphysical scheme in WRF-Chem, which shows that the microphysical processes of raindrops accreting cloud droplets (RAW) and graupel melting (GMT) explain the ARI-induced rain production change by 73% and 16%, respectively, different from the dominant process of collision-coalescence in the ACI effect. The ARIs can significantly modulate the precipitation evolution in a diurnal lifecycle of the locally generated convective system, inhibiting the precipitation initially while enhancing it later, causing a reduction in the amplitude of diurnal precipitation by up to 43%. The opposite ARI effects at the two stages were governed by distinct microphysical process responses rooted in atmospheric thermodynamic and dynamic changes. The warm rain process RAW dominates the former stage, whereas the cold rain processes including graupel accreting cloud droplets (GAW), graupel accreting snow (GAS), ice to snow transformation through Bergeron process (SFI), and GMT, and the warm rain process RAW almost equally contribute to the latter stage.

Moreover, the uncertainty in simulating aerosol itself will translate into the uncertainty of simulating aerosol-radiation-cloud interations. As secondary organic aerosols (SOAs) lead to a large amount of CCN in the Amazon upper troposphere (UT), the WRF-Chem deficiency in simulating the upper tropospheric CCN due to the uncertainty in the SOA treatment limits its accurate representation of ACIs. An attempt to improve the simulation of SOA-dominated CCN in the UT was made for the MOSAIC aerosol module coupled with the CRIMECH gas-phase module in WRF-Chem. Newly developed modules of the organic nucleation induced by highly oxygenated molecules (HOMs) and the condensation of low volatile organic compounds (LVOCs) were incorporated into WRF-Chem, based on which simulations were conducted in September–October 2014 over the Amazon, and were evaluated in terms of the aerosol number and mass concentrations and their vertical distribution against aircraft measurements during the ACRIDICON-CHUVA campaign. The newly developed modules significantly improve the underestimation of the CCN at 0.52% supersaturation and organic aerosol (OA) mass in the UT in the default WRF-Chem while maintains an observation-comparable CN concentration simulated in the default WRF-Chem. The organic condensation of LVOC improves the CCN concentration in the UT in the default WRF-Chem by about 90%. The HOMs-induced organic nucleation provides additional new particles aside from the existing H_2SO_4-H_2O binary nucleation mechanism, and leads to an improvement of over 50% and 14% in the CN and CCN number concentration in the UT under the condition of sufficient particle growth. Deep convection controls the occurrence of HOMs production in the UT by controlling the transport of biogenic organic vapors to the UT. The significant temperature effect on the HOMs-induced nucleation rate favors a high organic nucleation rate in the UT. The intensity of condensation of LVOC is sensitive to the assumption of the LVOC yield. A temperature dependant correction on the bulk assumption of LVOC yield based on laboratory experiments is suggested to better reproduce the observed organic aerosol mass.

Contents

Chapter 1 Introduction

Atmospheric aerosols play a significant role in modifying the weather and climate on the Earth. The understanding of the aerosol effect on weather and climate is essential and urgent for the prediction and mitigation of future climate change by human beings. In this context, how and to what extent cloud and precipitation are influenced by aerosols are the key questions as cloud and precipitation are crucial branches of the hydrological cycle and energy balance of the Earth-Atmosphere system.

However, the aerosol effect on cloud and precipitation are still far from being well understood that it constitutes the largest uncertainty in aerosol climate effect assessment (IPCC, 2013). A thorough understanding of the aerosol effect is challenging because of the complexity of the aerosol-cloud-precipitation system and the complicate matrix of the spatially and temporally varying aerosols and wide range of cloud regimes.

The dry season in the Amazon features an annual lowest rainfall amount and highest aerosol loading; the precipitation scarcity and potentially strong aerosol impact necessitate an investigation of the cloud and precipitation responses to aerosols in this period. Motivated by all the above, this PhD research focuses on the aerosol impact on cloud and precipitation formation in the Amazon region during the dry season. Specifically, the responses of cloud and precipitation to aerosols are explored and quantified from cloud process scale to regional scale based on an online coupled meteorology-chemistry model, and improvement for model representation of aerosol-cloud interactions has been made for this region.

1.1 Atmospheric aerosols

Atmospheric aerosols are particles of liquid or solid phase that suspend in the air. They exist with sizes spanning several orders of magnitude, i.e., from nanometer (nm) scale to tens

of micrometers (μm) in diameter, and with varying chemical composition. Aerosol size and chemical composition are important aerosol features for determining their optical and hygroscopic properties that ultimately control the climate effect of aerosols through their interaction with radiation flux and cloud microphysics. For the atmospheric aerosols, their size and chemical characteristics as well as concentration are dependent on their sources, sinks, and dynamic and chemical processes in the atmosphere.

Aerosol size, though spanning several orders of magnitude, is observed in a repetitive manner to be with relatively higher frequency at certain ranges, which are named the 'size modes'. Based on aerosol observations across the globe, aerosol size distribution typically exhibits four size modes: nucleation mode where the particles are less than 0.01 μm in diameter, Aitken mode with particle diameters varying from 0.01 to 0.1 μm, accumulation mode with the aerosol size coverage from 0.1 to 2.5 μm in diameter, and coarse mode in which the particle diameters are larger than 2.5 μm (Seinfeld & Pandis, 2016). The size spans and patterns of these modes are not rigidly fixed but may vary slightly in different conditions. Aerosols in the four modes are generated as a result of different aerosol processes. The nucleation mode contains aerosol particles formed from vapors (e.g., sulfuric acid vapor and low volatile organic compounds) by gas-to-particle conversion. Particles in this mode are susceptible to coagulation scavenging. The Aitken mode aerosols are usually made up of both particles that have grown up from nucleation mode size and particles directly emitted in particle phase, e.g., soot particles from combustion. The accumulation mode emerges due to inefficient atmospheric scavenging including coagulation scavenging and dry and wet deposition in this size range. The growth of Aitken mode aerosols, in-cloud processes, and direct emission are all possible sources for particles in this mode. The coarse mode forms when relatively large particles are emitted directly into the atmosphere from certain sources and mechanical processes, for instance, dust and sea salt particles from wind friction on the desert and ocean surfaces, respectively. The

four modes are of different activity in terms of interacting with radiation and clouds, e.g., aerosols in the accumulation and coarse modes are more efficient to be activated into cloud droplets compared with the finer modes.

Atmospheric aerosols are observed to contain a variety of components, and the most important components globally are seasalt (composed of sodium, chloride), sulfate, nitrate, ammonium, dust, and carbonaceous materials (including black carbon, BC, and organic carbon, OC). The seasalt aerosol occupies a substantial mass fraction but is only distributed over marine areas. Sulfate, nitrate, and ammonium are common over both continents and oceans, with their highest loading over industrialized regions due to the large emissions of their precursors. Sulfate and nitrate aerosols are to a large extent generated from SO_2 and NO_x vapors through gas-to-particle conversion, respectively; while ammonium is usually formed in accompany with them through the neutralizing process. Organic matter is an important contributor to the aerosol mass in a number of continental areas. For example, in boreal and tropical forests, a large amount of organic matter form as biogenic secondary organic aerosols or from biomass burning events; in urban areas with large emission of high-molecular-weight organic vapors (e.g., polycyclic aromatic hydrocarbons), organic aerosol can account for large fraction of the dry aerosol mass (Chow et al., 2002). Black carbon is derived from combustion and distributes mainly at areas with fossil fuel combustion or biomass burning activities. Dust aerosol mainly originates from deserts as a result of wind erosion. The chemical composition plays a crucial role in controlling the optical property and hygroscopicity of aerosols. Black carbon and dust are the only two aerosol types that are acknowledged to be able to both scatter and absorb solar radiation while the rest components can only scatter solar radiation.

The size distribution, chemical properties, and population of atmospheric aerosols are governed by their source and sink mechanisms which are complex and region-dependent across

the globe. Besides, they are modulated by physical and chemical processes they may undergo during aging in the atmosphere.

Atmospheric aerosols originate either directly from natural and anthropogenic emissions (primary aerosols) or from gas-to-particle transformation proceeding in the atmosphere (secondary aerosols). For the primary aerosols, dust and seasalt are the primary species of natural origin (Seinfeld & Pandis, 2006); anthropogenic aerosols associated with open biomass burning, residential and traffic practices, power station, and industrial activities, etc. are mainly composed of sulfate, nitrate, ammonium, and carbonaceous materials (Andreae & Merlet, 2001; Streets et al., 2003). Specifically, for the anthropogenic sources, industrial and urbanization-related aerosol emissions are mainly in the Northern Hemisphere, whereas open biomass burning emission prevails in the tropics and Southern Hemisphere, mainly at the rainforest and savanna areas in the Amazon, Africa, Australia, and Southeast Asia. On the other hand, several secondary aerosol formation mechanisms, i.e., gas-to-particle conversion pathways, have been identified, e.g., new particle formation where low-volatile vapors such as H_2SO_4 and organic components with extremely low volatility nucleate into particle phase (Kulmala, 2003), condensation of gas precursors such as low volatile organic compounds onto existing particles (Calvo et al., 2013), and specific partitioning processes involving chemical reactions such as the in-cloud sulfate formation from sulfur dioxide vapor (Levin & Cotton, 2009). The vapor precursors for the secondary aerosols are also from both natural and anthropogenic sources. In terms of the total aerosol mass (both primary and secondary) on a global scale, the contribution from natural sources substantially exceeds that from the anthropogenic sources (Seinfeld & Pandis, 2016). However, anthropogenic influence on the atmospheric aerosol loading should still be emphasized. That is because, regionally, anthropogenic input of aerosols may take the dominant role, e.g., urban areas in the Northern Hemisphere and the Amazon region during its dry season. Besides, the influence of

anthropogenic activities is beyond the direct emission since the natural aerosol emission is also susceptible to anthropogenic practices, such as land use change (Andreae & Rosenfeld, 2008).

Once airborne, aerosol particles can go through a series of microphysical and chemical processes in the atmosphere, changing their size and chemical properties. Aerosol particles can grow/shrink through condensation/evaporation. For instance, the condensation of low volatile organic compounds onto preexisting aerosols via absorption and adsorption is an important pathway for the secondary organic aerosol formation. Aerosols of the same or different sizes can coagulate with each other, which has no impact on the total aerosol mass in the atmosphere but can substantially influence the aerosol number and size spectrum. The coagulation process serves as a significant depletion for small particles while contributes to the growth of large particles. Aerosol particles, when reaching a certain size determined by the ambient water vapor pressure and the aerosol hygroscopic property, can be activated as cloud condensation nuclei (CCN) and then participate in cloud processes. The CCN number concentration is observed to vary from less than 100 cm^{-3} in remote marine areas to several thousands cm^{-3} in polluted continental regions. Similarly, some types of aerosols such as dust and black carbon are able to act as ice nuclei (IN) and engage in the ice-cloud processes.

Aerosol particles are removed out of the atmosphere through dry and/or wet deposition. Specifically, dry deposition involves processes of gravitational sedimentation, turbulent mixing, and impaction onto the ground and canopy surface; wet deposition includes below-cloud scavenging where aerosols are swept out of the atmosphere by rain, and in-cloud scavenging where aerosols are transformed into cloud droplets after being activated as CCN or IN. The deposition processes largely determine the residence time of aerosols in the troposphere. The lifetime of tropospheric aerosols is days to one week generally (Seinfeld & Pandis, 2006), which is much shorter than the greenhouse gases (several years). Therefore, in contrast to the greenhouse gases that can be distributed uniformly across the globe by

transportation, aerosols emitted at a certain location can only be transported within short range. This feature warrants the regional investigation of aerosol climate effects.

1.2 Aerosol effects on cloud and precipitation

Clouds are a collection of water droplets either in liquid phase or in ice phase. Clouds initially form when air parcels become supersaturated with respect to liquid or ice water droplets (Wallace & Hobbs, 2006). Clouds show different appearance and characteristics according to the ways the supersaturation is reached. Convective clouds occur where the atmospheric stratification is unstable and there is external forcing for air masses to ascend, e.g., the convective clouds driven by surface heating in the tropics, pyro-clouds fed by strong updrafts due to the energy from wildfires, frontal cloud systems induced by dynamic uplift in the stormtracks in the midlatitudes, orographic clouds formed out of the airlifting forced by the earth's topography. These convective cloud systems can reach deeply to the tropopause, involving both liquid and ice droplets. The stratocumulus clouds over the subtropical trade wind regions represent another type of clouds, which are formed under stable atmospheric stratification and self-maintained by the longwave radiative cooling at the cloud top. The stratocumulus clouds are mostly distributed within the lower atmosphere with mainly liquid cloud droplets. In contrast, cirrus clouds are clouds at higher atmosphere and consist solely of ice crystals. They usually form where the cold temperature and moisture sources are enough to generate ice crystals, e.g., contrails and anvils of deep cumulus. Besides this classification, clouds are also commonly categorized according to the phase of the hydrometers within the cloud. For instance, warm clouds consist of only liquid droplets; cold clouds may contain ice crystals; mixed-phase clouds are made of both ice crystals and supercooled water.

To produce precipitation, cloud liquid and ice droplets need to grow to a certain size to transform into precipitating hydrometers, e.g., raindrop, snow, and graupel, and then fall out of the cloud systems. The droplet growth mechanisms for warm clouds mainly include

condensation of water vapor onto activated CCN and collision-coalescence of liquid droplets, and these mechanisms analogously apply to the ice crystal growth in the cold clouds. In mixed-phase clouds, interactions between supercooled water and ice crystals additionally contribute to cloud droplet growth, e.g., the Wegener-Bergeron-Findeisen process by which ice particles promptly gain water mass from supercooled water droplets (Pruppacher & Klett, 2010).

Clouds and precipitation are crucial constituents in the climate system of the Earth, serving as key agents in the radiation transfer and hydrological cycle on the planetary. Clouds affect the radiation budget either by reflecting the incoming solar radiation and therefore reducing the incident radiation on the Earth's surface or by absorbing the outgoing terrestrial radiation and reemitting part of it back to the lower atmosphere. The two processes exert competing effects on the net radiation flux of the Earth-Atmosphere system as the former causes negative radiative forcing while the latter induces positive one. Cloud properties such as amount, optical characteristics, lifetime, and occurring time govern the net radiative effect of clouds. For instance, low clouds tend to act on the solar radiation and cool the climate whereas high clouds are characterized with greenhouse-like effect and warm the climate. The precipitation, as an important factor controlling the cloud microphysics and lifetime, can indirectly influence the radiative effects of clouds. Aside from their roles in radiation transfer, clouds and precipitation govern the atmospheric branch of the hydrological cycle and transport the moisture from the atmosphere to the Earth's surface.

Aerosols influence clouds and precipitation through manifold complex processes, which have been generally categorized into two bulk mechanisms: aerosol-radiation interactions (ARIs) and aerosol-cloud interactions (ACIs; IPCC, 2013).

1.2.1 Aerosol-radiation interactions

Aerosol particles interact with radiation by scattering and/or absorbing solar radiation and terrestrial radiation. The capability of absorbing solar radiation is determined by aerosol

optical property. In the atmosphere, black carbon and mineral dust are the only species that have been identified as light-absorbing aerosols–aerosols that are able to both scatter and absorb solar radiation; the other aerosol components do not absorb solar radiation and are categorized into light-scattering aerosols. The interactions between aerosol and radiation can impact the Earth's climate. Specifically, the light-scattering aerosols scatter solar radiation, cause a negative radiative forcing to the climate, and therefore cool the Earth-Atmosphere system. By contrast, light-absorbing aerosols, though also scatter solar radiation as the light-scattering aerosols do, can meantime absorb solar radiation and warm the atmosphere. The net radiative forcing of light-absorbing aerosols on the Earth-Atmosphere system is an outcome of the two competing effects, which has been estimated to be near zero globally but considerably large in some regions (Ramanathan & Carmichael, 2008).

Such global climate cooling or warming induced by aerosols corresponding to their optical properties can exert systematic long-term influence on clouds and precipitation. Aside from this, some short-term mechanisms could cause fast and more intensive modifications on cloud systems. As mentioned above, light-absorbing aerosols can effectively absorb incident shortwave radiation and therefore heat the air layer they reside in, enhancing the evaporation of clouds (the 'semi-direct' effect; Hansen et al., 1997). Besides, both light-absorbing and light-scattering aerosols can reduce the incident shortwave radiation reaching the surface, causing less sensible and latent heat flux from the surface to the atmosphere. With less convective driving force and moisture supply, clouds can be suppressed from forming and developing (Feingold et al., 2005). Moreover, aerosols can alter the atmospheric temperature stratification, change the thermodynamic stability, and hence influence cloud development (Saide et al., 2015). Additionally, spatially different radiation responses due to inhomogeneously distributed aerosols can affect the horizontal temperature gradient, the air convergence/divergence, and therefore the convective cloud formation (Grant & van den Heever, 2014).

The effect of aerosol-radiation interactions on cloud and precipitation is complicated due to its sensitivity to a number of factors. Firstly, individual atmospheric aerosol particles usually contain a mixture of light-scattering and light-absorbing substances, and the overall optical properties depend on the way the two materials mix. For the ambient aerosols, their size distribution and total concentration are also determinants of aerosol-radiation interactions. As measures of the column integrated optical characteristics, the aerosol optical depth (AOD) is commonly used to illustrate the radiation extinction capability of aerosols and the single scattering albedo (SSA) is usually adopted to represent the absorbing-to-extinction ratio. Aside from the optical properties of aerosols themselves, environmental factors play a vital role in aerosol-radiation interactions, influencing the magnitude and even the sign of the resultant radiative forcing. Such environmental factors include the solar angle, the underlying albedo, as well as the relative vertical position of aerosol layers and clouds. The effect of aerosol-radiation interactions on cloud and precipitation formation, though comparably important, is not documented as extensively as the aerosol-cloud interactions, and the study on this field is at a relatively beginning stage waiting for more investigations to advance it.

1.2.2 Aerosol-cloud interactions

Another important pathway for aerosols affecting clouds and precipitation is aerosol-cloud interactions, where aerosols act as CCN or IN, modify cloud microphysics, and impact the cloud properties such as cloud albedo and lifetime (IPCC, 2013). Meanwhile, dynamical feedbacks to the aerosol-induced cloud microphysical perturbation may lead to further adjustments in clouds and precipitation (Rosenfeld et al., 2008).

In the atmosphere, the presence of aerosols is necessary for cloud formation. It is of little possibility in the real atmosphere that pure water vapor homogeneously nucleates into liquid droplets or ice crystals which can grow spontaneously, because the required supersaturation for homogeneous nucleation is too high to be achieved in the ambient

conditions. However, the presence of aerosol particles is effective at lowering the energy barriers for the formation of liquid droplets or ice crystals (Köhler, 1936). The potential capability of an aerosol particle being activated as a CCN is defined by its size and hygroscopicity. Specifically, lower supersaturation is required for the activation of particles with larger size and higher hygroscopicity (Köhler, 1936). On the other hand, aerosols facilitate ice crystal formation by serving as IN. By now, it remains unclear regarding the aerosol species and mechanisms that lead to IN production. Some physical processes responsible for aerosols becoming IN include: deposition nucleation where the water vapor pressure in the air reaches the supersaturation with respect to ice over the particle surface and then deposits onto the aerosol particle; contact nucleation where aerosol particles contact with liquid cloud droplets and cause the latter to freeze at temperatures higher than –38 °C; freezing nucleation where aerosol particles already existing in the liquid cloud droplets cause the droplets to freeze at temperatures higher than –38 °C (Wallace & Hobbs, 2006). Only particles of specific types can act as IN due to their special structure characteristics such as crystalline structure. Mineral dust, soot, and some primary biological aerosols have been found with the ability to work as IN (Hoose & Mohler, 2012; Pöschl et al., 2010).

Based on the two basic functions (CCN and IN) aerosols act in the cloud, several mechanisms for the influence of ACIs on cloud and precipitation have been proposed. Firstly, the addition of aerosols into a cloud can lead to more and smaller cloud liquid droplets. The modification on the cloud microphysics results in increased cloud albedo, less solar radiation on the surface and in the atmosphere, and hence a cooler climate system (Twomey, 1977). Meanwhile, the smaller cloud droplets due to increased aerosol concentration slow down their transformation to raindrops and therefore the precipitation efficiency is reduced while the cloud lifetime is prolonged (Albrecht, 1989). As a subsequent stage of the precipitation inhibition, invigoration of convection and precipitation by aerosols can occur because the smaller cloud

droplets in larger numbers are easier to be lifted to high altitudes and the accompanied latent heat release can promote the convection development (Rosenfeld et al., 2008). For cold clouds such as cirrus clouds, the addition of IN would result in larger numbers of smaller ice crystals so that the cloud optical properties are changed accordingly (Krishnakumar et al., 2011).

Despite these physically based mechanisms, the effects of ACIs on cloud and precipitation are not straightforward due to complex atmospheric processes and feedbacks at different scales and their sensitivity to environmental factors. Studies of the aerosol-cloud interactions have shown results that diverge not only in the magnitude but also in the sign of the response of cloud and precipitation properties, e.g., the precipitation response (Guo et al., 2014; Kogan et al., 2012; Planche et al., 2010; Tao et al., 2012; Teller & Levin, 2006), the cloud lifetime response (Jiang & Feingold, 2006; Kaufman et al., 2005; Norris, 2001), and even the cloud albedo response (Chameides et al., 2002; Twohy et al., 2005). Hence, accurate model representations of the cloud and aerosol processes and cloud regime-based studies are needed to lower the uncertainties in qualitatively understanding and quantitatively assessing the ACIs.

In summary, the aerosol effects on cloud and precipitation either by ARIs or by ACIs are still highly uncertain in terms of both mechanisms and quantitative assessment. In the context of practically improving the understanding, modeling simulations combined with observations are needed. Particularly, the regional modeling studies based on advanced atmosphere-chemistry models are essential. On one hand, the aerosol-radiation-cloud-precipitation system in the atmosphere is more complex than an ideally designed single cloud in simplified cloud models such as box models and 2-D cloud models and the simplification could cause uncertainty to these model results. On the other hand, the dependence of the ACI and ARI on so many factors such as cloud categories (Khain et al., 2005), meteorological conditions (Fan et al., 2009; Khain et al., 2005), as well as aerosol properties (Chang et al., 2015) makes the scientific question of aerosol impact on cloud and precipitation a complex

matrix. An overall global examination could not reveal the regionally dependent characteristics; moreover, an accurate representation of the atmospheric processes in a global model requires huge computing resources that cannot be achieved now. Hence, regional studies, especially fine-resolution simulations by advanced models, are desired to get deep insights into the aerosol effects on cloud and precipitation and to provide relatively more accurate assessments for the specific regions (Stevens & Feingold, 2009).

1.3 Aerosols, cloud, and precipitation in the Amazon during the dry season

The Amazon basin, located in the tropical area, is of vital importance in the global climate system. This region, working as a part of the tropical band, absorbs the largest amount of solar radiation on the globe and drives the global atmospheric circulation (Nobre et al., 2009). The Amazon river embedded in it contributes significantly to the global hydrological cycle as ~17% of global freshwater is discharged into the ocean by it (Dai & Trenberth, 2002). The rainforest and soils in the Amazon are estimated to have a substantial storage of carbon (Malhi et al., 2006), which considerably govern the CO_2 concentration and may potentially influence the global warming. The cloud and precipitation in this region significantly influence the radiation transfer, hydrological balance, and the vegetation there. The resilience of the Amazon cloud and precipitation to forcings from human activities, e.g., aerosol emission, is therefore of great concern. Especially in the dry season when the humidity is relatively low, the sensitivity of the ecosystem there to the rainfall from cloud systems is more accentuated. Aside from regional influence, changes in the cloud and precipitation properties in the Amazon Basin can cause significant large-scale or remote atmospheric perturbation, e.g., mitigation of the Intertropical Convergence Zone (ITCZ; Wang & Fu, 2002), due to the interactions between regional climate and large-scale atmospheric circulation.

1.3.1 Aerosol sources

Aerosols in the Amazon basin exhibit distinctive characteristics for the wet and dry seasons. In the wet season, the particle concentration is as low as that over the remote areas (Andreae, 2009). By contrast, the dry season features remarkably high particle concentration, generally 500–2000 cm^{-3} based on long-term observation, being an order of magnitude higher than that in the wet season (Andreae et al., 2015). During the dry season, aerosols in the Amazon originate from several sources. Biomass burning, as a primary aerosol emission source, is significant for the aerosol population in this region. Other minor primary aerosol sources include traffic and industry in cities within this region (Kuhn et al., 2010), canopy-emitted primary biological aerosols such as pollen, bacteria, and fungal (Elbert et al., 2007), and episodic aerosol influx by long-range transport, mainly including dust, biomass burning, and volcanic particles from the African continent (Martin et al., 2010; Pöhlker et al., 2018). In addition to the primary aerosol sources, the secondary organic aerosol (SOA) originated from the biogenic organic vapors plays a considerable role in the aerosol population, causing the aerosol concentration in the upper troposphere to be as high as that near the surface (Andreae et al., 2018).

The biomass burning aerosol emission in the Amazon accounts for a subsitaintial fraction of the global sum (Wiedinmyer et al., 2011). Biomass burning causes drastic aerosol concentration increase in the dry season in the Amazon and is the most important aerosol source for vast areas within the region, especially for those near the fire spots (Tegen et al., 1997). Biomass burning activities in the Amazon are performed at the forest- and savanna-covered areas mainly for agricultural practices (Andreae et al., 2002), with the majority of the biomass burning events being carried out at the edge of the Amazon rainforest (Guyon et al., 2005). During biomass burning, smoke particles are injected directly into the atmosphere and can be lifted hundreds of meters upwards by the heat released from the fire, and can then be

transported rapidly over the whole Amazon region (Reddington et al., 2019). Biomass burning results in a mixture of black carbon, organic materials, soil dust, ash, and other inorganic species (Andreae et al., 1998). Although the exact composition fraction is modulated by factors such as the vegetation type and combustion completion level (Andreae, 2019), generally, OC and BC account for ~50–60% and ~5–10% of the biomass burning aerosols (Reid et al., 2005). With such chemical composition, the hygroscopicity of the smoke particles is generally at the level of 0.1–0.2 (Pöhlker et al., 2018), which corresponds to an activation diameter of ~0.07–0.1 μm at the supersaturation of 0.5% (Su et al., 2010). As the majority of freshly emitted biomass burning aerosols is in the aitken and accumulation mode (Martin et al., 2010), the smoke particles can act as efficient cloud condensation nuclei in the atmosphere. Besides, the smoke particles tend to increase their hygroscopicity during the particle aging process (Reid et al., 2005). One significant characteristic of the biomass burning aerosol emission in the Amazon is its pronounced interannual variation, which is caused by the interannual variation of precipitation amount and the factors related to the deforestation practice such as economic growth and government control policies.

Although SOA is incomparable to biomass burning aerosols in magnitude near the surface, SOA dominates the remarkably high concentration of aerosols in the upper troposphere where the aerosol loading can be as large as that near the surface (Andreae et al., 2018; Schulz et al., 2018). Such high SOA concentration in the Amazon is driven by the large emission of BVOCs from the canopy in this region, which poses an SOA hotspot area in the global SOA distribution (Rasmussen & Khalil, 1988). The most important SOA precursors in the Amazon are isoprene (C_5H_8) and monoterpenes that are mainly constituted by α-pinene and β-pinene. After emission, BVOCs can be oxidized by atmospheric oxidants such as OH, O_3, and NO_3. The oxidation by OH is prominent for the tropical region due to the high concentration of OH (Lelieveld et al., 2008). The oxidized products of BVOCs are gases with a variety of volatility,

and some of them are low volatile so that they condense efficiently onto preexisting aerosols to form SOA. Another mechanism of SOA formation in the atmosphere is through organic nucleation (Kirkby et al., 2016). Some oxidized products of BVOCs possess extremely low volatility and can nucleate into stable clusters and then combine into particles with diameters around 1 nm. Such phenomenon is rarely observed near the surface in the Amazon (Krejci et al., 2005; Rissler et al., 2006). However, recent aircraft observations detected enhanced number concentration in both cloud-active-sized and ultrafine-sized particles in the upper troposphere over the Amazon during the dry season (Andreae et al., 2018). Meanwhile, observations show the indication that the upper tropospheric SOA is related to the oxidation products of BVOCs through new particle production and particle growth (Schulz et al., 2018).

1.3.2 Cloud and precipitation

The meteorology of the Amazon Basin is governed by two distinct seasons: the wet season which lasts from December–June in the next year and the dry season which starts in June and ends in November (Andreae et al., 2015) as a result of seasonal movement of Southern Hemisphere frontal systems (Wang & Fu, 2002). The total precipitation amount is much higher in the former season than during the latter period (Tanaka et al., 2014). However, the individual rainfall events during the dry season have been found with stronger intensity compared with the ones in the wet season, demonstrating as both larger convection inhibition (CIN) and convective available potential energy (CAPE; Andreae et al., 2018; Cifelli et al., 2004), higher frequency of lightning (Williams et al., 2002), and larger local rainfall rates. Satellite observations have observed that the convection characteristics during the wet season are close to those of the tropical oceanic convection (Petersen & Rutledge, 2001) while the convections in the dry season are characterized by continental convection features (Petersen & Rutledge, 2001). Among the weather systems that drive the convection, the troughs in the easterly waves and the squall line systems are important sources for the cloud and precipitation events during

the wet season (Greco et al., 1990), while the dry season is primarily governed by locally generated convection (Zhuang et al., 2017) and only occasionally affected by the propagating mesoscale convective systems (Rickenbach, 2004).

The local convection, as the primary weather system in the Amazon region during the dry season, originates from local land-atmosphere interactions driven by the heating of the ground surface. Therefore, the local convective clouds usually start in the morning and fully develop in the afternoon, usually forming as composites of cloud cells with a radius of 2–3 km. The local convective clouds can be shallow or deep depending on the local thermodynamic and moist conditions. Shallow convection develops within limited vertical altitudes and therefore involves mainly warm cloud processes. Raindrops from shallow clouds grow from cloud droplets by vapor condensation and collision and coalescence of smaller droplets, usually exhibiting as drizzle (Petty, 1999; Schumacher & Houze, 2003; Short & Nakamura, 2000). Initial shallow convections can transform into deep convection as they develop in favorable conditions (Wright et al., 2017; Zhuang et al., 2017). Deep convections in the Amazon region can stretch up to high altitudes and some can even grow up to the height of the tropopause, generating anvil clouds (Zipser & Lutz, 1994). Therefore, deep convective clouds include warm, cold, and mixed-phase cloud processes. The ice-phase precipitating hydrometers like graupel and snow as well as mixed-phase cloud processes are important for the rainfall in deep convections (Benmoshe & Khain, 2014).

The cloud and precipitation in the Amazon region exhibit interannual variability due to the variations of large-scale atmospheric circulation such as the Atlantic SST pattern (Uvo et al., 1998), the ENSO in the equatorial Pacific (Ropelewski & Halpert, 1987), and the position and strength of the ITCZ (Nobre & Shukla, 1996).

1.3.3 Current understanding of aerosol effect on cloud and precipitation in the Amazon

The dry season in the Amazon features the smallest rainfall and the largest amount of aerosols during an annual cycle, which especially necessitates an accurate assessment of the aerosols' impact on cloud and precipitation. Previous studies have accumulated substantial observational and modeling results for the dry season, which are important for our understanding of the responses of cloud and precipitation to aerosols in this region.

As one pathway, the ARI is pronounced in the Amazon during the dry season due to the high aerosol loading. The aerosols there both scatter and absorb solar radiation and the light-absorbing effect is mainly attributable to the black carbon from prevailing biomass burning. The light-absorbing aerosols reduce the radiation reaching the ground while attaining more energy in the atmosphere. Numerical simulations (Feingold et al., 2005; Jiang & Feingold, 2006) show that the decreased incident solar radiation at the ground surface reduces the surface sensible and latent heat, the main energy and moisture source of the locally originated convections, and effectively suppresses the convection. On the other hand, the smoke aerosols warm the surrounding air and alter the atmospheric thermodynamic structure, but the ultimate impact on convection is largely controlled by the vertical location of the smoke aerosols (Feingold et al., 2005). Specifically, smoke aerosols embedded at cloud level act to facilitate the evaporation of cloud and therefore reduce the cloud cover; those close to the ground surface tend to destabilize the planetary boundary layer and enhance convection and cloud cover. A similar large eddy simulation (Johnson et al., 2004) demonstrates that absorbing aerosols located immediately above the PBL can increase cloud cover below due to the strengthened temperature gradient across the capping inversion and the lowered entrainment of dry air into the PBL. Based on these results, the radiative effect of biomass burning aerosols on cloud and precipitation in the Amazon could be an outcome of the suppression by the reduced surface flux exchange and the complicated cloud adjustments induced by

thermodynamic changes. Case studies by regional models show that a vertical difference could happen regarding the cloud response to biomass burning aerosols (Zhang et al., 2008); the rainfall tends to be organized into a fewer but more intense pattern with an overall reduction (Kolusu et al., 2015).

Acting as CCN, biomass burning aerosols can increase the number and decrease the size of cloud droplets in the Amazon, as simulated by cloud-resolving models (Chang et al., 2015; Reutter et al., 2009). The decreased cloud droplet size has also been observed by satellite (Andreae et al., 2004). However, the expected cloud albedo increases due to the more but smaller droplets is negligible in the Amazon, which is believed to be attributable to the already large optical thickness of the clouds in this region (Platnick & Twomey, 1994; Roberts et al., 2003). The modification of cloud microphysics by biomass burning aerosols has a complicated impact on cloud development and precipitation. Cloud-resolving model simulations of a single cumulus cloud suggest that the cloud water content and precipitation efficiency respond nonlinearly to the aerosol concentration (Chang et al., 2015). In other words, at a certain concentration range, the presence of CCN can enhance the cloud water content and precipitation in a cumulus cloud, while at a higher concentration, the addition of extra CCN may suppress the convection and rainfall. Simulations of cloud ensemble suggest that the inhibition of warm rain may lead to the invigoration of convection in the later stage (Khain et al., 2005). Satellite observation in this area found that clouds influenced by smoke plumes need to develop to a higher altitude to form precipitation than those in clean conditions, but the ultimate rainfall rate is greater in polluted clouds (Andreae et al., 2004). Besides the biomass burning aerosols, primary biogenic aerosols, whose size distribution is dominated by the coarse mode, are found to be able to act as giant CCN, being activated at supersaturations as low as 0.1%. This effect can enhance the collision-coalescence process and therefore influence the precipitation efficiency (Yin et al., 2000). However, due to their marginal fraction, the giant

CCN effect of primary biogenic aerosols may not be prominent in the Amazon (Braga et al., 2017). Aerosols can act as ice nuclei, modifying the cold cloud processes and subsequent precipitation. The locally emitted primary biogenic aerosols and long-range transported dust are observed as an important source of ice nuclei in the Amazon (Prenni et al., 2009; Pöschl et al., 2010). However, the aerosol characteristics required for IN and the detailed mechanism for IN activation are still not clear and therefore the IN effect of aerosols is open to further investigation. Besides these, the issue that aerosols are activated at high altitude is worth examining for the cloud system in the Amazon. Previous model simulations in the Amazon presume that aerosols are activated as CCN only at the cloud base. However, the secondary in-cloud activation of CCN above the cloud base, which has been proven efficient in deep convection (Braga et al., 2017; Phillips et al., 2007), would complement the current assessment of aerosol-cloud interaction in the Amazon region.

The joint effects of the aerosol-radiation interactions and aerosol-cloud interactions on clouds and precipitation in the Amazon have been investigated by regional models and in-situ and satellite observations. A satellite observation reported that the cloud response to biomass burning aerosols transits from an enhancement at a low AOD to a reduction with increasing AOD (Koren et al., 2008). Besides, satellite measurements found nonlinear precipitation to biomass burning aerosols (Lin et al., 2006). In-situ observation suggests that precipitation is enhanced by biomass burning aerosols at unstable atmospheric conditions while is suppressed when the atmospheric stratification is stable (Goncalves et al., 2015). Regional simulations show an increasing trend of cloud optical depth (COD) with increasing AOD when AOD is low, and an opposite COD response at higher AOD (Ten Hoeve et al., 2012). A 30-yr regional simulation found a regional overall reduction in cloud cover and precipitation by biomass burning aerosols (Thornhill et al., 2018).

1.4 Research objectives

As described in previous sections, the impact of aerosols on cloud and precipitation in the Amazon during the dry season is an important yet uncertain scientific question. Despite a number of observation and modeling studies that have been made, several issues remain unaddressed. Figure 1.1 illustrates three unaddressed questions regarding the aerosol impacts on cloud and precipitation in the Amazon which will be further investigated in this dissertation. 1) Previous model studies present results either on one aspect of aerosol-radiation interactions and aerosol-cloud interactions or their overall effect, while the studies examining the two pathways separately and jointly, especially in the context of varying emission intensity, are scarce. Meanwhile, observations can provide the overall impact of aerosols on cloud and precipitation, yet without coordinated simulation taking the two pathways (aerosol-radiation interactions and aerosol-cloud interactions) into consideration, it's difficult to interpret the observation results. 2) Aerosol-cloud interactions have been extensively investigated from cloud microphysical scale to macrophysical scale, but studies regarding aerosol-radiation interactions have mostly been conducted at macrophysical scale. Little is known about the cloud microphysic response to the aerosol radiative effect, which hinders the deep understanding of the aerosol-radiation interactions. 3) CCN concentration in the free troposphere over the Amazon has been underestimated by models, affecting the estimatation of the secondary in-cloud activation of CCN and therefore the aerosol-cloud interactions.

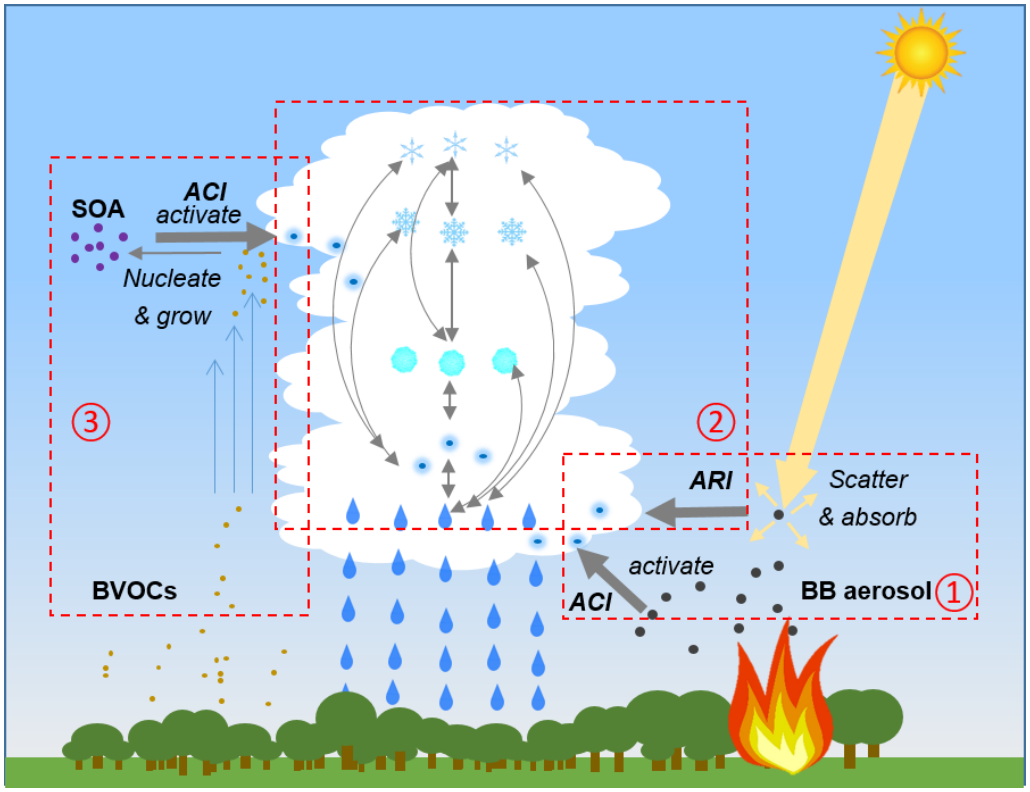

Figure 1.1. Graphical overview of the structure of this dissertation. The grey arrows represent the main processes in the atmosphere relating to the ARI and ACI in the Amazon. The three dashed boxes show questions addressed in this dissertation: ① assessing the ARI and ACI impacts of BB aerosols on the cloud and precipitation formation individually and jointly based on variant emission scenarios, ② revealing the cloud microphysical mechanism behind the rainfall change by the ARI of BB aerosols, and ③ improving the ACI treatment in the model by improving the simulation of SOA-dominated CCN in the upper troposphere, which correspond to the sub-topics in Chapter 2, 3, and 4, respectively.

The main aim of the research presented in this dissertation is to advance the understanding of aerosols' role in the cloud and precipitation formation over the Amazon in the dry season, by comprehensively revealing the two main pathways (aerosol-radiation interactions and aerosol-cloud interactions) and cloud microphysical processes behind them and by improving model representation ability of aerosol processes in high altitudes.

To accomplish this goal, the Weather Research and Forecasting model coupled with chemistry (WRF-Chem), an online coupled meteorology-chemistry model (Grell et al., 2005),

was used to reproduce the cloud and aerosol fields for the Amazon dry season in a coupled way that allows fully interactions among aerosols, radiation, clouds, and precipitation.

The specific scientific goals in this dissertation are:

1) To give a thorough examination on how ARIs and ACIs related with biomass burning aerosols affect the cloud and precipitation formation over the Amazon area individually and jointly, which would be conducted for both the diurnal cycle and the monthly mean state.

2) To quantitatively illustrate the relative significance of the two pathways at reality-based variant biomass burning emission scenarios. In other words, the sensitivity of the two pathways to the changes in aerosol loading would be explored. It has been recognized in single cloud simulations that the aerosol-cloud interactions respond nonlinearly to aerosol concentration (Chang et al., 2015). However, no systematic study has been made regarding the sensitivity of both ACI and ARI to the aerosol loading.

3) To reveal how rain formation-related microphysical processes and subsequent precipitation are altered by biomass burning aerosols when the aerosol-radiation interactions are taken into account on a regional scale.

4) To improve the model performance of CCN simulation in the upper troposphere in the Amazon. This would provide a basis for implementing the parameterization of secondary CCN activation in numerical models and advancing the understanding of aerosol-cloud interaction mechanisms in this region.

The dissertation is organized as follows: Chapter 2 is dedicated to assessing the impact on cloud and precipitation by ARIs and ACIs of biomass burning aerosols in the Amazon dry season as well as examining their relative role with varying emission scenarios. Chapter 3 further probes deeper into the modification of cloud microphysical processes and subsequent precipitation by biomass burning aerosols, with a focus on the ARIs. The process analysis method is utilized to explicitly quantify individual responses of the multiple cloud

microphysical processes. In Chapter 4, an effort of improving the model parameterization of aerosol-cloud interactions is made by improving the CCN simulation at a higher altitude over the Amazon. Newly developed modules of organic nucleation and condensation are integrated into the WRF-Chem model. Chapter 5 summarizes the conclusions reached in this work and discusses future perspectives for the investigations on this scientific topic.

Chapter 2 Relative roles of aerosol-cloud and aerosol-radiation interactions in cloud and precipitation formation

2.1 Introduction

Biomass burning (BB) aerosols were reported to cause a negative direct radiative forcing ranging from several to tens of watts per square meter (W m^{-2}) at the top of the atmosphere (TOA) over the Amazon area (Kolusu et al., 2015; Procopio et al., 2004; Sena et al., 2013; Zhang et al., 2008). However, when it comes to the BB aerosol total radiative forcing which not only includes the aerosol direct radiative effect but also involves the radiative disturbance by aerosol-induced cloud adjustments, it is inconsistent in both sign and magnitude between different modeling estimates (Archer-Nicholls et al., 2016; Kolusu et al., 2015; Ten Hoeve et al., 2012). It indicates that the cloud responses to BB aerosols in different simulations may play a key role in causing the unagreeable BB aerosol radiative forcing estimates among studies, which should be examined deeply.

The inconsistent cloud responses to BB aerosols over the Amazon were reported by both observation and models. Satellite remote sensing measurements showed both suppression and enhancement of cloud fraction with the presence of BB aerosols in the Amazon (Kaufman & Fraser, 1997; Kaufman & Koren, 2006; Koren et al., 2004; Koren et al., 2008). Simulations by both cloud-resolving models and regional atmosphere-aerosol coupled models found enhanced cloud water burdens due to the microphysical effects of BB aerosols (Wu et al., 2011b). Their radiative effect was shown by large-eddy simulation to efficiently diminish liquid cloud amount by evaporating cloud droplets. Precipitation from convective clouds was also reported to be either inhibited or invigorated based on observations from in situ, aircraft, and satellite remote sensing measurements (Andreae et al., 2004; Gonçalves et al., 2015; Lin et al., 2006).

Cloud-resolving modeling provided some clues for the varying cloud and precipitation response estimates by finding nonlinear relationships between aerosol loading and precipitation in the ACIs of BB aerosols (Carslaw et al., 2013; Chang et al., 2015). Indeed, interannual variability is a prominent characteristic of the biomass burning intensity in the Amazon (Bevan et al., 2009; Kaufman & Fraser, 1997; Pöhlker et al., 2019). However, most previous studies assessed the climate response to BB aerosols based on the BB emission scenario of 1 specific year (Archer-Nicholls et al., 2016; Kolusu et al., 2015; Ten Hoeve et al., 2012; Wu et al., 2011b; Zhang et al., 2008; Zhang, Fu, et al., 2009). Given the possible nonlinear relationship between convection and aerosol concentration (Carslaw et al., 2013; Chang et al., 2015), the necessity of a thorough assessment of cloud and precipitation responses to BB aerosols over an extensive range of emissions is underscored.

To investigate the effects of BB aerosols on the Amazon clouds and precipitation quantitatively and mechanistically, WRF-Chem simulations over the Amazon Basin in September 2014 were performed for a 'clean' condition, defined by the absence of influence from biomass burning, and for a set of emission scenarios resembling the realistic interannual emission variability in the dry season. Comparison of the precipitation in central Amazonia in the year 2014 with that averaged over 18 years (1998–2016) indicates that the atmospheric conditions in this region in 2014 are climatically representative (Pöhlker et al., 2016). Therefore, the present study based on September 2014 may serve to represent the typical sensitivity behaviour of the dry season climate to BB aerosol concentration variations. As case study simulations imply that the initial convection response may influence secondary convection (Khain et al., 2005), monthly averaged effects of BB aerosols were assessed here to demonstrate an overall characteristic for the whole month. Individual processes of ARI and ACI were disentangled in our simulations, based on which the relative significance of the two pathways and their sensitivity to emission intensity were quantified.

2.2 Model description, configuration, and numerical experiments.

WRF-Chem is an online coupled meteorology-chemistry model that integrates meteorology and chemistry with aerosol-radiation-cloud feedbacks (Grell et al., 2005). WRF-Chem version 3.9.1 was used in this study to investigate the impact of BB aerosols on the energy budget and hydrological cycle over the Amazon Basin. The Carbon-Bond Mechanism version Z (CBMZ) gas phase chemistry mechanism (Zaveri & Peters, 1999) and the Model for Simulating Aerosol Interactions and Chemistry (MOSAIC) aerosol module (Zaveri et al., 2008) were selected. The aerosol size distribution is described by eight discrete size bins defined by their lower and upper dry particle diameters ranging from 39 nm to 10 μm. Aerosols are assumed internally mixed in each bin to engage in microphysical processes. Other major schemes utilized, e.g., the RRTMG longwave and shortwave radiation scheme (Mlawer et al., 1997; Pincus et al., 2003), the Lin et al. microphysics scheme (Lin et al., 1983), and the Grell-Devenyi cumulus parameterization (Grell & Devenyi, 2002), are described in Table 2.1.

Table 2.1. WRF-Chem configuration.

Atmospheric Process	WRF-Chem Option
Longwave radiation	RRTMG
Shortwave radiation	RRTMG
Surface layer	Monin-Obukhov
Land surface	RUC
Boundary layer	YSU
Microphysics	Lin et al.
Cumulus	Grell-Devenyi ensemble scheme in the 75 km and 15 km simulations; no cumulus scheme in the 3 km simulation
Gas-phase chemistry	CBMZ
Aerosol module	MOSAIC
Aqueous-phase chemistry	Fahey and Pandis
Photolysis	Fast-J
Anthropogenic emissions	EDGAR-HTAPv2
Biogenic emissions	MEGAN
Biomass burning emissions	FINNv1.5

To participate in the radiative processes, each aerosol component in the MOSAIC aerosol module is prescribed with a refractive index based on the values suggested in Barnard (2010). To avoid the overestimation of the particle absorption cross section when using the

internal mixing of BC with other aerosol components (Bond & Bergstrom, 2006), the Maxwell-Garnett mixing rule assuming spheres of BC distributed randomly throughout a mixture of other aerosol components was applied in this study (Bond & Bergstrom, 2006). Note that the process of BC aging (Peng et al., 2016; Wang et al., 2018) has not been implemented in the model. In the future, it would be desirable to implement BC aging (Peng et al., 2016; Wang et al., 2018) in order to more accurately simulate the mixing state of BC-containing aerosols. With the mixed refractive indices, the aerosol extinction efficiency, single-scattering albedo, and asymmetry factor are computed using a Mie algorithm for each size bin and wavelength. The total optical properties are then obtained by integrating over all of the size bins and used as inputs to the RRTMG radiation transfer model for the shortwave (Fast et al., 2006) and longwave spectrum (Zhao et al., 2013). Aerosol-cloud interactions are accounted for in the model through three pathways: activation of aerosol particles to form cloud droplets as well as their resuspension from evaporating cloud droplets, aqueous chemistry, and wet deposition (Chapman et al., 2009). Aerosols are treated as 'interstitial' or 'cloud-borne' according to whether they are activated as CCN, and the calculation of the activation process follows the methodology of Abdul-Razzak (Abdul-Razzak & Ghan, 2002). The two-moment Lin et al. microphysics scheme (Lin et al., 1983; Rutledge & Hobbs, 1984) was employed in this study, where prognostic cloud droplet number is treated based on activated aerosols following Ghan et al. (1997), and the autoconversion of cloud droplets to rain droplets is dependent on droplet number (Liu et al., 2005) so that aerosols are allowed to potentially influence the rain rate and liquid clouds (Chapman et al., 2009; Ghan et al., 1997). The aerosol-aware Lin et al. microphysics scheme has been used previously in investigating aerosol impacts on synoptic cyclones (Ye et al., 2019), regional fog (Lee et al., 2016), and local convection systems (Wu et al., 2011b). In order to validate the response of our model to increasing CCN, monthly mean domain-averaged cloud droplet radii and corresponding cloud-base CCN concentrations were

calculated for simulations with different emission rates, shown in Fig. 2.2. The sensitivity of cloud droplet radius to increasing CCN concentration is pronounced at lower CCN concentrations, while the response tends to saturate at higher CCN concentrations. The saturation of the response of droplet radius to aerosol concentration has also been observed by satellite (Breon et al., 2002). These observations suggested a saturation point at AOD of 0.3, which corresponds to the relatively higher aerosol concentration scenario (EMIS3) in our study. Cloud-borne aerosols and trace gases dissolved in cloud water interact through aqueous chemistry, which may modify aerosol composition and content. The aqueous phase chemistry is based on the Carnegie Mellon University (CMU) bulk aqueous-phase chemical mechanism (Fahey & Pandis, 2001). Wet deposition of aerosols includes in- and below-cloud removal through being collected by rain, graupel, and snow (Chapman et al., 2009) and through being scavenged by precipitation washout (Easter et al., 2004), respectively.

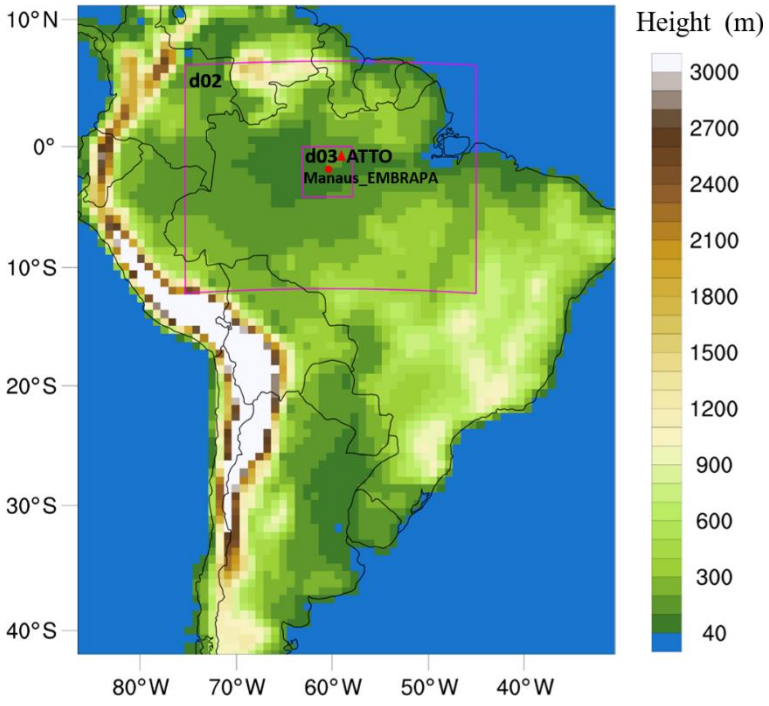

Figure 2.1. Model domain and orography. The outer map represents the parent domain with 75 km horizontal grid spacing, and the embedded squares show the extents of the 15 km (d02) and 3 km (d03) nested domains. The red dot denotes the AERONET monitoring station; the triangle represents the ATTO site.

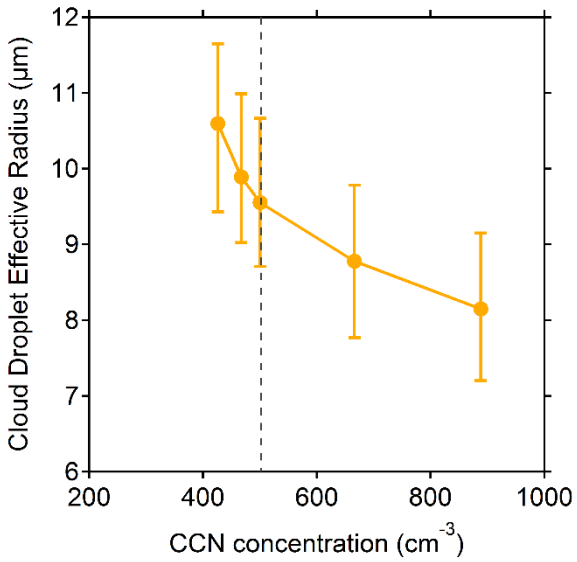

Figure 2.2. Relationship of monthly mean domain-averaged cloud droplet effective radius and cloud-base CCN concentrations for all emission scenarios derived from experiments of CCNR3 and PCNR3_EMISX (Table 2.2). The dashed line indicates the EMIS1 scenario. Error bars represent the 25th and 75th percentiles of all domain-averaged data in each simulation.

In this study, three nested domains with horizontal resolutions of 75, 15, and 3 km were set up over South America (Fig. 2.1). Domain1 covers most of the South American continent, with the biomass burning source region included. Domain3 centers around the Amazon Tall Tower Observatory (ATTO) site to represent the typical climate and environment of the central Amazon Basin (Andreae et al., 2015) and uses cloud-resolving grid spacing with the Grell cumulus parameterization turned off (Table 2.1). Vertical layers of 29 levels extending from ground to 50 hPa were employed for all domains. The outer domains were two-way coupled with initial and boundary meteorological and chemical conditions from the 6 h National Centers for Environmental Prediction (NCEP) Final Analysis (FNL) data and Model for Ozone and Related Chemical Tracers, version 4 (MOZART-4), global chemical transport model output (Emmons et al., 2010), respectively. The Four Dimensional Data Assimilation (FDDA) of temperature, horizontal wind, and moisture was applied for the outer domains to reduce meteorological biases (Otte et al., 2012). The innermost domain was driven one way by initial

and boundary inputs from the outer domain. No nudging was used in the innermost domain. The aerosol-induced perturbations were estimated with the meteorological fields simulated in domain3. Anthropogenic emissions were from the EDGAR-HTAPv2, a global gridded air pollution emission dataset with a resolution of 0.1° × 0.1° (Janssens-Maenhout et al., 2015). The biogenic emissions were generated online by Model of Emissions of Gases and Aerosols from Nature (MEGAN; Guenther et al., 2006). The Fire Inventory from NCAR version 1.5 (FINNv1.5; Wiedinmyer et al., 2011), which provides global estimates of the trace gas and particle emissions from open fires updated daily with 1 km resolution, was used to provide the biomass burning emissions. The primary organic matter (POM) emission rate was converted from OC emission based on an observed ratio of 1.5 between the mass of POM and OC (Reid et al., 2005). The conversion factor 1.5, broadly used in WRF-Chem simulations for biomass burning emission (Archer-Nicholls et al., 2015; Ge et al., 2014), represents the lower end of the range of POM/OC ratios for fresh aerosol emissions from biomass burning (Andreae, 2019). Plume ascent from fire emission sources is calculated by a plume rise parameterization (Freitas et al., 2007; Grell et al., 2011). The simulation spans from 24 August to 30 September 2014, when the Amazon Basin was undergoing its dry season with biomass burning prevalent. The simulation was conducted at 72 hr time slots, with the last 48 hr being used for analysis. In each recycle, the meteorological field was reinitialized, while the chemical field was restarted from the preceding run. The first 6 days of the simulation were used as spinup. Details on model configurations are listed in Table 2.1. In order to quantify the impact of BB aerosols on radiation, cloud, and precipitation, a set of BB aerosol emission scenarios generated by multiplying different aerosol emission factors (X) with the original BB aerosol emission was applied to all domains. As sub-grid convective parameterization can cause uncertainties to the impacts from BB aerosols due to the lack of aerosol-cloud interactions in the sub-grid convective parameterization (Archer-Nicholls et al., 2016), the analysis of BB aerosol effects

in the following section is based on the domain3 simulation where convections are explicitly resolved at 3 km resolution. Simulations of domain3, namely PC3_EMISX, were conducted using the BB aerosol emission scenario (EMISX) and chemical boundary conditions from the outer-domain simulation with the corresponding emission scenario (Table 2.2). A control simulation CC3 was conducted without influence of biomass burning emissions. Then the total effects of BB aerosols can be evaluated from the difference between the PC3_EMISX and CC3 simulations.

Table 2.2. Description of numerical experiment design.

Experiment identification	Experiment description
CC3	Clean case at 3 km resolution without BB emission.
CCNR3	Clean case at 3 km resolution without BB emission. The aerosol radiation feedback is turned off.
PC3_EMISX	Polluted case at 3 km resolution with BB emission scenario EMISX. EMISX represents scenario with BB aerosol emission rate scaled by a factor of X based on original BB emission.
PCNR3_EMISX	Polluted case at 3 km resolution with BB emission scenario EMISX. The aerosol radiation feedback is turned off.

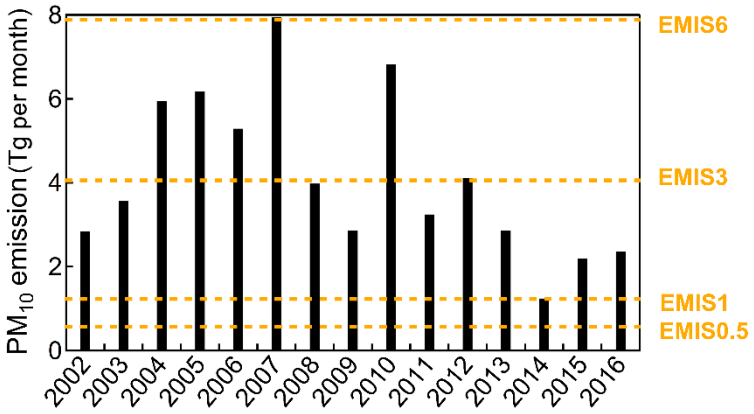

Figure 2.3. Annual variation in PM_{10} emission during September over domain1 based on FINNv1.5.

As shown in Fig. 2.3, the biomass burning emissions during September undergo large annual variations, e.g., the emission in 2007 is 6 times as much as that in 2014. The variation pattern of PM_{10} emitted from BB in September is consistent with an interannual variation in

MODIS-retrieved AOD over the Amazon (Sena et al., 2013). Based on the range of emission intensities from 2002 to 2016, three emission scenarios representing different emission strength were chosen: EMIS1 for emission in 2014; EMIS3 for an average intensity over all the years; and EMIS6 for the emission intensity in 2007, which corresponds to the maximum emission intensity from 2002 to 2016. In addition, emission scenario EMIS0.5 was added to mimic the reduced BB emissions projected assuming the influence of enhanced government regulation policy (Streets, 2007). The domain3-averaged AOD in the simulations for the EMIS0.5, EMIS1, EMIS3, and EMIS6 emission scenarios is used to represent the aerosol concentration under the corresponding emission scenarios in the analysis in next section.

To assess the ACI and the ARI effect of BB aerosols separately and jointly, the ACI and ARI effects were calculated following the method used in Archer-Nicholls et al. (2016). Parallel simulations with PC3_EMISX and CC3 were performed in the absence of aerosol radiative feedbacks, namely PCNR3_EMISX and CCNR3, respectively (Table 2.2). The ACI effect of BB aerosols in each emission scenario can be assessed from the difference between PCNR3_EMISX and CCNR3, where aerosols were radiatively inactive and only the aerosol effect on cloud microphysics was included. Then the ARI effect of BB aerosols was obtained by deducting the ACI effect from the aerosol total effect (Archer-Nicholls et al., 2016). This way of calculating the ARI of BB aerosols enables assessments of the ARI solely from BB aerosols without the influence of aerosols from other origins (Ghan et al., 2012).

2.3 Results

2.3.1 Model evaluation

The WRF-Chem simulation with the EMIS1 scenario was evaluated for the meteorological conditions and the aerosol field using satellite and ground-based measurements which are listed in Table 2.3.

Table 2.3. Observation datasets.

Variable	Dataset	Description	reference
Precipitation	TRMM	Satellite observations of tropical and subtropical (50 °S–50 °N) precipitation. The 3B42 rainfall dataset produces 3-hr averaged high-quality infrared and microwave precipitation estimates at a resolution of 0.25°×0.25°	(Huffman et al., 2007)
Liquid water path Ice water path Cloud cover	The Moderate Resolution Imaging Spectroradiometer (MODIS) Level 3	Satellite-derived daily estimates of cloud properties at a resolution of 1°×1°. The measurements time of Aqua is approximately at 13:30 local time. Model outputs at the satellite detection time were used when comparing against MODIS data.	(Platnick, S., et al., 2015)
AOD	The Aerosol Robotic Network (AERONET) Level 2.0	TheAOD at 550 nm was interpolated using corresponding measurements at 675 nm and 440 nm for the site Manaus_EMBRAPA (2.89 °S, 59.97 °W) over September 2014.	(Holben et al., 2001)
Extinction coefficient profile	The Cloud-Aerosol Lidar and Infrared Pathfinder Satellite Observations (CALIPSO) Level 3	Global gridded dataset with a horizontal resolution of 2°×5°. The clear-sky aerosol extinction at 532 nm of both daytime and nighttime measurements over the studied region was used.	(Tackett et al., 2018)
CCN number concentration	Amazon Tall Tower Observatory (ATTO)	The CCN number concentration measurements at 60 m height by a CCN counter with supersaturation cycling through a set of levels ranging from 0.11% to 1.1% were used.	(Andreae et al., 2015; Pöhlker et al., 2016; Pöhlker et al., 2018).

The daily retrievals of cloud fraction, total cloud water path (LWP), and total ice water path (IWP) from the MODIS Aqua measurements are used to evaluate the simulation performance for cloud properties by WRF-Chem. The domain3 simulation results are averaged over the domain area to compare with the corresponding variables from the satellite measurements, as shown in Fig. 2.4. The simulated total LWP, calculated as the sum of liquid cloud and rainwater, correlates well with observations with a moderate underestimation. The total IWP from the model, as the sum of cloud ice, snow, and graupel, basically shows a positive correlation with the observations. However, a large underestimation of the total IWP from the model exists compared to the remote-sensed data. The model performs relatively well for the extreme low and high IWP regimes, with values being approximately 25% of the observations. The simulation of the total IWP by the WRF model has been found to produce a seasonally averaged underestimation by up to 80% compared with satellite measurements (Baro et al., 2018). The uncertainties inherent in the satellite dataset, e.g., eliminating data points with unrecognized cloud ice, would bias the observation results towards higher values and thus to some extent account for the discrepancy between model and observation. Besides, uncertainties associated with the ice-phase microphysical processes, e.g., the lack of IN parameterization, may also be a potential reason for this discrepancy (Su & Fung, 2018). Generally, the total cloud fraction from the model shows a linear correlation with the observations, falling between 25%–75% of the observed values. Figure 2.5 shows the time series of domain-averaged 3-hr accumulated precipitation from the domain3 simulation and corresponding TRMM measurements during September 2014. Despite some underestimation of the rainfall, e.g., on 8 Sep and 17 Sep, the overall precipitation simulated by WRF-Chem is comparable with TRMM observations in terms of time variation and intensity, which illustrates the model's ability to represent the convective activity during the study period.

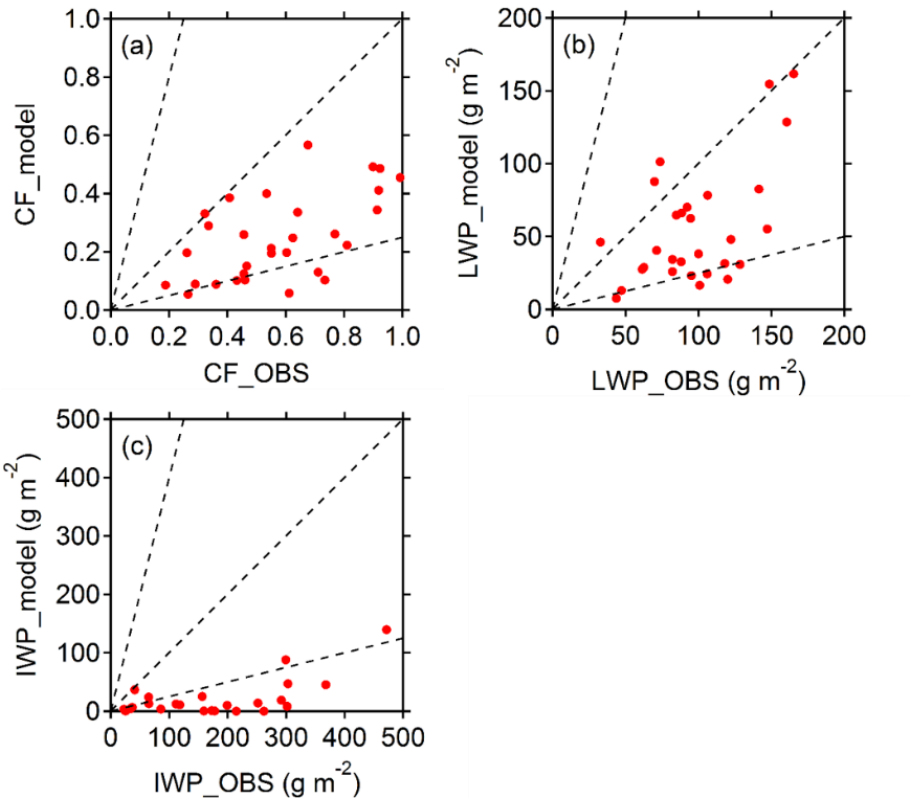

Figure 2.4. Scatter plots of (a) cloud fraction, (b) total liquid water path, and (c) total ice water path from WRF-Chem domain3 simulations and MODIS satellite measurements. The dashed lines are 1:4, 1:1, 4:1 from top to bottom, respectively.

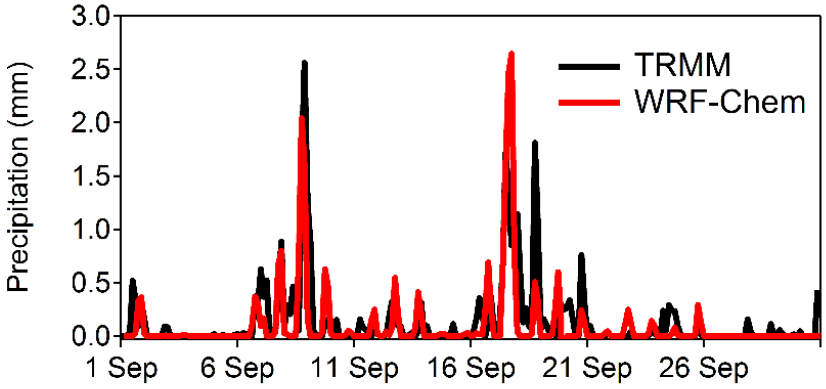

Figure 2.5. Time series of region averaged 3-hr accumulated precipitation (mm) over domain3 from TRMM satellite observations and WRF-Chem simulations during September 2014.

Table 2.4. Comparison of AOD and SSA at 550 nm obtained from model simulation in domain3 and observation.

	Observation	Model[a]
	AOD	
Manaus_EMBRAPA (AERONET)	0.24±0.10 (average of Sep 2014)	0.21±0.05 (R^b=0.54)
	SSA	
TT34[c] (Rizzo et al., 2013)	0.87±0.06 (average of Jul–Dec 2008–2010)	0.89±0.01
ATTO[d] (Saturno et al., 2018)	0.88 (average of Aug–Nov 2012–2017)	0.90±0.01

a) Model results with EMIS1, averaged for September 2014.
b) R represents the correlation coefficient between the observation and model simulation.
c) The SSA values at this site are for 637 nm. Calculation of SSA at 550 nm is not conducted due to incomplete information on Angstrom exponent in Rizzo et al. (2013).
d) The SSA observation for the ATTO site is obtained from Saturno et al. (2018) by extrapolating the original value at 637 nm to that at 550 nm using the Angstrom exponents in Saturno et al. (2018).

Table 2.4 shows the comparison of the modeled AOD against the AERONET observation at Manaus_EMBRAPA, a forest reservation site representative of the central Amazon environment (Artaxo et al., 2013). The model simulation generally captures the absolute value and the temporal variation of the observed AOD, with the mean bias and correlation coefficient being –0.03 and 0.54, respectively (Table 2.4). This is basically consistent with the AOD prediction accuracy in the Amazon by global models using the same fire emission inventory (Pan et al., 2020; Reddington et al., 2019). The slightly low bias in the AOD value could be related to an underestimated BB emission intensity due to errors in the detection of fires by satellite (Rosario et al., 2013) and/or an underestimation of the transatlantic transport from Africa (Holanda et al., 2020). Besides, the lack of SOA production in the model may also account for the bias in the AOD simulation (Bond & Bergstrom, 2006). The simulated SSA is compared with observations from previous studies, as shown in Table 2.4. Compared with the in-situ measured SSA of 0.87±0.06 at 637 nm at the TT34 tower (Rizzo et al., 2013) in the central Amazon, a slightly higher value of 0.89±0.01 is obtained by the model simulation. Similarly, the modeled monthly mean SSA of 0.90 for the location of the

ATTO site is relatively higher than an extrapolated value of 0.88 at 550 nm from multi-year observations for the dry season at the ATTO site (Saturno et al., 2018). Given the substantial influence of BB particles on the aerosol SSA (Saturno et al., 2018), the difference between model results and observation may be associated with the mismatched average time periods for the comparison. Generally, the simulated SSA does not deviate greatly from the observed value, which reflects a reasonable representation of the aerosol optical characteristics in the model.

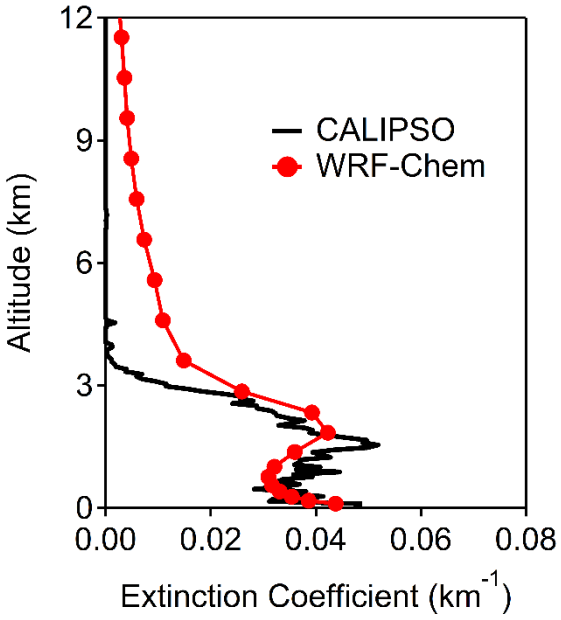

Figure 2.6. Monthly mean clear-sky aerosol extinction coefficient at 532 nm averaged over domain3.

The aerosol vertical distribution is evaluated using the CALIPSO-measured monthly mean clear-sky aerosol extinction profile averaged over the domain3 (Fig. 2.6). The simulation data was processed to align with the observation by using outputs corresponding to the passing time of the satellite, excluding cloudy grids with a cloud criterion of 1 g kg^{-1} and interpolating the extinction coefficient at 550 nm to 532 nm. The model reproduced the observed high aerosol extinction coefficient below 3 km and accurately captured the location of the two peaks at the surface and near 2 km respectively. Compared with the observation, the model

overestimates the aerosol extinction above 3 km, which was also found in Wu et al. (2011a). This discrepancy may be associated with an overestimated exchange between PBL and the free atmosphere by turbulent mixing and convective transport, an underestimation of precipitation scavenging, and/or an overestimated plume rise at some fire spots. Generally, the model reasonably simulated the aerosol vertical distribution, illustrating an acceptable performance of the plume rise parameterization. The ability of the model to reproduce the aerosol vertical pattern provides reliable aerosol input for investigating the aerosol-radiation-cloud interaction, given the important role of the vertical distribution of light-absorbing aerosols in affecting the aerosol radiative effect (Johnson et al., 2004).

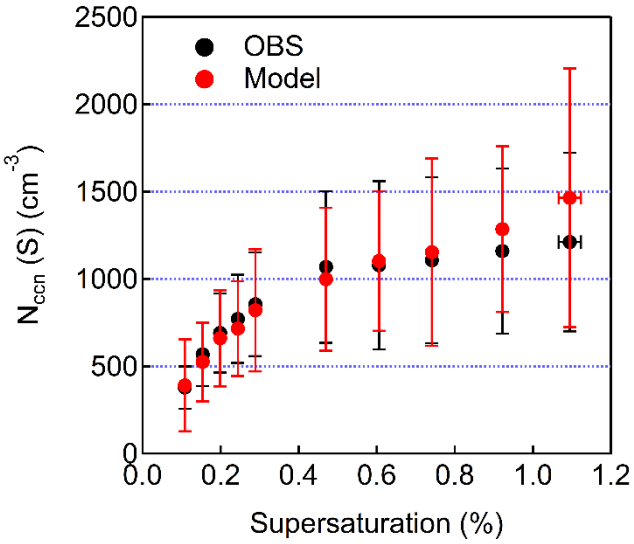

Figure 2.7. Monthly averaged CCN number concentrations at different supersaturations from ATTO observations and WRF-Chem simulations. Error bars represent the standard deviation.

A comparison of CCN concentrations at different supersaturations between in-situ observation and the WRF-Chem simulation for the ATTO site is presented in Fig. 2.7. The calculation of CCN number concentration at observed supersaturation level from model outputs followed the method in Su et al. (2010). The model results show an overall agreement in

magnitude with observations for the supersaturation range of 0.2–0.5%, which represents the typical atmospheric conditions during the dry season in the Amazon (Archer-Nicholls et al., 2016). The variation of CCN number with supersaturation level matches the pattern obtained by observation (Pöhlker et al., 2018), indicating a reasonable sensitivity of aerosol activation ability to varying supersaturation situations.

2.3.2 Response of cloud

Figure 2.8 shows the diurnal and vertical distribution of domain-averaged changes in cloud water and cloud ice concentration caused by BB aerosols. By serving as CCN, BB aerosols create more cloud droplets and cause a reduction in the cloud droplet size (Table 2.5) due to competition for water vapor, which slows down the transfer rate from cloud to rain (Braga et al., 2017; Chang et al., 2015; Rosenfeld et al., 2008). Consequently, cloud water in the free troposphere is increased by the ACI effect throughout the day (Fig. 2.8) at the expense of rainwater concentration, while the diminished cloud water within the PBL corresponds to the warmer air temperature (Fig. 2.9a) and suppressed moisture flux from the ground surface (Table 2.5). The response of cloud water to ARI also varies with altitude. The increased RH within the PBL by the aerosol radiative effect (Fig. 2.9b) lowers the cloud base height (Table 2.5) and favors cloud persistence, resulting in higher cloud water content (Johnson et al., 2004). In contrast, the aerosol radiative heating near the top of the PBL (Fig. 2.9b) decreases the RH and therefore ‘burns off’ the liquid clouds (Feingold et al., 2005; Huang et al., 2016). Such contrasting cloud water responses to the BB aerosol radiative effect between different layers were also found by a large-scale RegCM3 simulation covering South America (Zhang et al., 2008). The increased cloud water in the lower troposphere (0–2 km) was attributed to large-scale moisture convergence. Here, the simulation over a smaller region located in the central Amazon Basin shows that the local modification of the thermodynamic structure by BB aerosols is able to contribute to the effect as well.

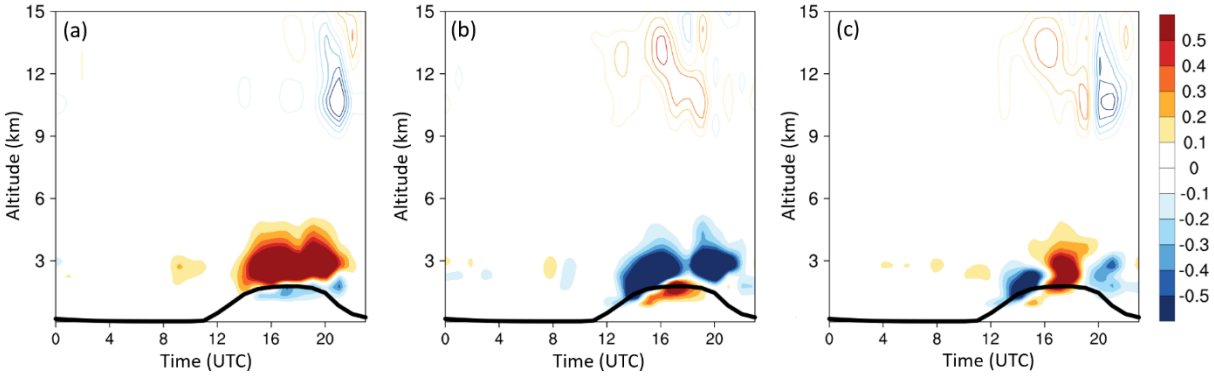

Figure 2.8. Diurnal variation in the vertical distribution of the domain-averaged difference in cloud water (shaded; in mg kg^{-1}) and cloud ice (contour lines; in 0.1 mg kg^{-1}) caused by BB aerosols' (a) ACI, (b) ARI, and (c) total effect in the EMIS1 emission scenario. The thick black line represents the PBL height.

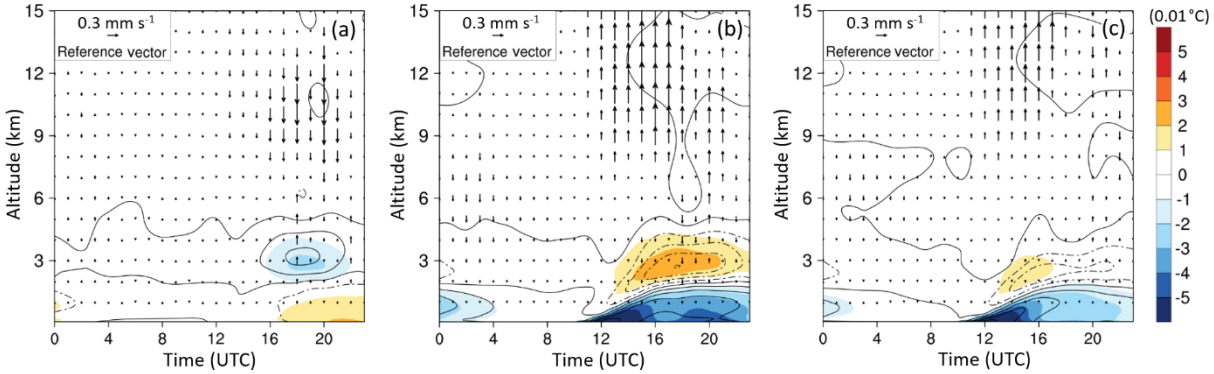

Figure 2.9. Domain-averaged difference in air temperature (shaded, in intervals of 0.01 ºC), relative humidity (contour lines, in intervals of 0.1 %), and updraft velocity (arrows) caused by BB aerosols' (a) ACI, (b) ARI, and (c) total effect in the EMIS1 emission scenario.

Integrated over the atmosphere, the cloud LWP is enhanced by the ACI but reduced by the ARI effect (Ackerman et al., 2000; Feingold et al., 2005; Johnson et al., 2004). Therefore, the overall change in cloud water amount by BB aerosols results from the competition between the ACI and ARI effects. Figure 2.10a displays the dependence of the overall response of cloud water on the emission intensity (represented as AOD). Weaker emission scenarios yield higher

cloud water, driven by the ACI effect, while stronger emissions lead to an opposite response of cloud water, dominated by the ARI effect. The simulated dependence of cloud water change on aerosol amount agrees with satellite measurements of the total cloud fraction over the Amazon region (Koren et al., 2004).

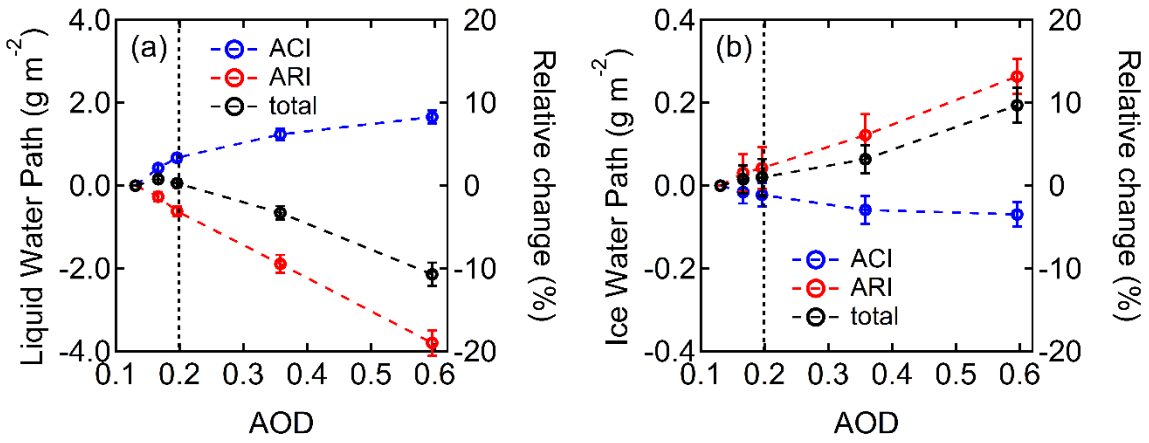

Figure 2.10. Changes in (a) cloud LWP and (b) cloud IWP with increasing BB emission intensity (indicated by domain-averaged AOD in each emission scenario). The vertical dotted line in each plot indicates the EMIS1 scenario. Error bars denote the standard error.

The cloud ice content is invigorated by BB aerosols, driven by the ARI effect (Fig. 2.10b). Through radiation absorption, BB aerosols heat the air, evaporate liquid cloud, and promote upward flux of vapor and moisture to higher altitudes (Fig. 2.9b), facilitating cloud ice formation there. Similar ice enhancement due to aerosol radiative heating was also seen in simulations of dust-radiation interaction (Dipu et al., 2013). This positive response of cloud ice and updraft velocity to ARI corresponds to the thermodynamic invigoration mechanism proposed in Wang et al. (2013), which suggested larger CAPE above PBL could be induced by the absorbing aerosols in the lower troposphere. In contrast, the ACI tends to act in opposition to the ARI effect but in a minor magnitude, showing a moderate negative response (Fig. 2.8a).

The ACI effect has been reported to invigorate deep convection when more abundant, smaller cloud drops are uplifted to boost the cloud microphysical processes at higher altitudes (Rosenfeld et al., 2008), which, however, is sensitive to the background environment (Fan et al., 2009; Khain et al., 2005). Hints of this effect are only seen during a narrow time span around 18:00 and 22:00 UTC, as indicated by increased cloud ice (Fig. 2.8a) and precipitating hydrometeors (Fig. 2.12a). However, the enhancement is insignificant in magnitude and overwhelmed by the negative responses that persist during the rest of the diurnal cycle, which may result from different cloud types and environmental conditions from those in Rosenfeld et al. (2008). Generally, the monthly mean domain-averaged results show a negative effect of the ACI on cloud ice water path (Fig. 10b).

Such nonlinear patterns of cloud LWP and IWP responses to BB aerosols are consistent with those of the BB aerosol shortwave and longwave radiative forcing (RF) at TOA (Fig. 2.11a), respectively, implying the importance of cloud adjustments for affecting BB aerosol RF. Unlike the negative shortwave RF at TOA in clear-sky (Table 2.5), the all-sky shortwave RF at TOA by the ARI, which not only involves the aerosol direct radiative forcing but also contributed by the radiative forcing of ARI-induced cloud adjustments, show positive value and increase in magnitude with increasing BB aerosol concentration. The reason for it is that the cloud LWP reduction by the ARI of BB aerosols cause more solar radiation to reach the surface and less to be reflected, which even overruns the BB aerosol direct RF at TOA in magnitude and strengthens with the increase of BB aerosol loading (Fig. 2.10a). The shortwave RF at TOA by the ACI of BB aerosols also follows the corresponding ACI-induced cloud LWP change, being negative at the presence of more liquid cloud amount (Fig. 2.10a). The total shortwave RF (ARI+ACI) at TOA is −0.3 and 0.6 W m^{-2} for the EMIS1 and EMIS6 scenarios, respectively (Table 2.5), corresponding to the sign variation of the cloud LWP responses (Table 2.5). Similar in magnitude, a modeling study in the Amazon dry season using the HadGEM3-

GA3 model showed a monthly mean shortwave RF of 1.35 W m^{-2} with AOD increasing from 0.19 to 0.67 (Thornhill et al., 2018). The longwave RF by BB aerosols is of comparable magnitude to the shortwave radiative forcing (Table 2.5). The ARI effect is the driving force for the positive longwave RF, as the outgoing infrared radiation can be directly trapped by black carbon contained within the BB particles (Ramachandran & Kedia, 2010). In addition, high clouds mainly comprised of ice are also efficient at blocking outgoing longwave radiation (Hartmann et al., 1992), yielding a positive longwave RF at TOA. Therefore, the ARI-induced larger amount of cloud ice content (Fig. 2.10b) can result in positive longwave RF as well. The positive longwave RF resulting from increased ice cloud is in agreement with the satellite observations of tropical deep convection, where a strong warming was caused by increased convective cloud anvils impacted by aerosols (Koren et al., 2010). The all-band RF (shortwave plus longwave) of BB aerosols changes sign with increasing emission intensity of BB aerosols, with values of −0.2 and 1.5 W m^{-2} for the EMIS1 and EMIS6 scenarios, respectively.

It should be noted that uncertainties associated with BB aerosol effects on cloud ice exist, because of the lack of IN parameterization (Fan et al., 2018). Field observations suggested that the BC in the BB aerosols could contribute substantially to ice nucleation (McCluskey et al., 2014), which may influence the estimate of the response of cloud ice to BB aerosols as well as the associated longwave RF of BB aerosols.

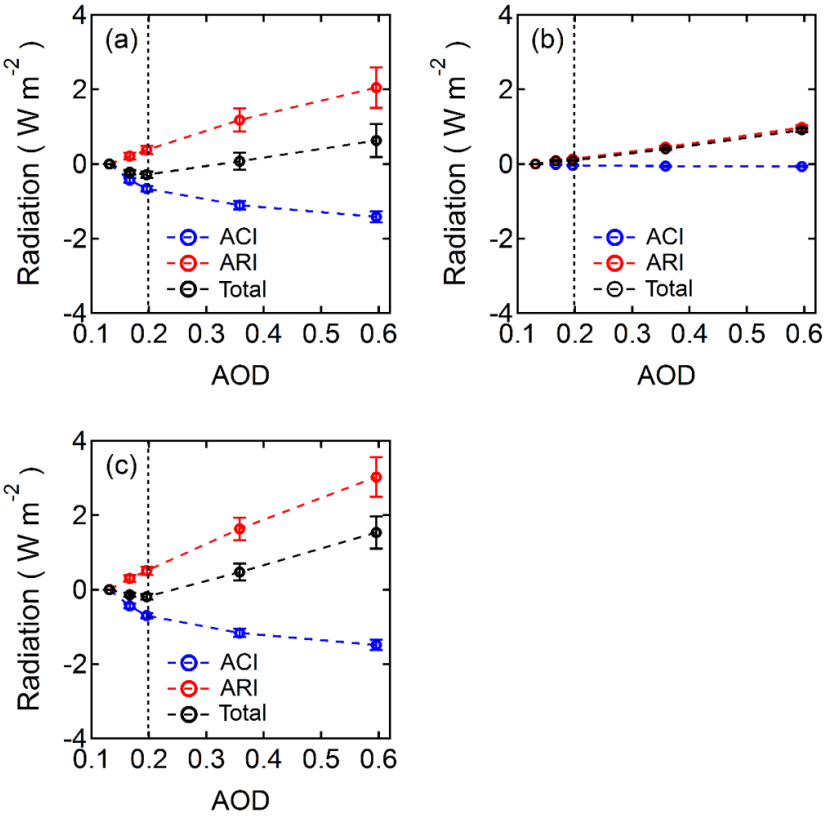

Figure 2.11. Changes in (a) shortwave, (b) longwave, and (c) total radiation budgets at TOA with increasing BB emission intensity (indicated by domain-averaged AOD in each emission scenario). The vertical dotted line in each plot indicates the EMIS1 scenario.

Table 2.5. Summary of monthly mean perturbations caused by the ARI and ACI of BB aerosols in the EMIS1 and EMIS6 emission scenarios.

Variable	ARI		ACI	
	EMIS1	EMIS6	EMIS1	EMIS6
Clear-sky TOA solar radiation (W m^{-2})	–0.7	–3.7		
TOA solar radiation (W m^{-2})	0.4	2.0	–0.7	–1.4
TOA solar + IR radiation (W m^{-2})	0.5	3.0	–0.7	–1.5
Surface solar radiation (W m^{-2})	–5.7	–30.5	–0.6	–1.3
Sensible heat flux (W m^{-2})	–2.3	–14.4	–0.1	–0.2
Latent heat flux (W m^{-2})	–2.0	–11.8	–0.5	–1.1
Surface temperature (°C)	–0.03	–0.20	+0.00	+0.01
PBL height (m)	–8	–58	+0	2
Cloud droplets number (cm^{-2})	-0.7×10^5	-6.0×10^5	4.0×10^5	14.5×10^5
Cloud droplets radius (μm)	–0.7	–0.5	–1.0	–2.6
Cloud base height (m)	–6	–40	1	5
LWP (g m^{-2})	–0.6	–3.8	0.7	1.7
LWP in PBL (g m^{-2})	0.03	0.14	–0.01	–0.04
LWP in FT (g m^{-2})	–0.6	–3.9	0.7	1.7
IWP (g m^{-2})	0.04	0.26	–0.02	–0.07
Precipitation (mm day^{-1})	0.01	–0.11	–0.06	–0.10

2.3.3 Response of precipitation

To show the response of precipitation, the diurnal and vertical distribution of domain-averaged changes in precipitating hydrometeors (sum of rain, snow, and graupel) based on the EMIS1 scenario is presented in Fig. 2.12. The domain-averaged rainwater below the freezing level height of about 5 km shows a prominent negative response to ACI during most of the daytime (Fig. 2.12a). As discussed before, by acting as CCN, the BB aerosols reduce cloud droplet radius, slow down the conversion rate from cloud to rain, and therefore inhibit warm rain formation. On the other hand, consistent with the responses of cloud ice, precipitating hydrometeors are enhanced by the ACI effect in the local afternoon and early night due to the invigorated convection. Generally, an overall reduction in precipitation is induced by the ACI, similar to previous WRF-Chem simulations of BB aerosol microphysical effects in the Amazon (Wu et al., 2011b). The results of the ARI effect show an overall positive impact on precipitating hydrometeor concentrations (Fig. 2.12b) and consequent surface precipitation (Fig. 2.13a) in the EMIS1 scenario. With the influence of the ARI effect, significant enhancement appears in the precipitating hydrometeors above the freezing level beginning in the early morning, indicating cold rain processes. Specifically, the graupel concentration, which is mainly responsible for the cold rain response (Chang et al., 2015), is promoted as more supercooled cloud droplets efficiently feed the growth of graupel. The increased supercooled cloud water concentration could be a result of the enhanced updraft promoted by the ARI (Fig. 2.9b). By 17:00–18:00 UTC, the precipitation reaching the surface is increased correspondingly. The increase in precipitation by the local ARI effect was also found in previous simulations of light-absorbing aerosols, including black carbon (Lin et al., 2016) and mineral dust (Dipu et al., 2013; Huang et al., 2019; Shi et al., 2014). Influenced by the overall effect of both the ACI and ARI mechanisms, a reduction of precipitating hydrometeors is prominent in the morning and afternoon, while enhanced precipitating hydrometeor abundance

occurs in a narrow time span from local noon to early afternoon. The variation in convection response throughout the convective evolution cycle implies a possible dependence of aerosol-radiation-cloud interactions on environmental stabilization, which is also shown by the observation that BB aerosols tend to increase precipitation under unstable conditions (Gonçalves et al., 2015).

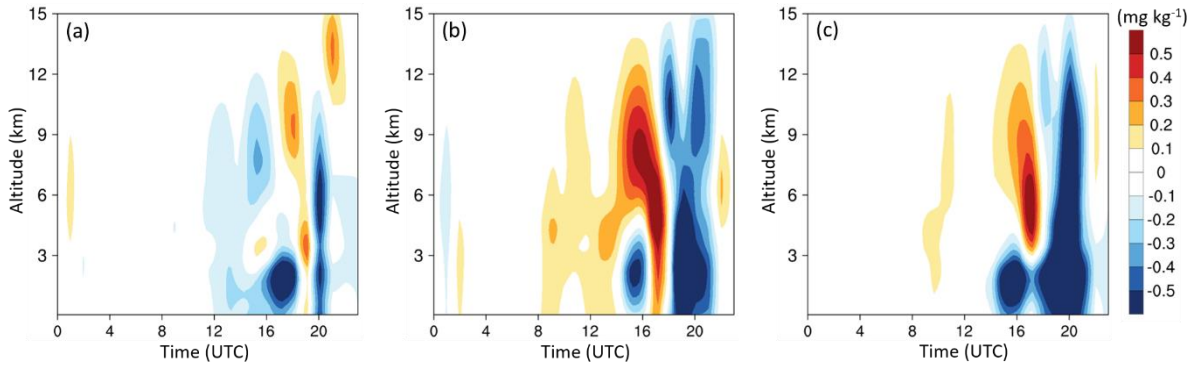

Figure 2.12. Diurnal variation in the vertical distribution of the domain-averaged difference in precipitating hydrometeor (QRAIN+QSNOW+QGRAUP) concentrations caused by BB aerosols' (a) ACI, (b) ARI, and (c) total effect in the EMIS1 emission scenario.

The response of the precipitation rate to different emission intensities of BB aerosols (represented as AOD) is shown in Fig. 2.13a. The precipitation reduction by ACI is climatically significant in all emission scenarios, with a monthly mean change of −7% and −11% at EMIS1 and EMIS6, respectively. The precipitation rate is slightly increased by the ARI at low aerosol loading due to invigorated daytime precipitation as discussed above. However, at high emission intensity, the strong radiative dimming effect of BB aerosols dramatically reduces surface heating (Table 2.5), which damps the ARI-induced convection invigoration and leads to an overall suppression of convection and a significant reduction of precipitation (Rosenfeld et al., 2008). This dimming effect is even more pronounced than the ACI effect in reducing precipitation for the EMIS6 scenario (Fig. 2.13). Taking the ACI and ARI effects together, the monthly mean precipitation rate is decreased by BB aerosols at all emission scenarios used in

this study. A reduction of −5% and −23% is calculated for the EMIS1 and EMIS6 emission scenarios, respectively, aligning in magnitude with a precipitation change by −14.5% for the switch of aerosol loading from the low-emission to the high-emission scenario in the Amazon found by Thornhill et al. (2018).

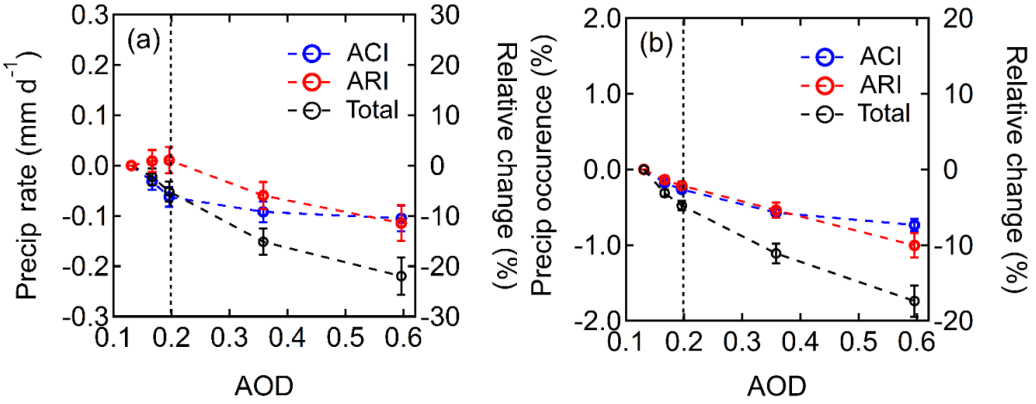

Figure 2.13. Changes in domain-averaged (a) precipitation rate and (b) precipitation occurrence with increasing BB emission intensity (indicated by domain-averaged AOD in each emission scenario). The vertical dotted line in each plot indicates the EMIS1 scenario.

To examine the precipitation responses at different precipitation intensities (Fig. 2.14), a threshold of daily maximum 3-hr accumulated precipitation exceeding 3 mm, the upper boundary of the domain-averaged amount (Fig. 2.5), is used to distinguish the intensive precipitation grids from the light precipitation ones. High convective strength indicated by larger CAPE (Fig. 2.14) corresponds to intensive precipitation, whereas relatively weaker convection is associated with the light precipitation regime. Intensive precipitation shows a significant nonlinear ARI response, whereas light precipitation tends to be reduced monotonically by the ARI. The precipitation reduction by ACI at low aerosol concentration is less prominent in heavy than in light rainfall, due possibly to the dynamic feedbacks in deep convection (Rosenfeld et al., 2008). By contrast, a stronger ACI effect at larger aerosol amounts is shown in heavy precipitation as a result of the larger potential for CCN activation in strong

convection (Reutter et al., 2009). The dependence of precipitation change on aerosol concentration is greater for the intensive precipitation than the light precipitation regime, given that the precipitation responses in the EMIS1 and EMIS6 scenarios are −3% and −27%, respectively, for the intensive regime and −8% and −17%, respectively, for the light precipitation. This is consistent with the rainfall sensitivity to increasing aerosol concentration for strong and weak convection in Chang et al. (2015). The dominance role of ARI over ACI at high aerosol loadings is found at both regimes. The precipitation occurrence (calculated as the ratio of precipitating grid cells to the total domain grid cells over the simulation period), which is approximately 11% in the clean case, is reduced noticeably by both the ACI and ARI effects (Fig. 2.13). The more extensive dry area coverage due to the presence of BB aerosols may act to aggravate the precipitation shortage for the Amazon forest in the dry season (Cox et al., 2008).

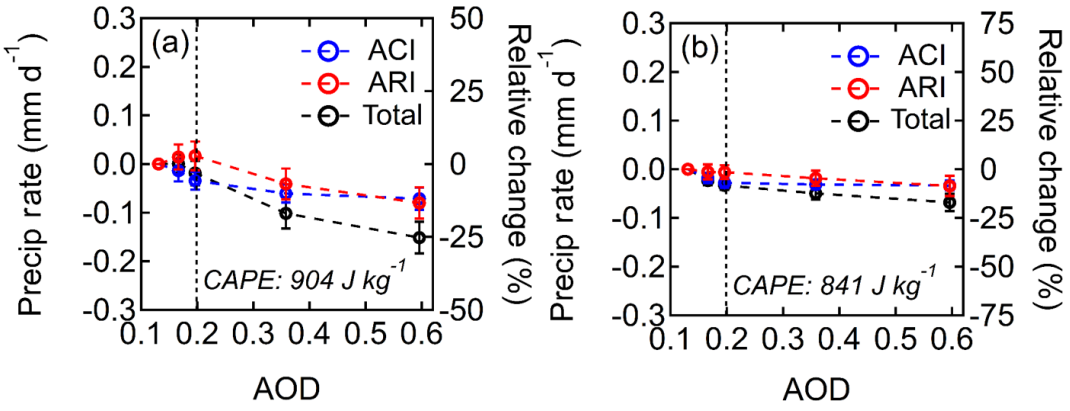

Figure 2.14. Changes in domain-averaged precipitation rate with increasing BB emission intensity (indicated by domain-averaged AOD in each emission scenario) in (a) the intensive precipitation regime and (b) light precipitation regime.

2.4 Conclusions

In this chapter, a comprehensive assessment of the impacts of BB aerosols on the regional cloud and precipitation and their sensitivity to interannual variations in BB aerosol

emissions was made. The effects of ARI and ACI were quantified individually and jointly; their relative significance with varying aerosol concentration was compared.

The shortwave RF of BB aerosols is the outcome of a competition between positive RF by the ARI effect and negative RF by the ACI effect, which is driven largely by the cloud response. The positive shortwave RF associated with cloud reduction due to the ARI effect of the BB aerosols counteracts the negative direct shortwave RF and constitutes the dominant component of ARI-induced effective shortwave RF. Contrarily, the ACI-induced more numerous but smaller cloud droplets increase cloud albedo and thereby exert a negative indirect shortwave RF. The relative significance of the ACI and ARI effects varies with aerosol loading, with a dominant role of the former at low aerosol emission rate, while the latter dominates at high emission intensity. The positive longwave RF by BB aerosols is driven by the ARI effect, through both aerosol direct radiative forcing and subsequent adjustment of enhanced ice cloud. The all-band aerosol RF is −0.2 and 1.5 W m^{-2} for BB aerosols in the EMIS1 and EMIS6 scenarios, respectively. The response of cloud LWP to BB aerosols is driven in opposite directions by the ARI and ACI effects. The surface cooling generated by radiation extinction together with the atmospheric heating from absorption of solar radiation stabilizes the atmosphere, inhibits convection development, and thereby decreases the cloud LWP. In contrast, higher cloud LWP is produced by the ACI effect through inhibited warm rain formation. The relative significance of the competing effects depends on the aerosol amount, consistent with the aerosol shortwave radiative forcing response, implying a crucial role of cloud adjustments in determining aerosol radiative forcing on the Earth-Atmosphere system. Lower precipitation occurrence is induced by both the ARI and ACI effects, which implies a larger fraction of dry areas in the Amazon Basin when affected by BB aerosols and threatens to exacerbate the droughts during the dry season. The domain-averaged precipitation rate is diminished substantially by ACI consistently over all the emission scenarios used in this study.

Strong suppression of warm rain formation is responsible for the overall precipitation reduction caused by the ACI, but in the lower-emission scenarios, an ACI-induced invigoration of deep convection occurs during a narrow period, due to latent heat release from more abundant smaller droplets aloft (Rosenfeld et al., 2008). The precipitation response to the ARI effect is nonlinear possibly associated with the participation of mixed-phase precipitation. At low BB aerosol emission rates, enhanced precipitation is found, but the enhancement disappears in the high-emission scenarios with overwhelming suppression of convection by BB aerosols. Reduction in monthly mean precipitation rate by the overall effects of BB aerosols is found for all emission scenarios and intensifies with aerosol loading, which may imply a positive feedback between precipitation scavenging and aerosol concentration for intense BB events. A reduction of monthly mean precipitation rate by −5% and −23% is estimated for the EMIS1 and EMIS6 scenarios, respectively, suggesting a strong sensitivity of precipitation to aerosol concentration. The sensitivity of precipitation change to aerosol concentration is more prominent in the intensive precipitation regime than in the light precipitation case.

The high-sensitivity and nonlinear relationship between regional cloud, precipitation, and BB aerosol abundance highlights the importance of comprehensive assessments of BB aerosol effects in the Amazon with multiannual aerosol emission scenarios. The variation in the ACI and ARI effects with increasing aerosol emission revealed a saturating tendency for the ACI, in contrast to a continuingly increasing effect of the ARI at high aerosol loadings. This may shed light on the climatic importance of the ARI in highly polluted regions and during episodes with severe smoke emissions such as intensive wildfires, industrialization-related fossil fuel combustion, and agricultural crop waste burning. The key role of the ARI also highlights the importance of accurate representation of aerosols and their optical properties in models when addressing their climate effects.

Chapter 3 Impact of aerosol-radiation interactions on cloud microphysics and precipitation by process analysis

3.1 Introduction

According to the results in the last chapter as well as several recent studies that investigated the aerosol climate effects by examining the ACI and ARI jointly and separately (Fan et al., 2015; Shi et al., 2014; Wu et al., 2011b), The ARI plays a significant role in the cloud and precipitation change on a regional scale. However, how and to what extent ARIs affect regional cloud and precipitation remain largely unknown (Koch & Del Genio, 2010).

Modeling studies have found that ARI influences precipitating mesoscale convective systems through disturbing local energy balance, atmospheric stability, and circulation (Deetz et al., 2018; Dipu et al., 2013; Feingold et al., 2005; Fu et al., 2017; Huang et al., 2019; Huang et al., 2016; Jiang & Feingold, 2006; Shi et al., 2014). However, the estimated net effects diverge as to the sign and magnitude. For instance, absorbing aerosols were found to suppress (Feingold 2005; Jiang & Feingold, 2006; Shi et al., 2014) or enhance (Dipu et al., 2013; Huang et al., 2019) or exert unnoticeable influence (Fu et al., 2017; Deetz et al., 2018) on convective precipitation.

For explaining the mechanism behind the ARI effect on precipitation, most of the studies investigating the influence of ARI conducted analyses in terms of cloud macrophysics, thermodynamics, and dynamics, e.g., cloud top height, cloud water path, temperature, supersaturation, and vertical velocity (Feingold 2005; Jiang & Feingold, 2006; Shi et al., 2014; Dipu et al., 2013; Huang et al., 2019; Fu et al., 2017; Deetz et al., 2018). The macrophysical diagnoses enable practical comparison with observation, but it is limited in revealing the full mechanism for precipitation change, e.g., it is unexplainable that different precipitation responses occur under resembling thermodynamic modification by ARI (Shi et al., 2014; Huang et al., 2019). This is because the detailed changes in microphysical processes which

eventually govern the source and sink of precipitating hydrometeors (Lin et al., 1983; Mao et al., 2018; Morrison & Grabowski, 2011) are not linear with thermodynamic changes due to complicated transformation among hydrometeors (Chang et al., 2015; Cheng et al., 2010; Jiang et al., 2016). For instance, the microphysical processes related to rainwater can differ considerably at a subtle change of updraft velocity (Chang et al., 2015). Hence, without probing into the cloud microphysical processes, the mechanism of aerosols affecting cloud and precipitation via ARI would be ambiguous and the aforementioned diverse ARI effects on precipitation could not be reconciled.

The cloud microphysical process analysis was applied for studies on the ACI effect (Cheng et al., 2010; Chang et al., 2015; Jiang et al., 2016), where the presence of aerosols lowers the critical supersaturation for CCN/IN activation in the atmosphere and therefore alters cloud droplet number and size as well as subsequent cloud microphysical processes. However, by far it has not reached the ARI investigation. Theoretically, the thermodynamic perturbation due to the ARI would inevitably alter the cloud microphysical processes, for example, the temperature modification by ARI could alter the atmospheric supersaturation condition and therefore the CCN/IN activation, and the turbulence change induced by ARI may influence the collision processes between cloud hydrometers (Lin et al., 1983; Morrison & Grabowski, 2011). Therefore, without filling in the blank of microphysical process analysis for ARI, the whole mechanism of how aerosols influence cloud microphysics and precipitation is incomplete and the observed aerosol impact on cloud microphysics cannot be interpreted concretively.

Motivated by that, in this study, a process analysis module was developed in a meteorology-chemistry coupled model, WRF-Chem v 3.9.1, intending to elucidate the microphysical processes accounting for the precipitation response to ARI. The precipitating cloud systems in the Amazon in the dry season are mostly composed of the locally generated

clouds, which form on atmospheric updrafts by the surface heating from solar insolation and therefore feature a prominent diurnal lifecycle. This type of cloud exists extensively on the globe, especially over continents (Dai et al., 1999; Greco et al., 1990), and therefore the study here for the Amazon can be generalized to other regions with clouds of this type.

3.2 Model development, configuration, and numerical experiments.

For the simulation in this chapter, the model WRF-Chem v3.9.1 (Grell et al., 2005) was utilized again. Besides, the same selection of the physical and chemical schemes as in the last chapter (Table 2.1) was chosen, which ensures the proceedings of both the aerosol-radiation interactions and aerosol-cloud interactions in the model in the way that is described in Section 2.2.

A process analysis module was integrated into the Lin et al. microphysics scheme (Lin et al., 1983). The Lin et al. scheme addresses 6 classes of hydrometeors: rain, graupel, snow, cloud water, cloud ice, and water vapor and the first three are precipitating matters. The time variation of each hydrometeor on each grid is governed by the following conservation equations (Lin et al., 1983):

For water vapor, cloud water, and cloud ice:

$$\frac{\partial q_i}{\partial t} = -\vec{V} \cdot \nabla q_i + \nabla \cdot K \nabla q_i + P_{q_i} \qquad \text{(Eq. 3.1)}$$

For snow, graupel, and rain:

$$\frac{\partial l_i}{\partial t} = -\vec{V} \cdot \nabla l_i + \nabla \cdot K \nabla l_i + P_{l_i} + \frac{1}{\rho}\frac{\partial}{\partial z}(U_i l_i \rho) \qquad \text{(Eq. 3.2)}$$

where q_i represents the mixing ratio of vapor, cloud water, or cloud ice whose terminal falling velocity is neglected, while l_i represents the mixing ratio of snow, graupel, or rain for which the terminal velocity is parameterized empirically based on observation (Lin et al., 1983). The first two terms on the right side describe the advection and convection transport as well as the turbulent diffusion, respectively. The last term in Eq. 3.2 is the fallout term, which

is only applied for precipitable substances, i.e., snow, graupel, and rain, where U_i is the terminal falling velocity for each hydrometeor. The P_{qi} and P_{li} terms denote the production/sink term for each hydrometeor associated with microphysical processes. The main microphysical processes related to precipitation particles are listed in Table 3.1 and the detailed description and calculation for each process are documented in Lin et al. (1983). A scaling analysis study of the governing equations for the hydrometeors shows that microphysical terms contribute significantly to the concentration of hydrometeors compared with dynamical processes (Lu et al., 2002). Simulation of moisture and energy budget of tropical convection system using general circulation models (GCMs) also illustrates the important role of microphysical sources and sinks in determining the amount and vertical distribution of vapor budget in tropical cumulus ensembles (Sui et al., 1994).

The surface precipitation is related to the vertical integrals of Eq. 3.2, that is,

$$\int_0^{z_0} \frac{\partial l_i}{\partial t} dz = -\int_0^{z_0} \vec{V} \cdot \nabla l_i \, dz + \int_0^{z_0} \nabla \cdot K \nabla l_i \, dz + \int_0^{z_0} P_{l_i} dz + P_s \qquad \text{(Eq. 3.3)}$$

where Z_0 is the top of the domain, and P_s is the instant surface precipitation rate. Because of the absence of severe weather system producing hails, such as squall lines, and because of the high temperature in the lower troposphere in tropics, the precipitating substance falling to the surface in our simulation is only rainwater. From Eq. 3.3, microphysical processes regarding rainwater are directly related to the surface precipitation amount.

Instant hydrometeor concentration (in kg kg^{-1}) in hourly time interval on grids within the domain, and hourly-accumulated microphysical process rate (in kg kg^{-1} hr^{-1}) were output together. Thereby the change of hydrometeor concentration at every hour could be related with the change of individual hourly-accumulated microphysical process rate, which was done in a way of domain average and column integration so that the response of horizontal advection within the domain region and vertical transport of the hydrometeor on each layer was eliminated, respectively. Since turbulent motion is significant mainly within the PBL, while

the cloud is mostly distributed above the top of the PBL, the influence of turbulent diffusion perturbation could be of minor significance compared to the response in microphysical terms for the cloud hydrometeors' responses. Correspondingly, based on Eq. 3.3, the aerosol impact on regional precipitation could be interpreted by aerosol-induced changes in the domain-averaged microphysical budget of rainwater.

Table 3.1. The abbreviation and description for microphysical processes.

Abbreviation	Process description
RAU	Autoconversion of cloud water to form rain
RAW	Accretion of cloud water by rain
SAW	Accretion of cloud water by snow to form rain
GAW	Accretion of cloud water by graupel to form rain
SMT	Melting of snow to form raindrops
GMT	Melting of graupel to form raindrops
REP	Evaporation of raindrops
IAR	Accretion of rain by ice to form snow/graupel
SAR	Accretion of rain by snow to form snow/graupel
GAR	Accretion of rain by graupel
GFR	Freezing of rain to form graupel
SFI	Reduction of cloud ice to form snow by Bergeron process
SAI	Accretion of ice by snow
SDP	Deposition of vapor on snow
SAU	Ice crystal aggregation to form snow
RAS	Accretion of snow by rain to form graupel
SUB	Sublimation of snow to vapor
GAS	Accretion of snow by graupel
GAI	Accretion of ice by graupel
GDP	Deposition of vapor on graupel
GUB	Sublimation of graupel to vapor
GMP	Evaporation of melted graupel

Three domains were set up with 75 km, 15 km, and 3 km horizontal resolution respectively (Fig. 3.1), and 29 vertical layers from near ground surface to 50 hPa for all. The two outer domains were two-way coupled with external meteorological and chemical inputs, while the innermost domain was run separately as driven by larger-scale forcing from the outer

domains. The meteorological and chemistry input for the outer domains as well as emissions were obtained the same as those in Chapter 2 (Table 2.1). This study focuses on the finest grid domain with the cloud-resolving resolution. The resolution of 3 km was employed to better capture the diurnal variation of convection given that previous simulations suggested increasing model resolution to cloud-resolving scales at 2.8−4 km can effectively improve the simulation of the diurnal convection development (Birch et al., 2016; Fosser et al., 2015). Indeed, the 3-km resolution can reasonably capture the precipitation in both magnitude and distribution pattern (Fig. 3.2a). Besides, it also well reproduced the AOD field (Fig. 3.2b), demonstrating its reasonable performance in simulating the aerosol condition in the Amazon area. It should be noted that no nudging was applied to this 3-km resolution domain so that the cloud and precipitation can respond freely to the aerosol forcing.

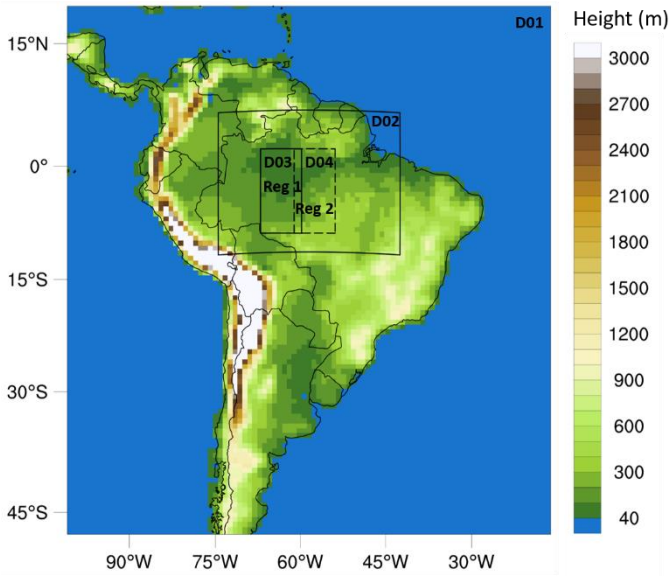

Figure 3.1. Model domain and orography. Outer map represents parent domain with 75 km horizontal grid spacing (D01), and squares show extents of 15 km (D02) and 3 km (D03 and D04, for the central and eastern Amazon basin, respectively) nests.

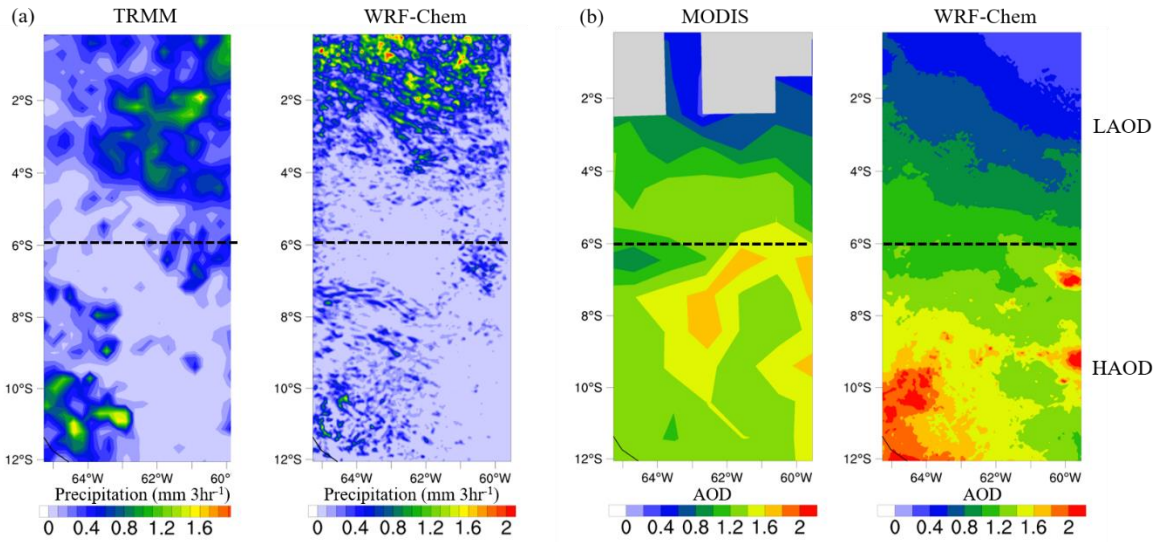

Figure 3.2. Spatial distribution of observed and simulated (a) 3-hr precipitation rate and (b) AOD average over the simulation period. The precipitation and AOD observation data are from TRMM and MODIS AQUA, respectively.

The simulations of the 3-km resolution domain were conducted by WRF-Chem for the periods of 5–15 Sep 2010 and 3–13 Sep 2012 for the central Amazon region and the periods of 13–23 Sep 2010 and 4–13 Sep 2012 for the eastern Amazon region (Fig. 3.1). The year 2010 and 2012 represent a relatively high and an average level of biomass burning aerosol emission intensity in the Amazon based on the records from 2006–2016, respectively (Fig. 2.3). Meanwhile, two domains covering the central and eastern Amazon feature biomass burning aerosols from forest and savanna fires, respectively (Reddington et al., 2019). Simulations for the two years and the two regions showed similar ARI effects (Fig. 3.7a and Fig. 3.8), and the following analysis only specify the case of the central Amazon from 5 Sep to 15 Sep 2010.

To separate the ARI and ACI effect of BB aerosols on precipitation, three sets of simulations (Table 3.2) were performed following the way used in Wu et al. (2011b): the ARI effect was quantified by switching on and off the aerosol-radiation feedback, i.e., the difference between CTRL (polluted case with BB emission) and NORAD (polluted case with BB emission but excluding aerosol-radiation feedback); and ACI effect was obtained as the

difference between NORAD and BASE (clean case). Although the ARI effect of aerosols not from BB emission is included in the ACI calculation, the uncertainty could be neglected, as BB emission is the primary source of aerosols during the dry season over the Amazon region (Martins et al., 2009), especially given that the periods simulated here (September 2010 and September 2012) are characterized with relative strong BB emission (Sena et al., 2013).

Table 3.2. Description of numerical experiment design.

Experiment identification	Experiment description
BASE	Simulation at 3-km resolution without BB aerosol emission; including aerosol-radiation feedback.
NORAD	Simulation at 3-km resolution with BB aerosol emission, excluding aerosol-radiation feedback.
CTRL	Simulation at 3-km resolution with BB aerosol emission, including aerosol-radiation feedback.

3.3 Results

3.3.1 Cloud microphysical processes in the Amazon in the dry season

Figure 3.3 depicts the diurnal and vertical distribution of cloud total hydrometeor concentration and microphysical processes related to the precipitating matters i.e., rainwater, snow, and graupel in the CTRL case. Different colors in each pie chart represent the relative contributions of microphysical processes to the total mass on that grid. The cloud is characterized by a growth phase in the daytime and a gradual decaying phase during night, with their vertical development reaching up to the upper troposphere. As an important rainwater-related process, the collision-coalescence (or autoconversion, RAU) takes place at levels higher than the cloud base (Fig. 3.3b), reflecting that cloud droplets activated at the cloud base need to be lifted to grow in size before transforming into raindrops. The accretion of cloud water by raindrops (RAW) serves as the primary source for rainwater mass from the cloud base to the freezing level (about 5 km). At the freezing level, the graupel melting (GMT) acts as the

most efficient pathway for rainwater formation. The graupel and snow, the cold-rain precipitating hydrometers, are mainly gained from the graupel accreting cloud water (GAW) and the Bergeron process (SFI; Hsie et al., 1980), respectively. After formation, all graupel is converted to rainwater as it melts below the freezing level, whereas snow contributes to rain by transforming to graupel (by GAS) as intermediation. The main microphysical processes accounting for the rain formation here are similar to that in the tropical and mid-latitude locally generated deep convective systems (Chang et al., 2015; Cui et al., 2014; Lin et al., 1983), while little difference was shown in the mid-latitude frontal system where interactions between snow and rain are more pronounced (Mao et al., 2018).

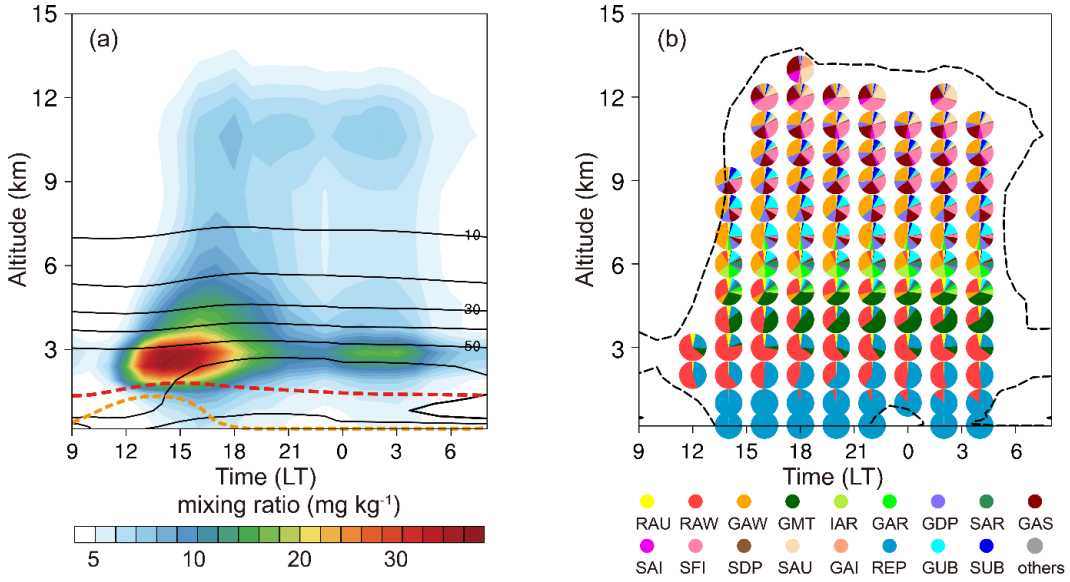

Figure 3.3. Diurnal and vertical distribution of domain- and time-averaged (a) concentration of total cloud substances (sum of cloud, ice, rain, graupel and snow, in unit of mg kg^{-1}, shaded) and PM_{10} (in unit of μg m^{-3}, line in black) and (b) contribution of microphysical processes related with precipitating hydrometeors (sum of rainwater, graupel and snow). The dashed orange and red lines in (a) represent the PBL height and cloud base height respectively. The abbreviations of microphysical processes in (b) are described in Table 3.1.

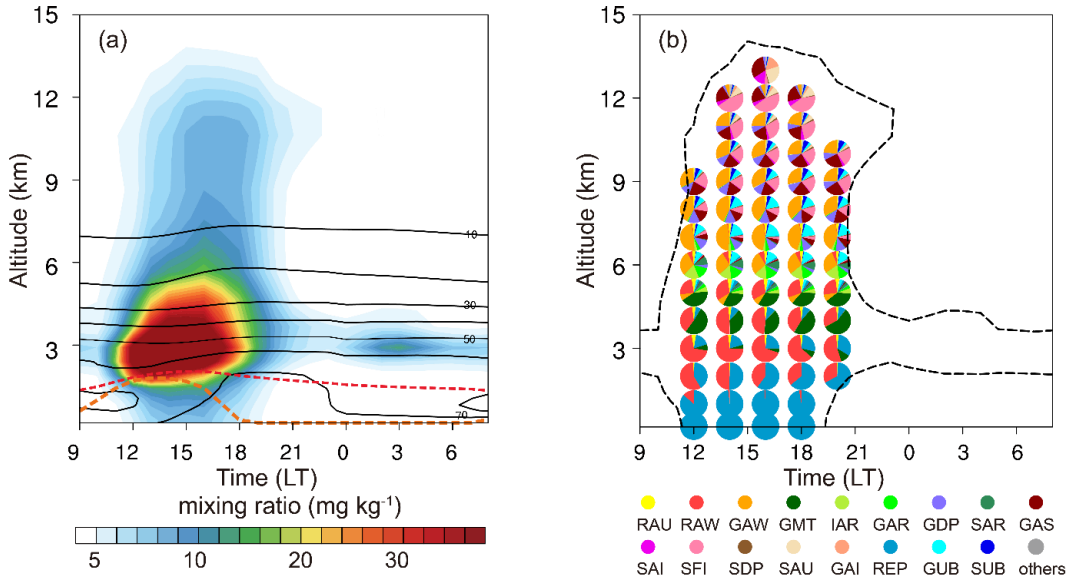

Figure 3.4. Same as Fig. 3.3, but for the NORAD case.

By contrast, the clouds in the simulation without ARI (NORAD; Fig. 3.4a) are mainly distributed from 10:00 to 20:00 LT, with only a marginal concentration within a lower altitude remaining at night. Besides, the cloud microphysical processes in this case (Fig. 3.4b) are different from those in the CTRL case (Fig. 3.3b). The difference in the rainwater-related microphysical processes between the CTRL and NORAD cases can explain the precipitation change by the ARI of BB aerosols (calculated as the precipitation difference between CTRL and NORAD) given the close correlation between the aerosol-induced changes in column-integrated rainwater microphysical budget and that in surface precipitation (Fig. 3.5). The precipitation modification by ARI and the underlying microphysical process responses will be explored in the next section.

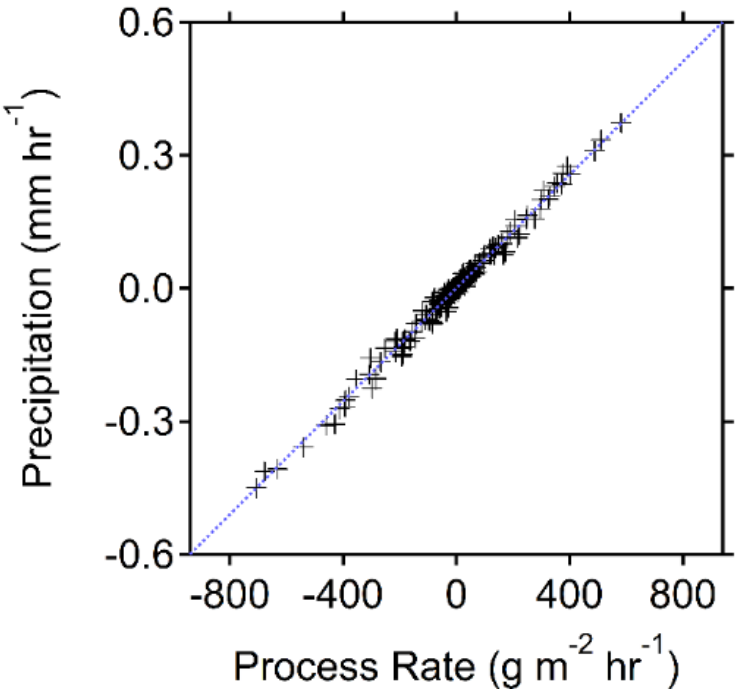

Figure 3.5. Scatter plot of domain-averaged hourly precipitation change versus the perturbation in net rainwater microphysical budget change due to BB aerosols over the simulation period.

3.3.2 Changes of cloud microphysics and precipitation

Despite the spatial inhomogeneity of aerosols in the domain of interest (Fig. 3.2b), the ARI-induced precipitation changes, however, show no obvious regional patterns from large-scale convergence/divergence (Fig. 3.6), implying the dominance of local dynamical and microphysical processes in precipitation responses. Fig. 3.7a compares the simulated diurnal precipitation averaged over the studied period and domain with the corresponding observation from TRMM which provides diurnal measurements due to its geostationary orbit (Yang & Slingo, 2001). The observation shows an increasing trend of precipitation from morning to afternoon and a maximum at around 17:00 LT, a few hours lagging the insolation peak (Fig. 3.10c). The rainfall rate then undergoes a slow decaying till the next morning and shows a

smaller peak in midnight. This diurnal pattern agrees with a typical locally generated convection in the Amazon reported previously (Greco et al., 1990; Zhuang et al., 2017). The simulations reproduced the basic pattern of convection growth and dissipation in the daytime and nighttime, respectively. However, the simulations without ARI (i.e., NORAD and BASE) cannot accurately capture the exact precipitation phase observed by TRMM, showing an earlier initiation and much larger diurnal amplitude, even though the cloud-resolving resolution was used to optimize the model performance in diurnal simulation. Taking the ARI into consideration significantly improves the diurnal results by lowering and enhancing the daytime and nighttime precipitation, respectively (see also Fig. 3.8). Fig. 3.7b demonstrates the diurnal variation of the ARI, ACI, and the total effect of BB aerosols on precipitation. While the ACI generally suppressed the rainfall throughout the day, the impact of ARI on precipitation shows pronounced diurnal variation: the precipitation is suppressed during 10:00–19:00 LT (Phase 1) by up to 100% and enhanced over 20:00–09:00 LT (Phase 2) by up to 100% relative to a daily mean precipitation amount. Accordingly, the amplitude of the diurnal precipitation is reduced by 43%. With the opposite daytime and nighttime precipitation responses to ARI offsetting each other, the ultimate daily mean precipitation shows a comparable response to ARI (0.004 mm hr^{-1}, 5%) and ACI (–0.006 mm hr^{-1}, –8%), although in opposite directions. The magnitude of hourly precipitation changes by ARI is much more significant compared to the ACI effect, indicating an important role of the ARI in modifying the instantaneous rainfall production during the convection evolution.

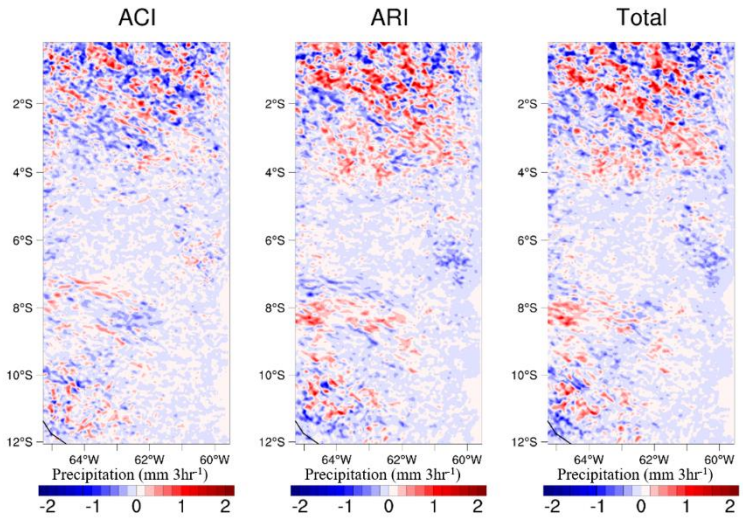

Figure 3.6. Spatial distribution of precipitation changes due to the ARI, ACI, and total aerosol effect of BB aerosols.

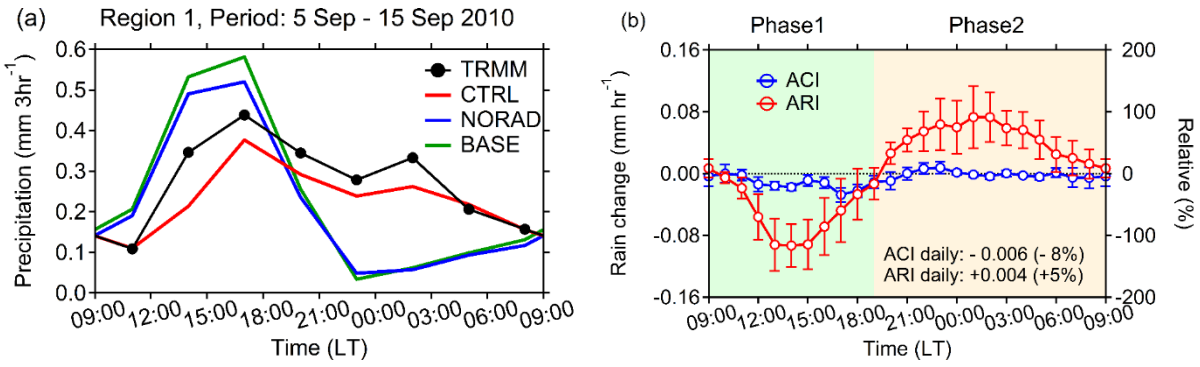

Figure 3.7. Diurnal variation of domain-averaged (a) rain rate from TRMM observation and model simulations and (b) rain rate changes due to ARI and ACI of BB aerosols. The error bars in (b) denote the standard error; the relative changes in (b) are obtained by the ratio of rain rate changes to daily mean rain rate.

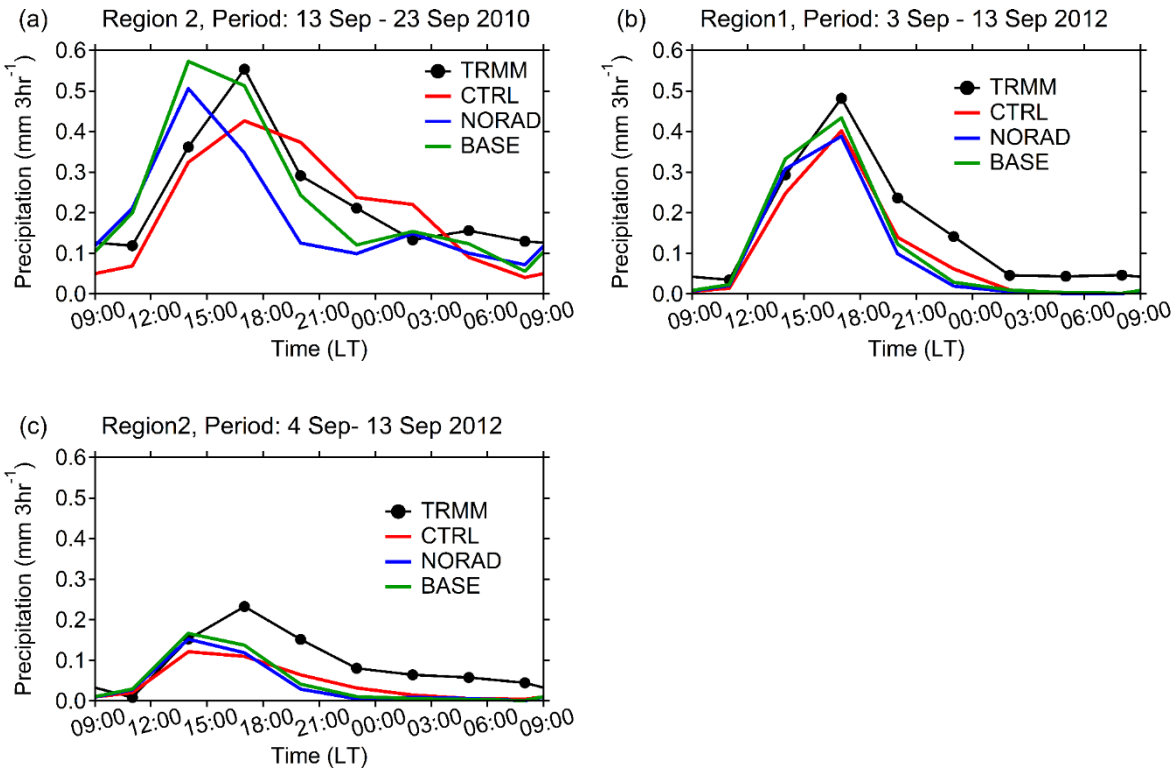

Figure 3.8. Diurnal variation of domain-averaged rain rate from TRMM observation and model simulations for (a) eastern Amazon Basin in 2010, (b) central Amazon Basin in 2012, and (c) eastern Amazon Basin in 2012.

The ARI-induced change in the rainwater microphysical budget is shown in Fig. 3.9a. The RAW and GMT are the main processes responsible for the rainwater production change by the ARI of BB aerosols throughout the convection lifecycle (Fig. 3.9a), accounting for 73% and 16% of the overall rainwater production change, respectively. Specifically, during Phase 1, prominent RAW reduction dominantly undermines rainwater formation, with the GMT reduction playing the secondary role. During Phase 2, the increase in GMT and RAW nearly equally leads to more rainwater production. The change in rainwater production was offset partly by the change in rainwater sinks, especially by rain evaporation (REP) which is parameterized proportional to the rainwater mass (Lin et al., 1983). Due to its dependence on temperature (Lin et al., 1983), the REP response is larger during phase 1 in the daytime than

phase 2 in the nighttime. Consequently, the rain production enhancement in phase 2 retained more of its effect and contributed to an overall increase of the daily mean precipitation.

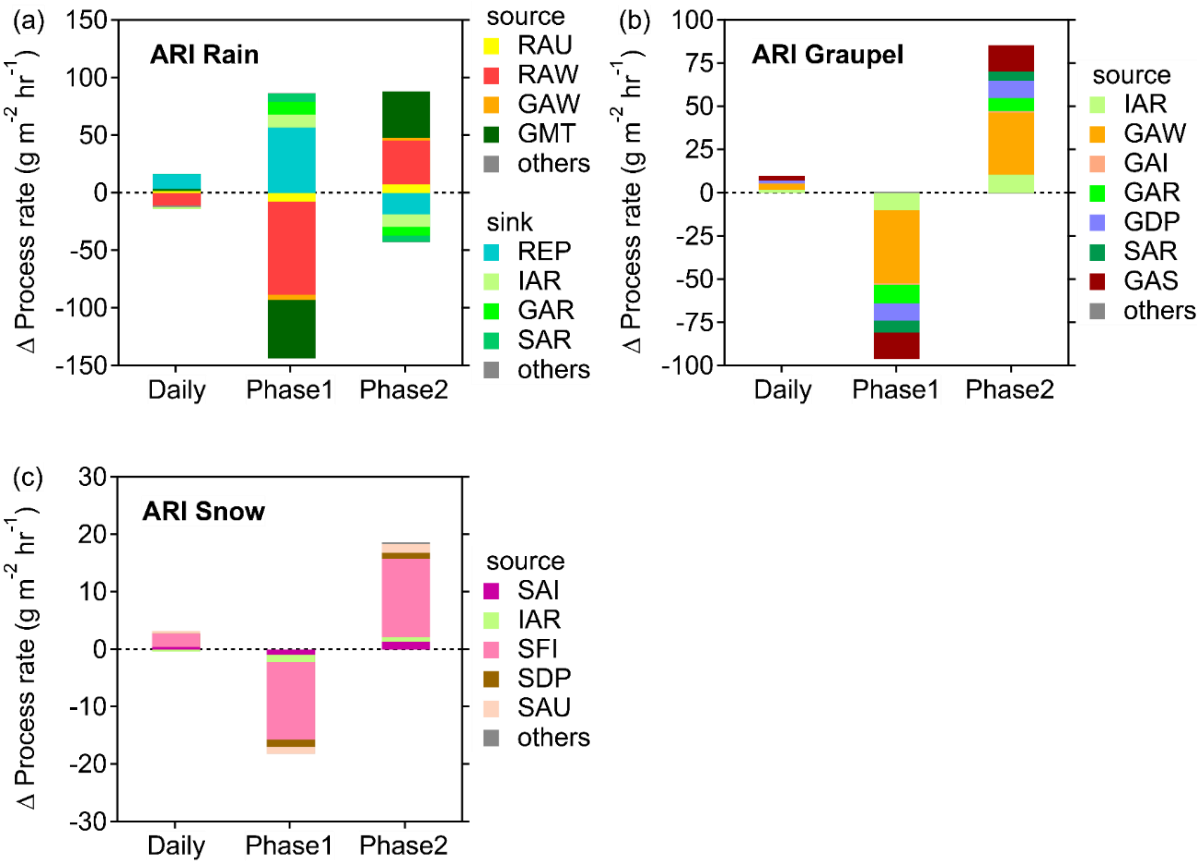

Figure 3.9. Changes in (a) microphysical budgets of rainwater, (b) microphysical source of graupel and (c) snow due to the ARI of BB aerosols for different phases of the convection evolution (indicated in Fig. 3.7b).

Based on that, further insight was taken into the microphysical mechanism behind the RAW and GMT modification. The RAW, the accretion of cloud droplets by raindrops, is sensitive to the liquid cloud amount, and therefore the diminished and invigorated cloud water in phases 1 and 2 (Fig. 3.10) leads to a reduction and enhancement in RAW, respectively. As the GMT is proportional to the graupel amount, the changes in source terms of graupel are calculated (Fig. 3.9b). The graupel production change arises mainly from the graupel accreting cloud water (GAW) and secondarily from the accretion of snow (GAS) which is further traced

back to the primary snow production term, the ice to snow conversion through the Bergeron process (SFI; Fig. 3.9c). Therefore, it can be speculated that the GMT change is mostly determined by both the liquid and ice phase cloud supply. The liquid and ice cloud modification by the ARI derives from the ARI effect on surface fluxes and the atmospheric thermodynamic state as suggested by previous studies.

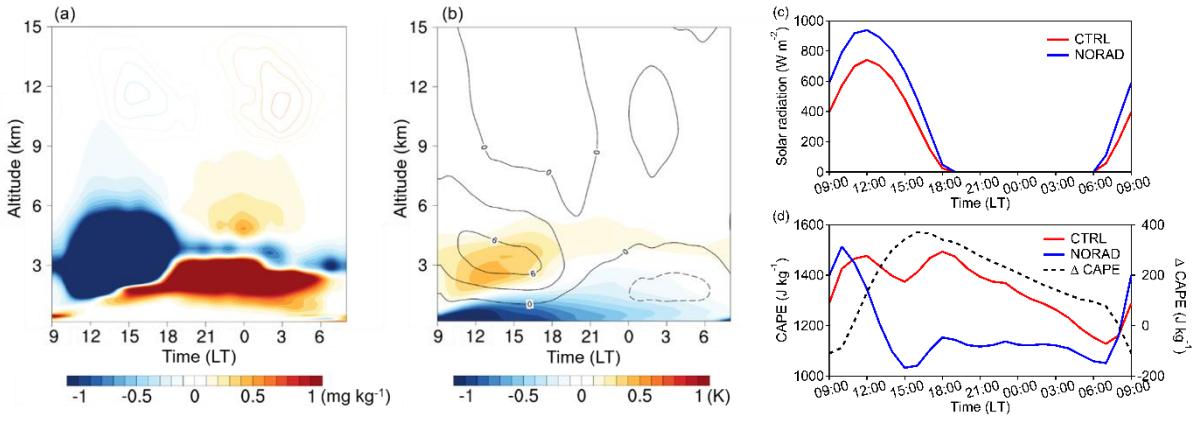

Figure 3.10. Changes in (a) cloud water concentration (shade for liquid phase and contour lines for ice phase) and (b) thermodynamic structure (shade for air temperature and contour lines for vertical velocity in intervals of 3 mm s^{-1}) caused by the ARI of BB aerosols; and diurnal variation of (c) incident solar radiation at surface and (d) CAPE for the CTRL and NORAD cases.

By scattering and absorbing solar radiation, BB aerosols reduce incident solar radiation reaching the ground surface (Fig. 3.10), which leads to a subsequent decrease in surface latent and sensible heat fluxes as a balance. This gives rise to a weaker updraft and moisture supply for the cloud compared with the convective condition absent from BB aerosols (Feingold et al., 2005; Jiang & Feingold, 2006). Meanwhile, the heating near the PBL top (Fig. 3.10) as a result of radiation absorbtion by BB aerosols stabilizes the PBL, increasing the barrier for convection development (Huang et al., 2016). The heating from BB aerosols distributed within the cloud

directly lowers the supersaturation and cause more cloud droplet evaporation (Koch & Del Genio, 2010). These thermodynamic changes by BB aerosols explain the suppression of cloud early development during phase 1. Accompanied by the convection suppression by BB aerosols, the release of convective energy and moisture is inhibited, leading to larger CAPE in the atmosphere (Fig. 3.10). This reservoir of CAPE accounts for the enhanced convection during phase 2, as the release of excessive energy and moisture promotes convective updraft and the transport of moisture from PBL to high altitude and therefore facilitates the development of liquid and ice cloud. Phase 2 occurs between 16:00–19:00 LT depending on the background convective condition and aerosol loading (Fig. 3.12). The triggering of it is determined by the instantaneous atmospheric convective strength versus convective inhibition, which are controlled by the atmospheric thermodynamic state (Holton, 1992). Several mechanisms may account for the triggering, for example, fully developed PBL has stronger entrainment of dry air that weakens the temperature inversion and convective inhibition, or the radiative cooling after sunset acts to lower the cloud condensation level (LCL) and therefore the convective inhibition. Further detailed investigation for the triggering mechanism is warranted.

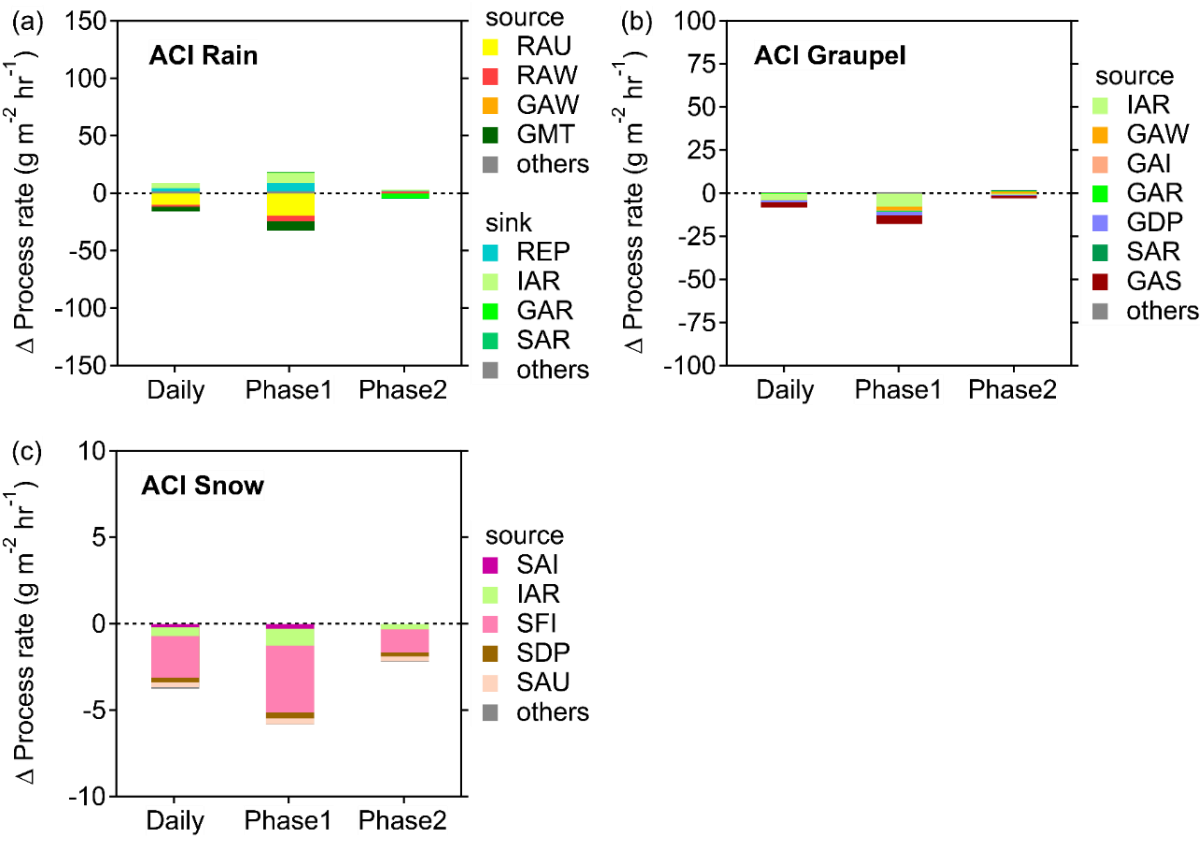

Figure 3.11. Same as Figure 3.9, but for the ACI effect.

In contrast to the ARI effect, the dominant process for the ACI-induced rainwater change is RAU (Fig. 3.11) which is consistent with previous recognitions (Gettelman et al., 2013; Suzuki et al., 2013). In both phases, although the overall change in rainwater microphysical processes is larger in ARI than ACI, the RAU is consistently in a smaller magnitude in the ARI effect than in ACI. This reflects that the RAU process is mainly modified through ACI while the diabatic process is of minor importance, which is supportive of previous results (Braga et al., 2017). In addition, the main process regulating the graupel change is different between the ACI and ARI, with IAR being responsible for ACI and GAW for ARI. During the individual phase, the ARI-induced overall change of microphysical processes dominates over the ACI-induced one, and therefore determines the eventual precipitation response to BB aerosols. This suggests that the observed precipitation invigoration may not only result from ACI even though the sign for ACI-invigoration, a decrease in cloud droplets

radius and RAU, is detected, since ARI could contribute substantially by modifying other rain-related processes such as RAW, GAW, GAS, and SFI.

3.3.3 Sensitivity to convection intensity and aerosol loading

The studied domain covers a region from southern Amazon (12 ºS) to northern Amazon (0 ºS), with distinctive more and less polluted conditions at south and north of 6ºS, respectively (Fig. 3.2b), and based on this, the domain was divided into the high aerosol (HAOD, south of 6ºS) and low aerosol (LAOD; north of 6ºS) regions. Deep and shallow convections were further classified with the daily mean CAPE of 1000 J kg^{-1} as a criterion (Zhuang et al., 2017). Hence, three regimes (Deep_HAOD, Shallow_HAOD, Deep_LAOD; Table 3.3) based on aerosol concentration and convection intensity difference were generated for examining the sensitivity of the ARI effect to aerosol and convection conditions.

Table 3.3. Description of the cases divided based on the background convective intensity and aerosol loading.

Case	Region	Period	CAPE (J kg^{-1})	AOD
Deep_HAOD	Northern Amazon	11 Sep– 15 Sep	1100	1.5
Shallow_HAOD	Northern Amazon	05 Sep– 10 Sep	400	1.7
Deep_LAOD	Southern Amazon	05 Sep– 15 Sep	1500	0.8

The ARI-induced precipitation changes show differences among different aerosol and background convection conditions (Fig. 3.12). During Phase 1, precipitation suppression is found in all the three cases, suggesting an inhibition impact of ARI on the initiation of convective precipitation. Then, the precipitation in Deep_LAOD is significantly enhanced during Phase 2, resulting in an overall daily mean precipitation increase of 0.012 mm hr^{-1}. The precipitation enhancement is also noticeable for the Deep_HAOD, but in an earlier and shorter time span (16:00–00:00 LT), which almost offset the precipitation reduction in Phase 1. The

Shallow_HAOD shows only a slight precipitation enhancement signal in Phase 2, so that its daily mean precipitation amount is substantially decreased (–0.005 mm hr^{-1}).

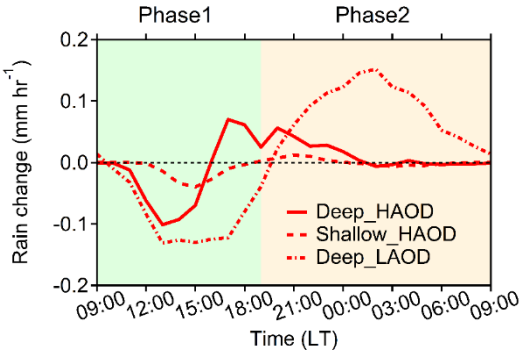

Figure 3.12. Diurnal variation of domain-averaged rain rate changes by ARI in different conditions: Deep_HAOD, Shallow_HAOD, and Deep_LAOD as described in Table 3.3.

The start of Phase 2 induced by the release of the CAPE is dependent on background conditions. In Deep_HAOD, the strong aerosol heating at the top of PBL triggers the CAPE release starting from 16:00 LT (Fig. 3.14a) with enhanced updrafts (Fig. 3.13a) and entrainment to the PBL (Lee et al., 2014; Martinez & Chaboureau, 2018). Accordingly, cold-rain microphysical processes, GMT and SFI, are enhanced (Fig. 3.13a), leading to more precipitation (Fig. 3.12), even though the overall cloud concentration does not show positive responses until 20:00 LT (Fig. 3.14d). For deep convection in the low aerosol loading condition, the release of larger CAPE occurs at nighttime (20:00 LT), when water vapor from daytime cloud evaporation condensates into cloud droplets and subsequently invigorate cloud development (Fig. 3.14f). Correspondingly, the processes of RAW and GMT are increased (Fig. 3.14c) and account for the larger rainfall (Fig. 3.12). In shallow convection, the CAPE increase does not result in substantial convection invigoration, possibly due to the relatively stable atmosphere condition that is unfavorable for triggering the CAPE release.

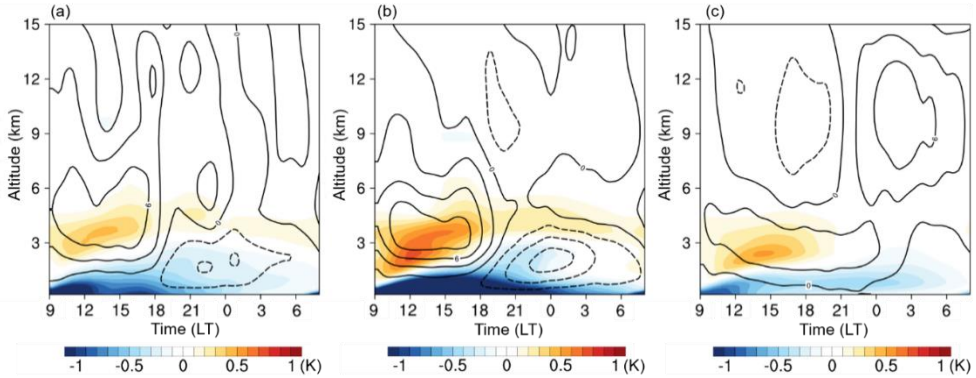

Figure 3.13. Changes in air temperature (shaded) and vertical velocity (contour lines, in intervals of 3 mm s^{-1}) caused by the ARI of BB aerosols for (a) Deep_HAOD, (b) Shallow_HAOD, and (c) Deep_LAOD.

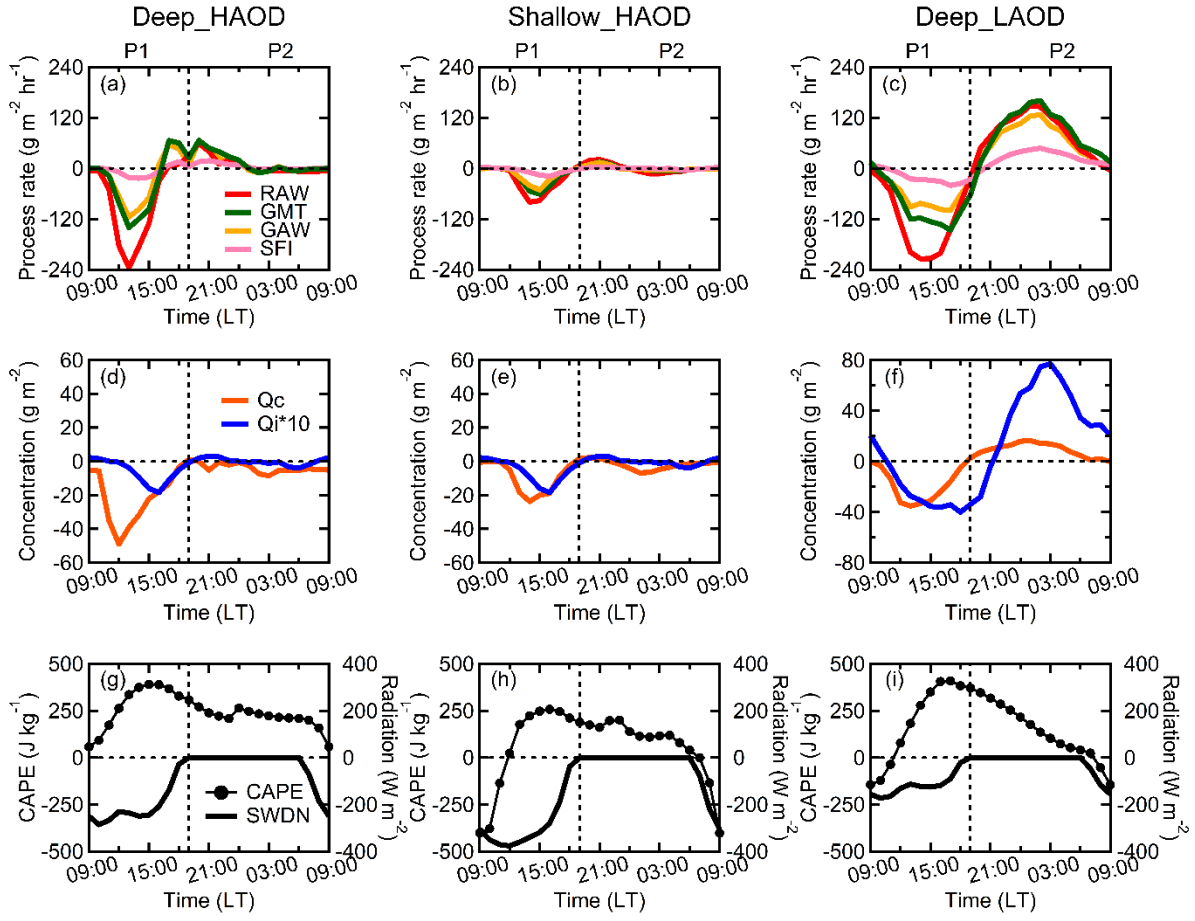

Figure 3.14. Diurnal variation of ARI-induced perturbations on (a–c) cloud microphysical processes, (d–f) liquid and ice cloud concentration, and (g–i) CAPE and surface solar radiation for the case Deep_HAOD (a, d, and g), Shallow_HAOD (b, e, and h), and Deep_LAOD (c, f, and i).

3.4 Conclusions

Based on the analysis of the ARI-induced precipitation, microphysical processes, and atmospheric thermodynamic condition perturbations, mechanisms for the ARI of BB aerosols on precipitation from a microphysical perspective are summarized in Fig. 3.15. The overall ARI effect on daily precipitation involves two competing pathways. First, the convection suppression by ARI through surface fluxes reduction and atmospheric heating diminishes liquid cloud amount and therefore inhibits the raindrop accretion growth (RAW) that is fed on cloud water. At this stage, the warm-rain process RAW determines the precipitation reduction while the cold-rain processes also contribute to but take a less important role in rainwater response. Second, the convection invigoration energized by the release of previously reserved energy and moisture promotes cloud water and ice formation. The warm rain production from the accretion of cloud water (RAW) is enhanced accordingly. Meantime, more snow generated from ice through the Bergeron process SFI was converted into more graupel, which together with enhanced graupel accretion of cloud water (GAW) act to boost the graupel concentration and subsequent graupel melting (GMT), causing more rainwater mass. The two microphysical pathways dominate at an earlier and later stage of a diurnal cloud evolution in the Amazon region, respectively, yielding an attenuated diurnal amplitude of precipitation under the ARI effect of BB aerosols. The two alternating microphysical mechanisms for the precipitation response to ARI hold for different conditions in the Amazon, yet the relative importance of the two phases tends to be sensitive to the aerosol loading and the background conditions. The precipitation invigoration appears more pronounced in less polluted deep convection while the precipitation suppression appears overwhelmingly in shallow or highly polluted conditions. Here, the microphysical process analysis is shown to be able to well explain the precipitation modification by aerosols for the locally generated convection. For precipitating occasions where advection of precipitating hydrometers is significant such as the outflow part within a

cloud or the region undergoes the passage of frontal systems, additional analyses of hydrometeor transport are needed to comprehensively reveal the mechanism lying behind.

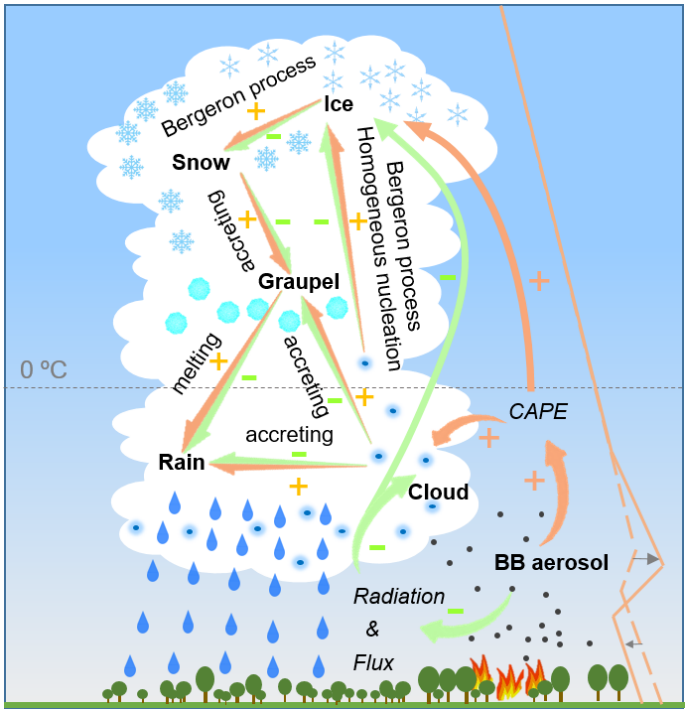

Figure 3.15. Scheme of cloud microphysical mechanisms for precipitation modification by the ARI of BB aerosols.

The microphysical process analysis in this study showed the complexity of the microphysical mechanisms regulating the precipitation response to aerosols, as the mechanisms involve more processes aside from broadly recognized processes, such as RAU, and encompass different phases in a diurnal period. This provides some implications for observation studies of the aerosol-precipitation interaction. Firstly, although observations of cloud droplet size change by aerosols can suggest the participation of ACI in changing precipitation, the dominant mechanism for the observed precipitation change cannot be determined without understanding the ARI's relative role and the key processes for rainwater change. Therefore, microphysical process-resolved models that include both ARIs and ACIs,

coordinated with the observations are needed to interpret the observed precipitation changes. Secondly, the diurnal variation of the aerosol effect on rainfall indicates that the satellite observation of aerosol impact on precipitation represents an instantaneous aerosol effect for a certain time of a day but may not be able to reflect the daily overall effect. In-situ observations with high temporal resolution are needed to provide an observational constraint on daily overall rainfall changes by aerosols.

The diurnal variation of convection and precipitation is a crucial factor for local climate and atmospheric chemistry. However, accurate simulation of the diurnal convective pattern remains a great challenge in atmosphere models since the diurnal evolution is coupled to complex physical processes such as radiation transfer, surface-atmosphere exchange, PBL turbulence, and cloud microphysics. Here, a significant improvement in diurnal precipitation simulation was achieved by taking ARI into account, which builds a smoother transition between different development stages of the convection compared with an ARI-absent cloud-resolving-resolution simulation. This result suggests the consideration of ARI in models as a potential way to improve the model simulation performance of diurnal convective variation.

Chapter 4 Model improvement for the aerosol-cloud interactions–CCN production in the upper troposphere by biogenic organics

4.1 Introduction

As described in Section 1.2.2, serving as CCN is an important pathway for aerosols to engage in ACIs. Therefore, an accurate representation of the CCN concentration is essential for investigating the ACI effect. As shown in Fig. 2.7, using the broadly utilized aerosol and gas chemistry configuration–the MOSAIC aerosol module coupled with the CBMZ gas chemistry module (Zhang, Dubey, et al., 2009), the WRF-Chem is able to capture the observed CCN characteristics in the lower atmosphere. However, recent aircraft observation in the ACRIDICON-CHUVA campaign detected a large number of aerosols with cloud active size in the upper troposphere of the Amazon (Andreae et al., 2018). Meantime, aerosol component analysis unveiled their origin from the oxidation of biogenic organics (Schulz et al., 2018). The existence of biogenic SOA in the upper troposphere poses challenges for the current WRF-Chem model since the mechanism of biogenic organic vapor converting into SOA is not included in the MOSAIC and CBMZ modules. Even for the WRF-Chem aerosol and gas modules that include the SOA mechanism, e.g., MOSAIC aerosol module coupled with SAPRAC99 gas chemistry module (Shrivastava et al., 2017) and RADM aerosol module coupled with MADE/SORGARM gas chemistry module (Schell et al., 2001), and for other 3-D models considering the SOA formation (Mann et al., 2012; Wang et al., 2011), the SOA parameterization is highly uncertain (D'Andrea et al., 2013). It can be speculated that the discrepancy in upper tropospheric CCN simulation in previous studies may to some extent be caused by the insufficient SOA representation in the models (Mann et al., 2012; Wang et al., 2011; Watson-Parris et al., 2019). It is necessary to improve the SOA parameterization in the WRF-Chem model so that the large number of SOA-dominated CCN in the upper troposphere in the Amazon would not be missed by the model.

Although the transformation of interstitial CCN to cloud-borne state occurs commonly at the cloud base (Wallace & Hobbs, 2006), the interstitial CCN residing above the cloud base, i.e., in the middle to upper troposphere, can also be activated into cloud droplets through secondary in-cloud activation and therefore engage in the aerosol-cloud interactions. The secondary CCN activation above the cloud base was found to occur through several pathways. Firstly, the entrainment of cloud droplet-free air can add additional CCN to the cloud; such additional CCN, especially those with lower critical supersaturation, could be activated when the entrained air parcel is lifted rapidly by the strong updraft within the cloud (Paluch & Baumgardner, 1989; Warner, 1969b). Secondly, A prompt increase of the vertical velocity above the cloud base can give rise to a higher supersaturation condition within a short time so that the water vapor has a higher chance to contribute to the activation of CCN rather than to the cloud droplets growth (Warner, 1969a). Thirdly, a strong decrease in droplet concentration due to intense rainfall and droplet collision would lead to an increase in supersaturation and therefore cause the secondary in-cloud activation (Khain et al., 2012). The in-cloud activation was found as an important process in both shallow and deep convective clouds (Phillips et al., 2005; Phillips et al., 2007; Pontikis & Hicks, 1993), accounting for approximately 40% of the cloud droplets (Slawinska et al., 2012). An accurate simulation of CCN in the free troposphere is an important prerequisite for calculating the in-cloud activation, and therefore, should be addressed in the model.

Two mechanisms may govern the CCN production from biogenic SOA. The first relates to the biogenic new particle formation (NPF) where aerosol particles form out of nucleation of gas-phase biogenic precursors and subsequently grow to larger sizes; the second involves the condensation of biogenic low volatile organics, which causes the existing particles to grow to the cloud active size. The biogenic vapors need to be oxidized into low volatile compounds in order to engage in either the nucleation or the condensation, which is especially true for the

nucleation for it requires extremely low volatile compounds (Ehn et al., 2014). The NPF by biogenic organic vapors was discovered in laboratory experiments where biogenic organics such as α-pinene and β-pinene trigger nucleation through being oxidized as highly oxygenated organic molecules (HOMs) and boost efficient aerosol growth with their low volatile oxidation products (Burkholder et al., 2007; Kirkby et al., 2016). The biogenic NPF signature has been observed in the ambient atmosphere and was shown to play crucial role in the atmospheric aerosol budget, especially in the upper troposphere region (Ehn et al., 2014; Jokinen et al., 2015; Kulmala et al., 2004). Attempts of including the biogenic organic nucleation mechanism into atmospheric models have been taken to investigate the new particle formation by biogenic organic vapors (Dunne et al., 2016; Ekman et al., 2008; Gordon et al., 2017; Gordon et al., 2016; Jokinen et al., 2015; Metzger et al., 2010; Riccobono et al., 2014; Trostl et al., 2016; Zhu & Penner, 2019, 2020; Zhu et al., 2019). It was shown that the pure organic nucleation mechanism is predominant over the sulfuric acid-mediated organic nucleation for the troposphere and is larger in magnitude than the inorganic nucleation mechanism in the continental upper troposphere (Zhu & Penner, 2019). The biogenic organic nucleation can contribute substantially to atmospheric aerosol concentration (Gordon et al., 2017; Zhu & Penner, 2019) and cause appreciable direct and indirect climate effects (Gordon et al., 2016; Zhu & Penner, 2019). However, uncertainties exist in the simulation results due to the treatments parameterizing the laboratory results into the model frameworks. For example, the different identification of the organic nucleation agents (Riccobono et al., 2014; Trostl et al., 2016), the approximation of the biogenic precursors (α-pinene and β-pinene) in the models (Dunne et al., 2016; Jokinen et al., 2015; Metzger et al., 2010; Riccobono et al., 2014; Trostl et al., 2016; Zhu & Penner, 2019; Zhu et al., 2019), the extension of the laboratory-based HOMs production processes to the model chemistry schemes (Dunne et al., 2016; Gordon et al., 2016; Gordon et al., 2017; Jokinen et al., 2014; Riccobono et al., 2014; Troestl et al., 2016; Zhu &

Penner, 2019; Zhu et al., 2019), and the approximation of equilibrium state of HOMs when calculating their concentration (Dunne et al., 2016; Gordon et al., 2016; Gordon et al., 2017; Jokinen et al., 2014; Riccobono et al., 2014; Troestl et al., 2016). As a consequence, the model results diverse largely, such as the vertical distribution of the nucleation occurrence (Zhu & Penner et al., 2019; Zhao et al., 2020) and the magnitude of the aerosol perturbation by the biogenic organic nucleation (Gordon et al., 2017; Zhao et al., 2020). Hence, a model that represents, in a consistent way with laboratory measurements, the targeted organic precursors, oxidation processes as well as the organic nucleation and condensation processes is desired for better understanding the biogenic NPF.

Secondly, if there are enough preexisting aerosols from transport or inorganic nucleation, the condensation of low volatile organic compounds onto these preexisting aerosols could also lead to a large number of CCN-sized particles in the upper troposphere. With certain parameterization of preexisting aerosols, the condensation of organics has been proven to bring the CCN concentration closer to observation compared with the case where this aerosol growth mechanism is absent (D'Andrea et al., 2013). In summary, it remains inconclusive the detailed mechanisms and quantitative assessments of the BVOC-driven nucleation and condensation proceeding in the atmosphere (Kulmala et al., 2006; Trostl et al., 2016; Williamson et al., 2019).

Motivated by this, the study implements the pure organic nucleation mechanism based on laboratory measurements and the state-of-art condensation process of organics into the WRF-Chem model to complement the missing SOA representation and to improve the simulation of SOA-related CCN in the upper troposphere. Besides, this work aims to characterize the contribution to the CCN production in the upper troposphere by the pure organic nucleation (HOMs-induced nucleation) and the condensation of organics, both of which are driven by the biogenic VOCs emitted in the canopy. Finally, this work aims to find

out the controlling environmental factors that drive the occurrence of the pure organic nucleation and the condensation of organics in the high altitudes.

4.2 Model development, configuration, and numerical experiments.

For the simulation in this chapter, the model WRF-Chem v3.9.1 (Grell et al., 2005) was employed again. The WRF-Chem configurations used are listed in Table 4.1. Unlike the gas-phase chemistry mechanism CBMZ used in Chapter 2 and 3, the Common Reactive Intermediates gas-phase Mechanism (CRIMECH) scheme (Jenkin et al., 2008; Watson et al., 2008) was used in this Chapter for its explicit description of the α-pinene and β-pinene, which enables an direct transplantation of the experimental results regarding the HOMs production from oxidation of α-pinene and β-pinene; other selections of the physical and chemical options are same as in Chapter 2 and 3.

Table 4.1. WRF-Chem configuration.

Atmospheric Process	WRF-Chem Option
Longwave radiation	RRTMG
Shortwave radiation	RRTMG
Surface layer	Monin-Obukhov
Land surface	RUC
Boundary layer	YSU
Microphysics	Lin et al.
Cumulus	Grell-Devenyi ensemble
Gas-phase chemistry	CRIMECH
Aerosol module	MOSAIC
Aqueous-phase chemistry	Fahey and Pandis
Photolysis	Fast-J
Anthropogenic emissions	EDGAR-HTAP V2
Biogenic emissions	MEGAN
Biomass burning emissions	FINNv1.5

CRIMECH contains up to 112 non-methane volatile organic compounds (VOCs), including α-pinene and β-pinene (Archer-Nicholls et al., 2014; Watson et al., 2008), and adopts 652 chemistry reactions regarding inorganic species, organic vapors, and their oxidation intermediates, based on the Master Chemical Mechanism (MCM), which enables it to provide the gas-phase precursors, i.e., α-pinene and β-pinene, for the organic nucleation. The MOSAIC

aerosol module uses discrete size bins to describe the aerosol size distribution (Zaveri et al., 2008). This study employed the 4-bin version with the size bins distributed as listed in Table 4.2. In the WRF-Chem version 3.9.1 MOSAIC aerosol module, the H_2SO_4-H_2O binary nucleation mechanism is included (Wexler et al., 1994), in which a critical concentration of H_2SO_4 is calculated based on air temperature and relative humidity. The H_2SO_4 with a concentration higher than this threshold is parameterized into aerosols. The organic nucleation and condensation of organic vapors are not accounted for. The coagulation process of particles is parameterized by the mass conserving semi-implicit numerical scheme of Jocobson et al. (1994) using the Brownian coagulation kernels.

Table 4.2. Description of aerosol size bins in MOSAIC.

Default bins				Modified bins			
Bin name	Low[a]	High[b]	Center[c]	Bin name	Low	High	Center
				01	0.6	2.4	1.2
				02	2.4	10	5
				03	10	39	20
01	39	156	78	04	39	156	78
02	156	625	312	05	156	625	312
03	625	2500	1250	06	625	2500	1250
04	2500	10000	5000	07	2500	10000	5000

a, b, c: low boundary, high boundary and geometric mean diameter of the bin in nm, respectively.

Based on the aforementioned CRIMECH gas-phase chemistry scheme and MOSAIC aerosol scheme, a new module resolving the purely organic nucleation has been added to WRF-Chem. The developments include implementing the production of HOMs in the CRIMECH scheme, resetting the sectional bins in the aerosol model, and adding parameterizations of pure organic nucleation mechanisms and aerosol condensational growth by HOMs.

The concentration of HOMs was calculated previously as the ratio of its production and condensation sink assuming that the HOMs were in a thermo-equlibrium state (Gordon et al., 2016; Kirkby et al., 2016). In this study, the kinetic calculations of the production and condensation sink of HOMs are implemented separately, which enables a more accurate

representation of the concentration of HOMs. To achieve this, 4 reactions regarding the oxidation of α-pinene and β-pinene by ozone and hydroxyl radical are added to the CRIMECH mechanism based on the reaction coefficients and yield rates suggested by laboratory experiments (Atkinson et al., 2006). Then, the production of HOMs is computed using the KPP module. The condensation sink of HOMs is represented according to the algorithm of Kerminen et al. (Kerminen et al., 2004).

$$\alpha\text{-pinene} + O_3 = \text{HOMs: } 0.029{\times}1.01 \times 10^{-15} e^{\frac{-732}{T}} \quad \text{(R4.1)}$$

$$\alpha\text{-pinene} + OH = \text{HOMs: } 0.012{\times}1.2 \times 10^{-11} e^{\frac{444}{T}} \quad \text{(R4.2)}$$

$$\beta\text{-pinene} + O_3 = \text{HOMs: } 0.0012{\times}1.5{\times}10^{-17} \quad \text{(R4.3)}$$

$$\beta\text{-pinene} + OH = \text{HOMs: } 0.0058{\times}2.38 \times 10^{-11} e^{\frac{357}{T}} \quad \text{(R4.4)}$$

The 4-bin MOSAIC scheme in WRF-Chem simulates aerosols with diameters from 39 nm to10 μm, which does not cover the size range of newly formed aerosols whose diameters are in the magnitude of the nanometer (Kulmala, 2003) and therefore incapable of explicitly representing the nucleation process of aerosols. In this study, the lower end of the aerosols size range simulated in the MOSAIC scheme is extended from 39 nm to 0.6 nm by introducing 3 additional size bins whose boundaries are set following the same lognormal size distribution law as the original 4 bins (Table 4.2). The modification of size bins based on the 4-bin instead of the 8-bin MOSAIC scheme assures a high computation efficiency.

Aside from the existing H_2SO_4 binary nucleation, pure biogenic nucleation mechanisms induced by HOMs are integrated into the MOSAIC module. The mechanisms of organic nucleation were investigated in CLOUD (Cosmics Leaving OUtdoors Droplets) Chamber experiments (Kirkby et al., 2016), suggested by which, the HOMs-induced pure organic nucleation rate (J_{org}, unit: cm^{-3} s^{-1}) can be represented by the combination of the neutral (J_n) and the ion-induced (J_{iin}) nucleation rate. The detailed parameterization of the J_n and J_{iin} is as following.

$$J_{org} = J_n + J_{iin} \quad \text{(Eq. 4.1)}$$

$$J_n = a_1 [HOM]^{a_2 + \frac{a_5}{[HOM]}} \quad \text{(Eq. 4.2)}$$

$$J_{iin} = 2[n_{\pm}] a_3 [HOM]^{a_4 + \frac{a_5}{[HOM]}} \quad \text{(Eq. 4.3)}$$

Where HOMs here are in the unit of 10^7 molecules per cubic centimeter and obtained by chemical kinetic calculation as described above; the a_i represent free parameters and their values were suggested by Kirkby et al. (2016) where a_1, a_2, a_3, a_4, and a_5 equaled to 0.04001, 1.848, 0.001366, 1.566, and 0.1863, respectively.

n_± is the ion concentration produced by radon and galactic cosmic rays and is parameterized as:

$$[n_{\pm}] = \frac{(k_i^2 + 4\alpha q)^{0.5} - k_i}{2\alpha} \quad \text{(Eq. 4.4)}$$

Where q (in cm^{-3} s^{-1}) represents the ion-pair production rate and adopts the value of 10 cm^{-3} s^{-1} (Horrak et al., 2008). α represents the ion-ion recombination coefficient (in cm^3 s^{-1}) and was set to $1.6e^{-6}$ cm^3 s^{-1} here. The ion loss rate, ki, is due to the ion condensation sink (CS) onto aerosols and the ion-induced nucleation:

$$k_i = CS + \frac{J_{iin}}{2[n_{\pm}]} \quad \text{(Eq. 4.5)}$$

In this study, the condensation sink term is calculated according to the empirical parameterization proposed by Horrak (2008). The HOMs nucleation rate J_{org} is then modulated by temperature. Unlike the approximated temperature correction suggested in Dunne et al. (2016), a temperature dependence associated with the Gibbs free energy for forming the critical cluster based on the classical homogeneous nucleation theory (Yu et al., 2017) is used here. Temperature correction to the J_n and J_{org} was applied by multiplying it by a correction factor, $\exp(\Delta G_n/k*(1/T–1/278))$ and $\exp(\Delta G_{iin}/k*(1/T–1/278))$, respectively, and the ΔG_n and ΔG_{iin} are based on the smog chamber results (Kirkby et al., 2016). Based on the functions above, the organic nucleation can be calculated. The newly formed particles are added into the smallest

bin and undergo subsequent processes such as coagulation, transport, and deposition. The condensation of HOMs on all aerosol particles is represented by partitioning the condensable HOMs (described above) onto each aerosol bin and applying the moving-center growth algorithm (Jacobson, 1997).

Additionally, a new module addressing the condensation of the low volatile organic compound (LVOC) is integrated into the WRF-Chem. The LVOC was oxidation products of α-pinene, β-pinene, and isoprene by ozone, hydroxyl and nitrate radicals. A yield of 13% for monoterpene oxidation products and 3% for isoprene oxidation products were used in Scott et al. (2014). However, laboratory chamber experiments found the temperature dependence of SOA yield from α-pinene oxidation (Saathoff et al., 2009). Therefore, temperature-corrected yields based on the laboratory experiment results (Saathoff et al., 2009) are applied to the LVOC production by monoterpene and isoprene oxidation for the model here.

In this study, two nested domains with a horizontal spacing of 75 km and 15 km were set up over South America (Fig. 4.1), with Domain1 covering most of the South American continent, while Domain2 over the Amazon Basin area. Vertical layers of 29 levels extending from the ground surface to the height of 50 hPa were applied for all domains. The meteorological and chemistry input as well as emissions were obtained the same as those in Chapter 2 (Table 2.1). The simulation was conducted from 24 Aug to 01 Oct 2014, and the first 6 days of the simulation were used as spin up. The comparisons between model outputs and aircraft measurements in the next section were made using the results from Domain2. Additionally, a rectangular area focusing on the Central Amazon, as shown in Fig. 4.1, was used in the analysis in the next section.

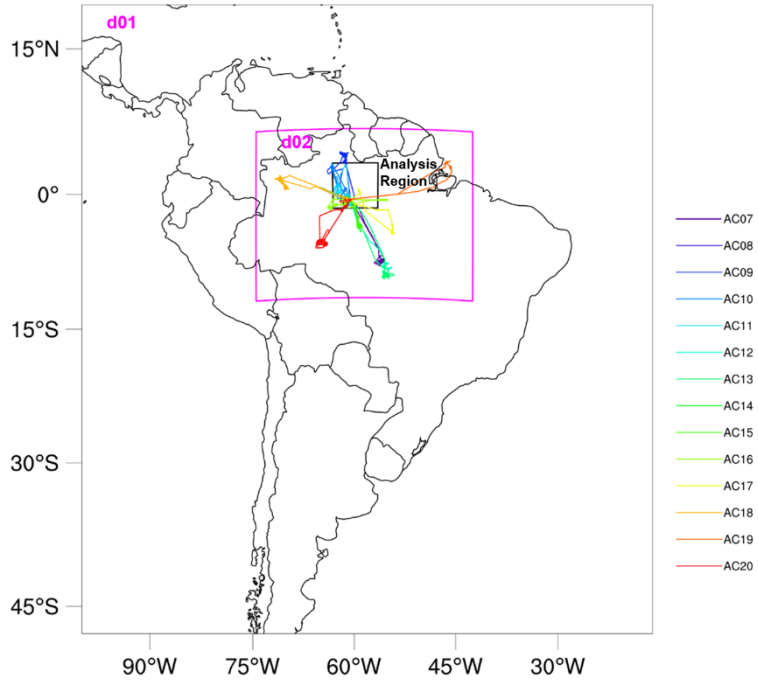

Figure 4.1. Model domain and tracks of flight AC07 to AC20 from the ACRIDICON-CHUVA campaign. The outer map and the embedded magenta square represent the domains with 75 km and 15 km horizontal grid spacing, respectively. The black rectangle in (a) denotes the region of the Central Amazon for further analysis in this study.

To characterize the organic nucleation and condensation as well as investigate the controlling environmental factors for their occurrence, a series of sensitivity simulations were performed as listed in Table 4.3. A baseline simulation using the default WRF-Chem (BASE) was carried out, where the binary nucleation-generated aerosols were put into the 3rd bin to not only make sure the practical application of this nucleation parameterization (Wexler et al., 1994) but also keep agreeable aerosol size range with the observation (i.e., starting from 20 nm). Simulation using the improved version of WRF-Chem, CTRL, was conducted, where the new particles can be formed by organic nucleation aside from the default H_2SO_4 binary nucleation as in BASE and meantime the organic condensation process was also taken into consideration. In order to examine the effect of atmospheric vertical temperature variation on

the organic nucleation and condensation growth, sensitivity simulations were performed using the modified WRF-Chem model, but without temperature influence on the nucleation rate and the yield of the LVOC, namely BNUnoT and OCDnoT, respectively. For distinguishing the influence from the organic nucleation and the condensation of organics, an additional sensitivity simulation was made where only the condensation of organics was included in the BASE case, which was termed OCD.

Table 4.3. Description of numerical experiment design.

Experiment identification	Aerosol size range	Inorganic nucleation	Biogenic HOMs-induced nucleation (BNU)	Temperature effect on BNU	LVOCs organic condensation	Temperature effect on LVOC yield
BASE	0.01–10 μm	Wexler et al. (1994)	No	No	No	No
CTRL	0.0006–10 μm	Wexler et al. (1994)	Yes	Yes	Yes	Yes
BNU	0.0006–10 μm	Wexler et al. (1994)	Yes	Yes	No	No
OCD	0.0006–10 μm	Wexler et al. (1994)	No	No	Yes	Yes
BNUnoT	0.0006–10 μm	Wexler et al. (1994)	Yes	No	Yes	Yes
OCDnoT	0.0006–10 μm	Wexler et al. (1994)	Yes	Yes	Yes	No

Aircraft measurements of aerosol profiles during the ACIRIDICON-CHUVA campaign conducted over the Amazon during September–October in 2014 (Wendisch et al., 2016) were used to evaluate the model results. The ceiling altitude of the flights reached up to 15 km, close to the tropopause (18 km; Wendisch et al., 2016), providing an observational constraint for the UT aerosol study (Andreae et al., 2018; Schulz et al., 2018). The model reasonably reproduced the meteorological condition (Fig. 4.2), the trace gases–O_3 and NO vertical distribution, and the black carbon concentration (Fig. 4.3), showing its ability to capture the meteorological processes, basic atmospheric chemical processes, and primary

aerosol emission and transport processes. In addition, the simulated concentration of the biogenic organic vapors–α-pinene, β-pinene and isopere (Fig. 4.4) is in comparable magnitude with previous observation (Kuhn et al., 2010), indicating the reasonable model simulation of the biogenic emission.

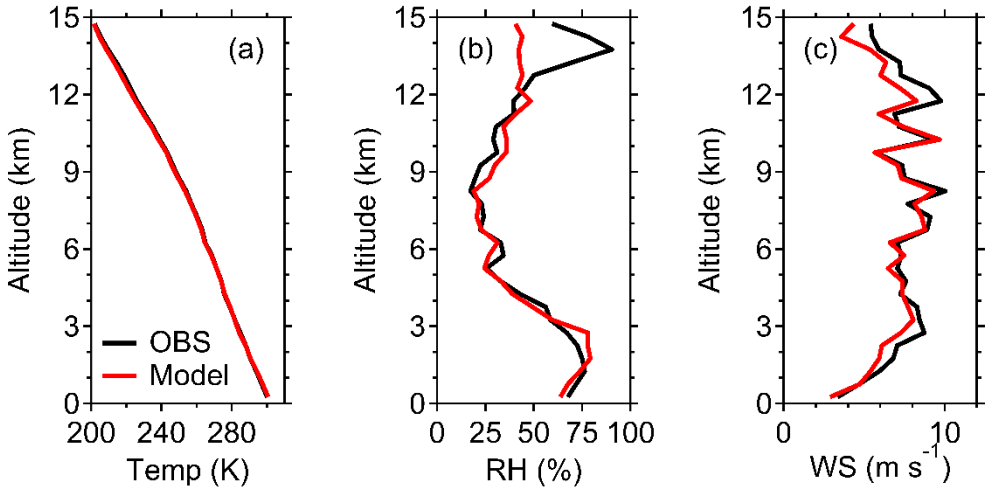

Figure 4.2. Comparison of (a) air temperature, (b) relative humidity and (c) wind speed averaged from all flight measurements and WRF-Chem simulation.

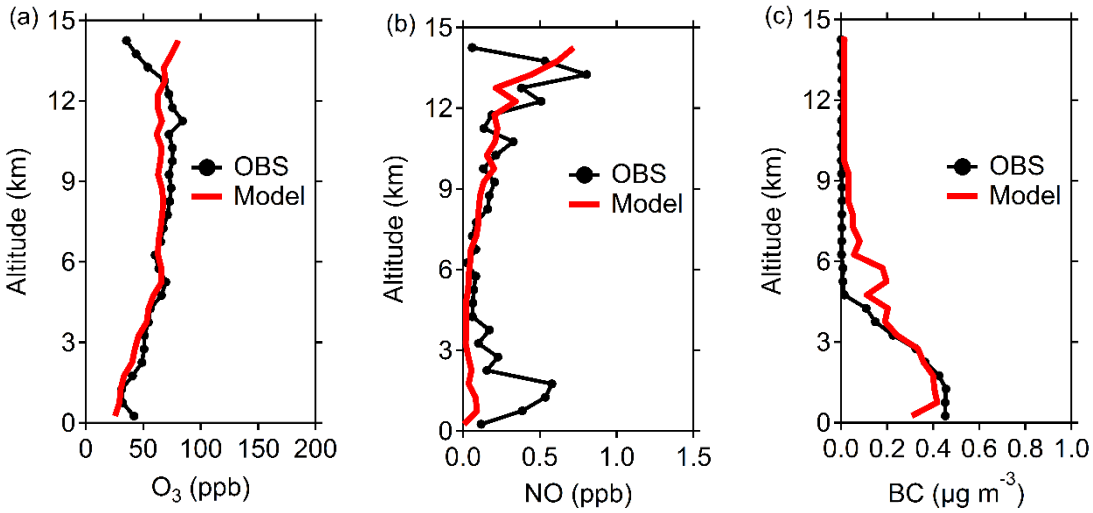

Figure 4.3. Comparison of (a) O_3, (b) NO, and (c) black carbon mass from flight measurements and model simulation.

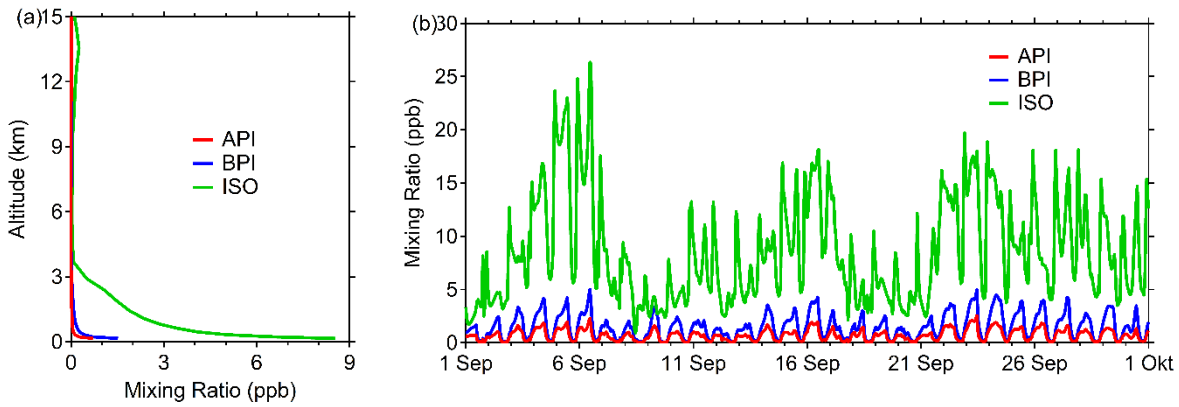

Figure 4.4. Simulated (a) vertical profiles and (b) time series of α-pinene, β-pinene, and isoprene mixing ratio at the location of ATTO.

4.3 Results

4.3.1 CCN simulation in the upper troposphere

Figure 4.5a–b show the profiles of number concentration of particles with a diameter above 20 nm and CCN at 0.52% supersaturation (hereinafter termed as CCN 0.52%) observed by aircraft during the ACRIDICON-CHUVA campaign (Fig. 4.1) and simulated by WRF-Chem scenarios (Table 4.3) from the 15-km-resolution domain. The CCN 0.52% is approximately 90 nm in diameter that is calculated according to the algorithm of Su et al. (2010). Compared with the observation, the BASE case simulation generally reproduces the vertical distribution of CN and CCN 0.52% for the vertical range from the ground to 8 km which covers the lower (PBL; 0–4 km) and middle troposphere (MT; 5–8 km). Especially, the observed high values of CN and CCN concentration in the PBL and their minimum concentration at the height of 4–5 km (Andreae et al., 2018) are well captured by the BASE case, which demonstrates a reasonable model performance in simulating aerosol processes dominating in the PBL and MT such as emission, transport, and scavenging. However, in the upper troposphere (UT; 9–15 km), although the BASE case still simulates comparable CN concentration compared with the observation, it underestimates the observed CCN number by

up to 500 cm^{-3} (Table 4.4). The large discrepancy in CCN is indicative of a lack of particle growth for the smaller particles in the upper troposphere in the default WRF-Chem simulation.

When adding the particle growth from the condensation of LVOC into the model (i.e., the OCD case), the simulated CCN number in the UT rises noticeably, with an increase of about 90% relative to the BASE case (Table 4.4). However, the larger particles from the condensation growth serve as scavengers and efficiently deplete the nanoscale particles, causing a dramatic CN concentration decrease. The lower bias of CN number under sufficient condensation growth may result from some missing mechanisms of new particle production in the UT (Gordon et al., 2016; Metzger et al., 2010). By further taking into account the organic nucleation (i.e., the CTRL case where both the organic nucleation and the condensation of LVOC are considered), the simulated CN number is considerably enhanced relative to the OCD case, resulting in substantially better agreements with the observation, while the CCN number in the model shows a much weaker increase (90 cm^{-3}, about 14%; Table 4.4) and still remains close to the observation. Under sufficient condensation growth, the organic nucleation leads to an increase of over 2100 cm^{-3} (over 50%; Table 4.4) in CN concentration through replenishing new nanoparticles relative to the case without its contribution (OCD; Fig. 4.5c). In summary, the HOMs-induced nucleation and the condensation of LVOC, which are both driven by the biogenic precursors both, play important roles in maintaining the particle population and size spectrum in the UT. The HOMs-induced nucleation significantly affects the CN number but has a weak influence on the CCN 0.52% concentration, while the condensation of LVOC causes a significant increase in the CCN concentration. This is expected as the CN number dominated by relatively small particles (Andreae et al., 2018) is sensitive to the newly formed particles which can be produced by the nucleation process. However, the CCN 0.52% mainly encompasses particles in the accumulation and coarse modes and requires considerable particle growth. The particle growth solely from H_2SO_4 is marginal as most H_2SO_4 is consumed during

the upward transport and only little reaches the UT. Therefore, the condensation of LVOC in the UT is a crucial mechanism for particle growth and therefore remarkably affects the CCN population in the UT.

Table 4.4. Averaged values of modeled and observed aerosol particle number concentration.

	CN (cm^{-3})			CCN 0.52% (cm^{-3})		
	PBL*	MT*	UT*	PBL*	MT*	UT*
Observation	1650±1030	2130±3070	7700±7970	880±630	410±150	840±440
BASE	2229	2486	6134	804	492	348
CTRL	2698	2223	6011	1103	581	750
OCD	2392	2138	3896	1092	569	660
OCDnoT	2653	2353	6163	1369	544	464

*PBL, MT, and UT are defined as the altitude range of 0–4 km, 5–8 km, 9–15 km, respectively.

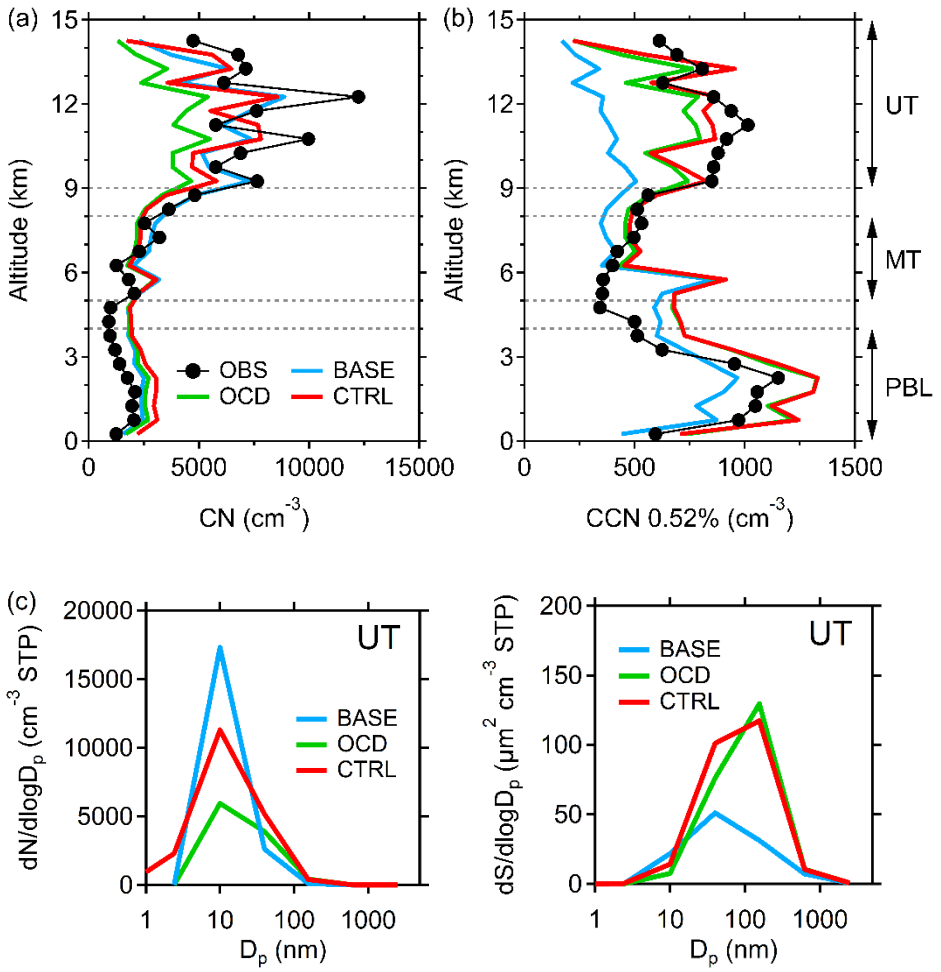

Figure 4.5. Comparison of observed and simulated particle number of (a) CN with diameter above 20 nm and (b) CCN at 0.52% supersaturation. Also shown are (c) size distributions of particle number and surface area in the UT along the flight track from model simulations.

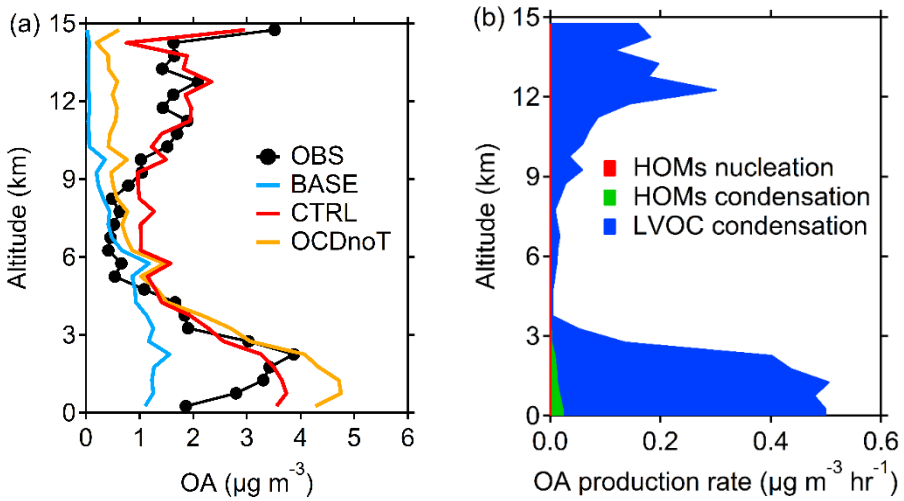

Figure 4.6. (a) Comparison of observed and simulated total OA mass; (b) contributions to OA mass from secondary organic aerosol formation processes.

Fig. 4.6a compares the simulated organic aerosol (OA) mass from the BASE, CTRL, and OCDnoT cases with the AMS-measured data. The BASE case using the MOSAIC aerosol module and FINN biomass burning emission inventory shows a reasonable performance of OA representation in the PBL, which is also confirmed by previous evaluations for this region (Archer-Nicholls et al., 2015), but significantly underestimates the OA in the UT. The underestimation of OA mass in the UT in the BASE case is greatly improved by the CTRL case due to the aerosol processes in the UT driven by the biogenic precursors, rendering a fair agreement between the CTRL case and the observation. Fig. 4.6b demonstrates explicitly the contribution to the OA mass from individual processes associated with the biogenic precursors. The condensation of LVOC can nearly account for the mass gain in the OA from BASE to CTRL while the other two processes, HOMs nucleation and HOMs condensation, contribute little. To further examine the uncertainty of the LVOC condensation in terms of the LVOC yield, sensitivity simulations regarding the temperature dependence of the LVOC yield were performed. The OCDnoT case adopted a bulk assumption of a yield of 13% from monoterpene oxidation and 3% from isoprene oxidation (OCDnoT) suggested by Scott et al. (2014); while in the CTRL case, temperature dependence of SOA yield based on an α-pinene oxidation

experiment (Saathoff et al., 2009) was applied to the LVOC yield. The OCDnoT case produces a larger amount of boundary layer OA than the CTRL case, causing a higher bias in the model compared with the observation. A significant difference between the environment where these yields were originally based (Kroll et al., 2005) and the region investigated here may be the reason for the poor performance of using these bulk yields directly, as the temperature previously used is relatively lower than the tropical forest boundary layer condition. This could also explain the underestimation of OA mass in the OCDnoT for the UT where the temperature is far below the freezing point (Fig. 4.6a).

4.3.2 Characteristics of organic nucleation and condensation

To examine the spatial characteristics of the HOMs-induced nucleation, spatial distributions of the monthly mean α-pinene, HOMs and its condensation on existing aerosols, nucleation rate (J_{org}), and convection-related variables (surface equivalent potential temperature, the upward flux of α-pinene to the UT, and precipitation) in the PBL, MT, and UT are shown in Fig. 4.7. α-pinene is used here as the surrogate of the biogenic organic precursors (α-pinene and β-pinene) given its dominant role in HOMs production (Zhu & Penner, 2019). Generally, HOMs concentration and the J_{org} are closely linked (Figs. 4.7a and 4.7b), which is legitimate as J_{org} is parameterized by HOMs. High concentrations of organic precursors and/or small CS (low concentration of existing particles) would lead to a high concentration of HOMs and thus high J_{org}. The fact that no evident spatial correlation is found between the oxidants (O_3 and OH) and HOMs (Fig. 4.8) indicates that for the overall tropospheric condition in the simulated area, O_3 and OH is high enough for their oxidation reactions with α-pinene and β-pinene to occur, and do not constitute limiting factors for the HOMs production in this region.

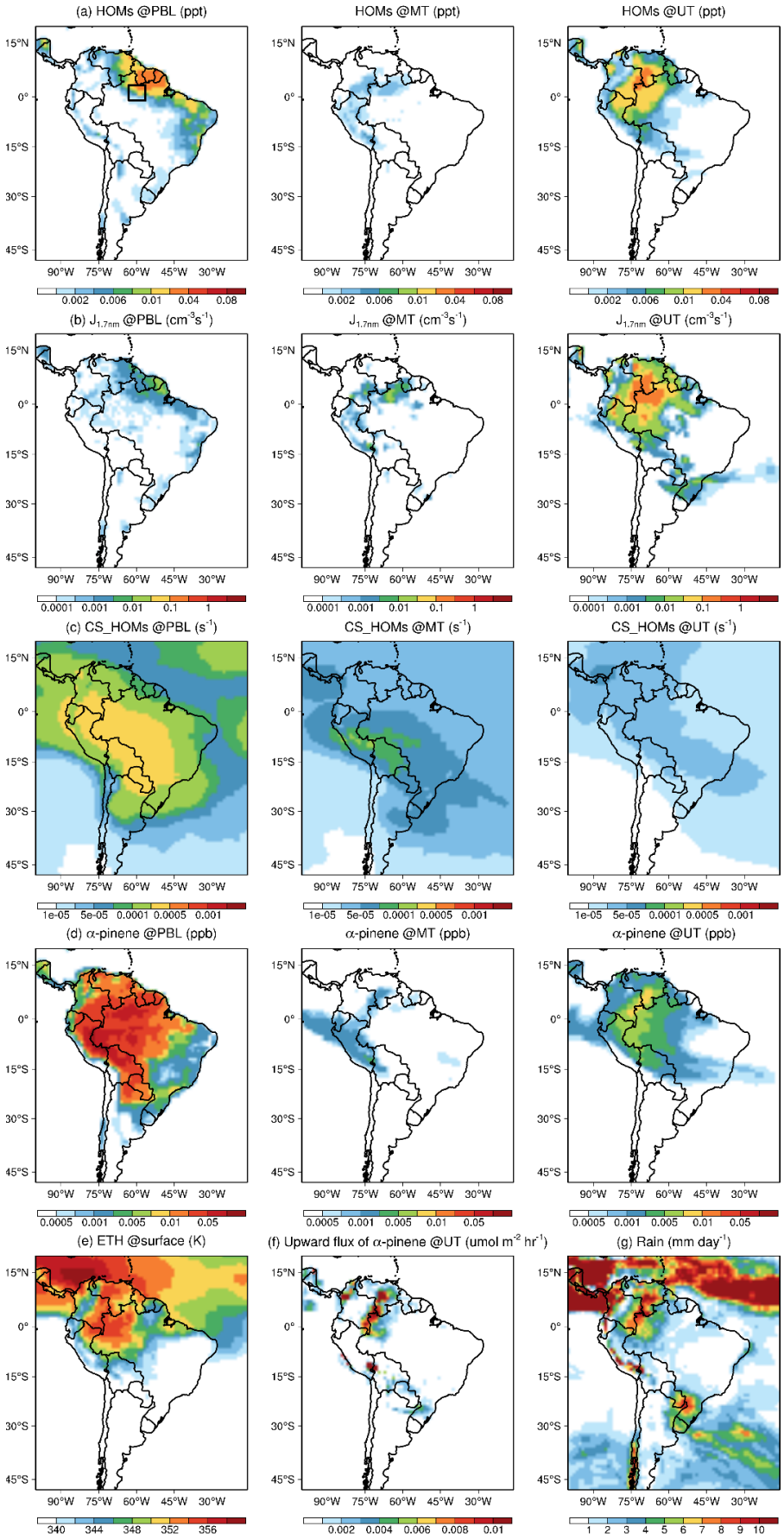

Figure 4.7. Spatial distribution of (a) HOMs, (b) organic nucleation rate, (c) condensation sink of HOMs, and (d) α-pinene mixing ratio at the PBL (left panel), MT (middle panel), and UT (right panel). Also shown are (e) equivalent potential temperature (ETH) at surface, (f) upward α-pinene flux at the UT, and (g) precipitaiton rate averaged over 01 Sep–01 Oct 2014. The black rectangle in (a) is the same as the marked area in Fig. 4.1, denoting the region of the Central Amazon.

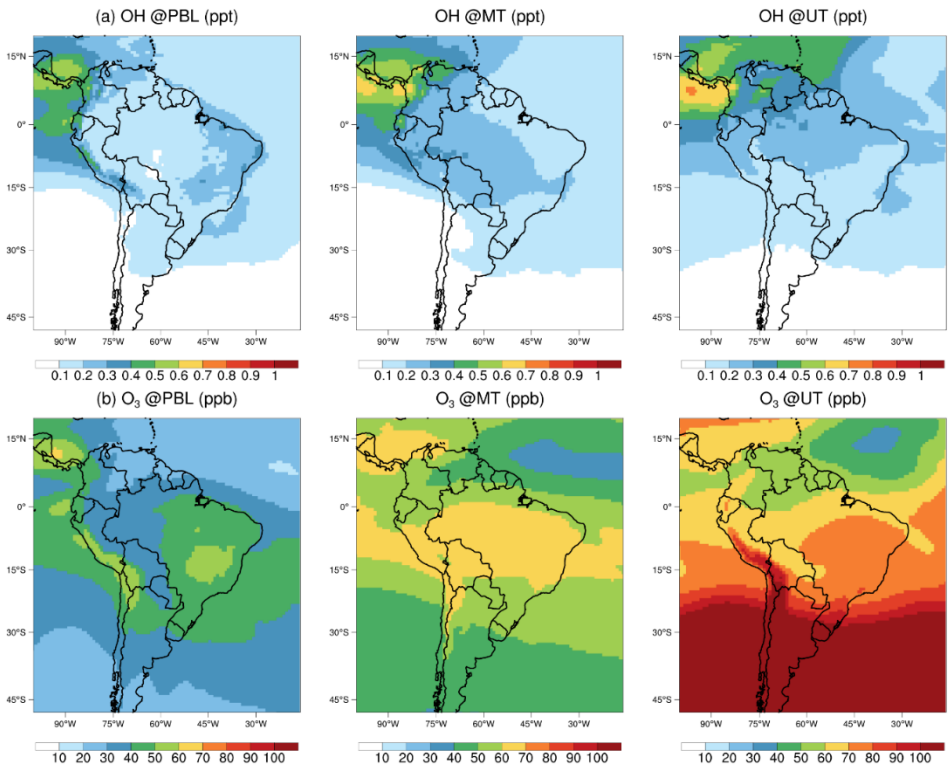

Figure 4.8. Horizontal distribution of (a) OH and (b) O_3 averaged over 01 Sep–01 Oct 2014 from the CTRL case.

High HOMs concentration and J_{org} are found in the PBL and UT with a minimum in the MT. The high HOMs concentrations in the PBL can be explained by the abundant organic precursors sourced from the canopy vegetation (Fig. 4.7d). With surface sources, the organic precursors are most abundant in the PBL (Fig. 4.7d). The high value of HOMs in the PBL is located at the northern and eastern parts of the Amazon Basin with a relatively low condensation sink of HOMs (Fig. 4.7c). This spatial association indicates the CS as an important limiting factor for the content of HOMs in the PBL. Although the α-pinene is a factor of magnitude larger in the PBL than in the UT, the HOMs at the two levels are comparable, which is associated with the low CS (sink of HOMs) in the UT (Fig. 4.7c). Then, the temperature dependence of J_{org} acts to foster a higher J_{org} in the UT compared with the PBL due to a cold upper tropospheric condition. As shown in Fig. 4.9, when the temperature effect

is not considered, the J_{org} in the UT is much lower than that with the temperature effect. The systematic low concentration of biogenic organic precursors and considerable condensation sink of HOMs could be the reason for the insignificant HOMs and J_{org} in the MT (Fig. 4.7d and 4.7c). Generally, the J_{org} is dominated by the ion-induced nucleation at all levels but is contributed considerably by the neutral nucleation mechanism at the PBL (Fig. 4.10), which is consistent with the previous simulations (e.g., Zhu & Penner, 2019).

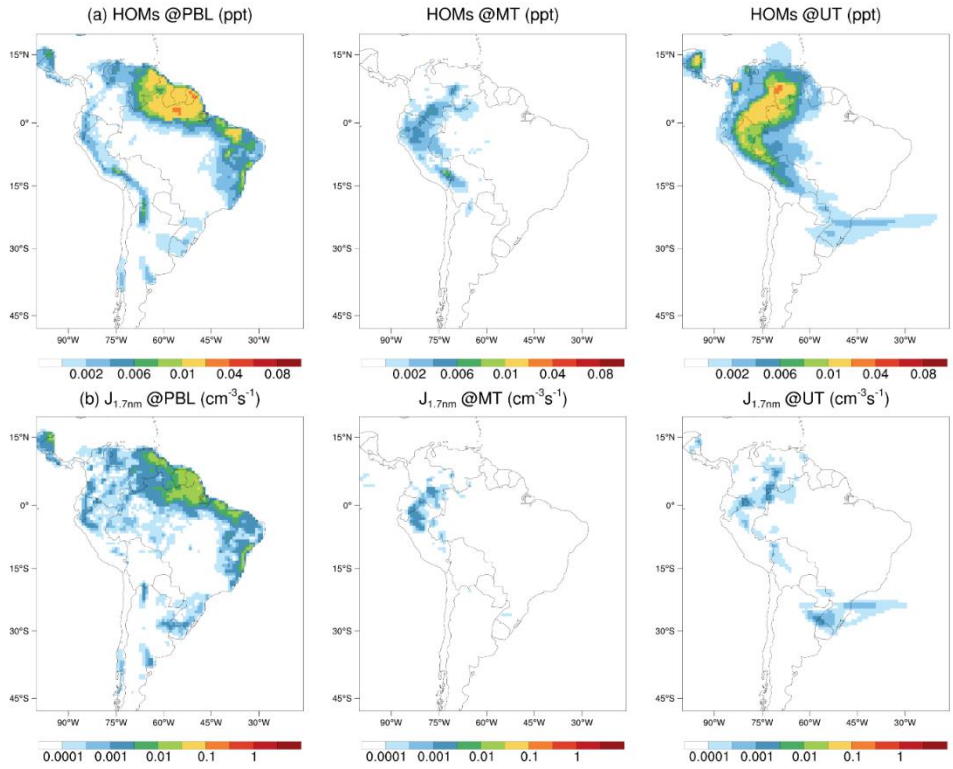

Figure 4.9. Horizontal distribution of (a) HOMs and (b) organic nucleation rate averaged over 01 Sep–01 Oct 2014 from the BNUnoT case.

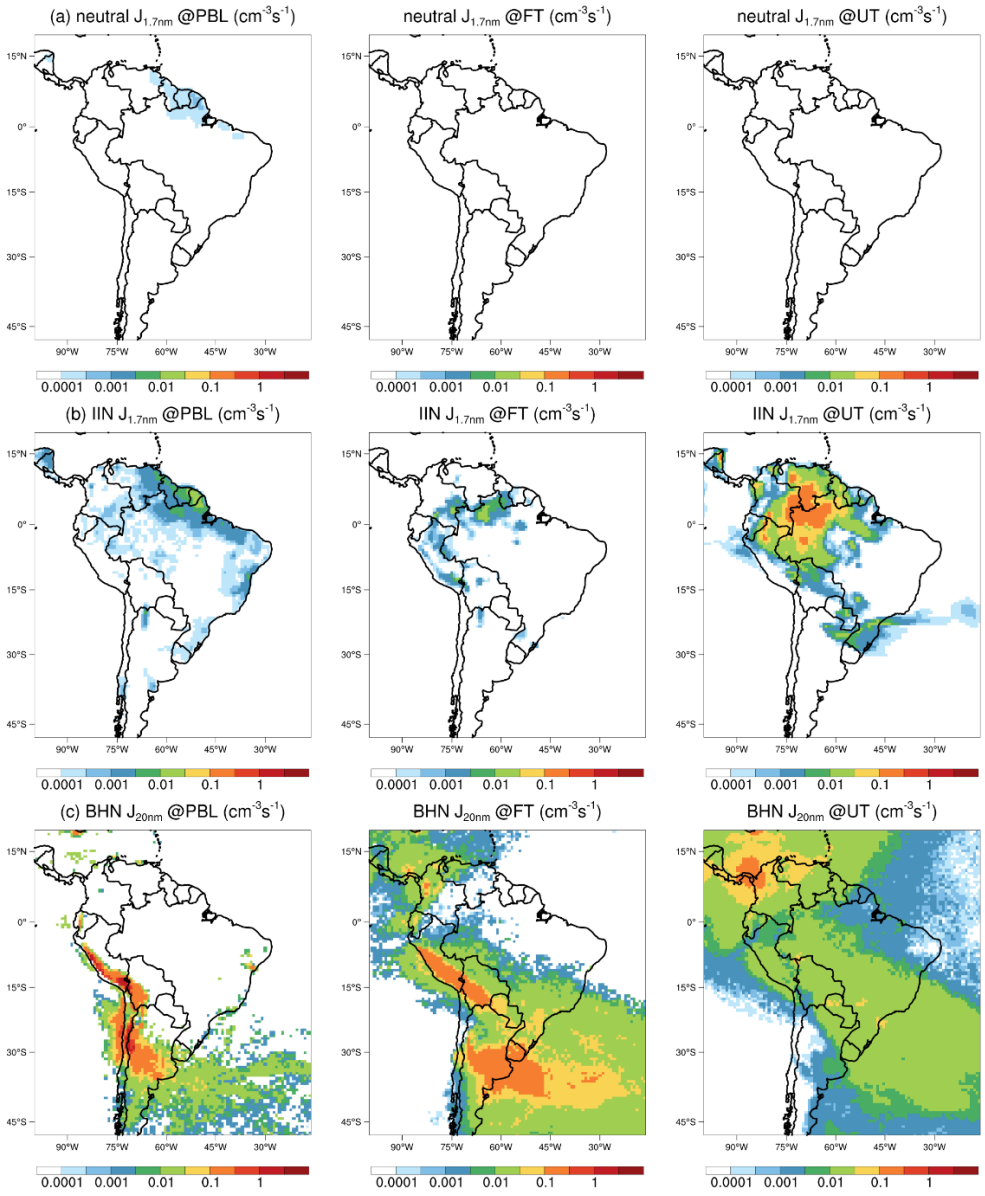

Figure 4.10. Horizontal distribution of the (a) neutral organic nucleation rate, (b) ion-induced organic nucleation rate, and (c) H_2SO_4-H_2O binary homogeneous nucleation rate at the PBL (left panel), MT (middle panel), and UT (right panel) averaged over 01 Sep–01 Oct 2014.

Figure 4.11a shows the daily variation of HOMs, J_{org}, newly formed particle ($N_{1.2}$, particles with a diameter of 1.2 nm) concentration, as well as meteorological factors averaged over the Central Amazon (marked with a black box in Fig. 4.1). The J_{org} in the PBL shows a moderate daily variation with values larger than $1e^{-3}$ cm^{-3} s^{-1} on most days. On the contrary, the J_{org} in the UT bears prominent daily variation with sporadically occurring high J_{org} episodes ($1e^{-2}$ to $1e^{-1}$ cm^{-3} s^{-1}). These episodes show a correlation with the occurrence of precipitating deep convection, which will be discussed in the next section. The overall magnitude of J_{org} throughout the troposphere is lower than the annual average of about 0.1 cm^{-3} s^{-1} in the Amazon region simulated previously (Zhu & Penner, 2019), possibly due to the omission of the ion sink in Zhu & Penner (2019). Note that the higher J_{org} in the PBL does not lead to a substantial amount of newly formed particles as a result of the high CS in the PBL. By contrast, the high J_{org} episodes in the UT result in a great abundance of fine particles. Following this, the days with the J_{org} in the UT larger than $1e^{-2}$ cm^{-3} s^{-1} were defined as UT biogenic NPF episodes (Fig. 4.11a) to further analyze the UT NPF characteristics and related ambient properties. During the UT NPF days, The HOMs and J_{org} demonstrate a clear diurnal cycle, with significant and negligible values in the daytime and nighttime, respectively. Although O_3 and OH both serve as oxidants in the HOMs production, the reaction rates of OH are several orders faster than O_3 (R4.1–4.2)and therefore may act as the dominant oxidant. Thus, the photolysis origin of OH (Fig. 4.11b–4.11c) can explain the daytime burst of the HOMs and J_{org}.

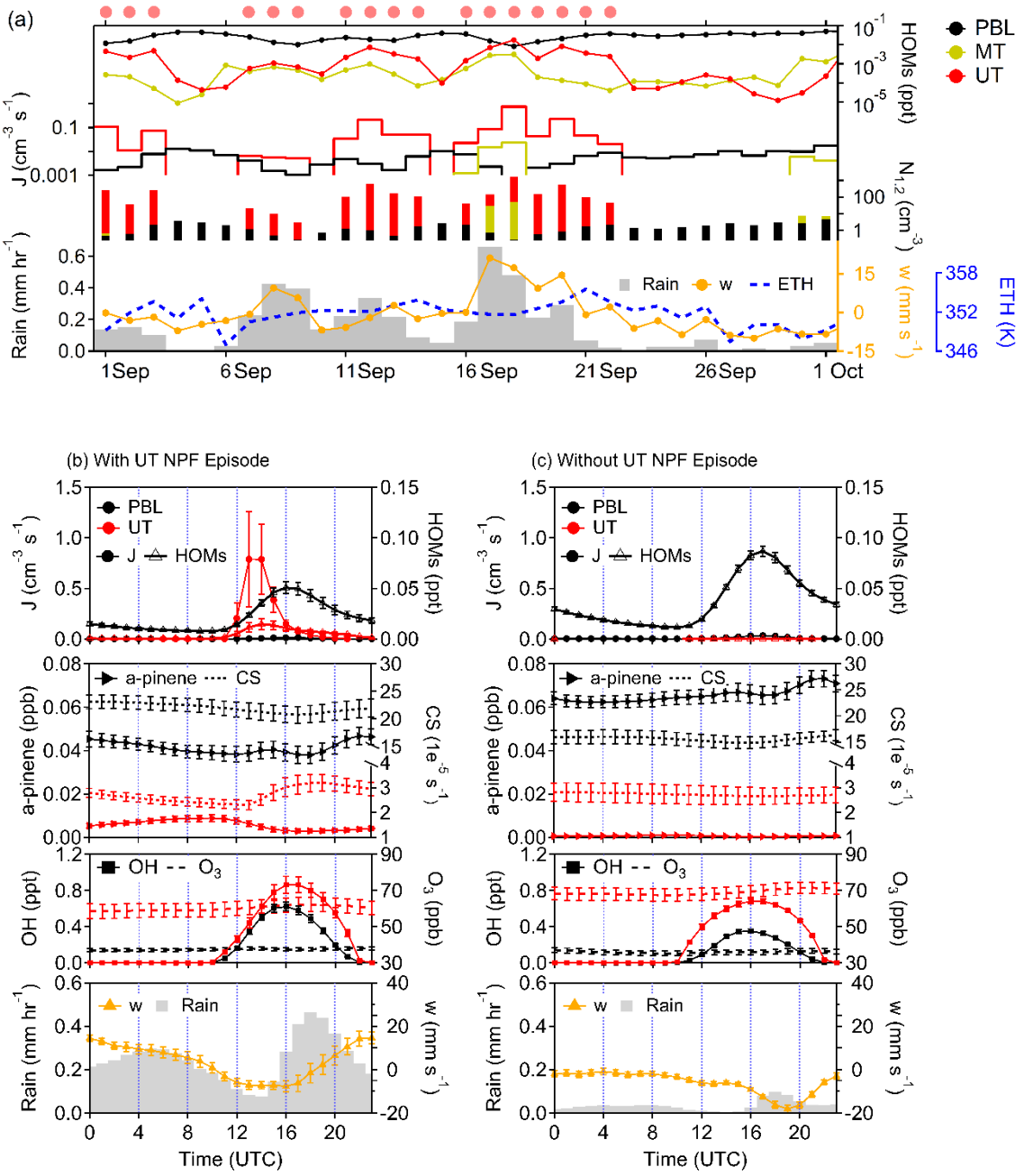

Figure 4.11. Temporal vairaiton of the rate and precursors of biogenic nucleation as well as meteorological variables. (a) Daily variation of regional averaged HOMs, nucleation rate, number concentration of particles with diameter of 1.2 nm ($N_{1.2}$), verticel wind at 8 km (w), precipitation, and surface air equvalent potential temperature. The dots above the figure mark the UT NPF episodes. The diurnal patterns of HOMs, nucleation rate, mixing ratio of α-pinene, O_3 and OH, and condensation sink of HOMs average in the PBL (black) and UT (red) and verticel wind at 8 km and precipitation for (b) the UT NPF episodes and (c) non-NPF episodes. The analyzed region is indicated in Fig. 4.1. The bars denote the standard error.

4.3.3 Factors influencing organic-driven CCN in upper troposphere

A positive correlation between the organic nucleation in the UT and precipitation can be found spatially (Fig. 4.7) and temporally (Fig. 4.11a). As revealed in the spatial distribution, the region where HOMs densely concentrate is analogous to the location of large upward α-pinene flux to the UT, which is different from the α-pinene distribution in the lower atmosphere but identical to the precipitation pattern. It indicates that the deep convective activities which are often accompanied by precipitation play a crucial role in the availability of the precursors in the UT. Stronger convection manifested as large precipitation rate and vertical wind can be found in the upper tropospheric NPF days relative to the non-NPF days (Fig. 4.11b–4.11c). Specifically, the nighttime convective activity as an extension of the former day convection contributes to the upper tropospheric accumulation of the biogenic precursors. Consequently, in the UT, the HOMs and J_{org} are almost zero in the non-NPF days limited by the biogenic precursors, while a high concentration of α-pinene at the NPF days gives rise to the formation of HOMs and subsequent organic nucleation. The reduced CS in the UT due to the nighttime precipitation scavenging in the deep convective condition may also act as a contributing factor to the following daytime increase of HOMs.

On the other hand, the reinforced upward shortwave radiation (Fig. 4.12) associated with increased cloud amount in the convection weather favors the photolysis production of OH in the UT and subsequent oxidation of biogenic compounds. The daily variation of HOMs in the PBL tends to be oppositely correlated with the surface precipitation (Fig. 4.11a), revealing a different role of atmospheric convection in the HOMs formation in this layer. The higher cloud amount in the precipitation days reduces the incident solar radiation reaching the ground surface (Fig. 4.12), hinders the emission of monoterpenes (Fig. 4.12), and thus decreases the HOMs concentration near the surface.

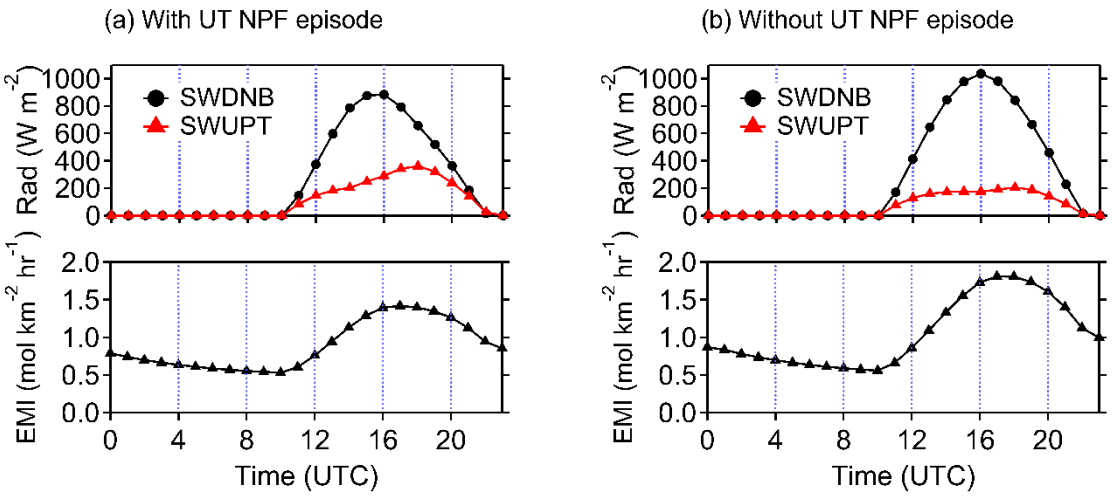

Figure 4.12. The diurnal variation of radiation flux and α-pinene emission rate for the average of (a) NPF episodes and (b) non-NPF episodes.

4.4 Conclusions

In this work, new organic nucleation and condensation schemes were developed and integrated into the WRF-Chem model to investigate the aerosol production in the UT by BVOCs emitted from the forest canopy. Several sensitivity studies were conducted over a precursor-rich region, the Amazon Basin, in September–October 2014 to illustrate the relative contribution of the organic nucleation and condensation to the aerosol population in the UT, to characterize their temporal and spatial distribution, and to identify the driving mechanisms for their occurrence.

The model evaluation against the aircraft measurements during the ACRIDICON-CHUVA campaign shows that the addition of the pure organic nucleation and organic growth substantially improves the model prediction of the CCN at 0.52% supersaturation and the OA mass in the UT. The organic condensation of LVOC contributes significantly to the CCN concentration in the UT by serving as an efficient mechanism for particle growth. The organic condensation improves the CCN concentration simulated by the default WRF-Chem by about 90% in the upper troposphere. The organic nucleation constitutes an important new particle

production pathway for the upper troposphere in the Amazon. Under sufficient particle growth, the nanoparticles produced from H_2SO_4-H_2O binary nucleation is largely scavenged, and the organic nucleation can efficiently replenish the nanoparticles, causing an increase of over 50% and 14% in the CN and CCN number concentration in the UT.

For the HOMs-induced organic nucleation, the simulation results show that HOMs can substantially form by the oxidation of biogenic organic vapors in the PBL and UT, while its formation at the MT is insignificant in the Amazon Basin. The concentration of HOMs in PBL and MT is limited by its condensation sink onto preexisting particles. Deep convection determines the HOMs formation in the UT through transporting biogenic organic vapors to the UT. Throughout the troposphere, the formation of HOMs is evident during the daytime associated with the hydroxyl radical produced from photolysis reactions. The pure organic nucleation is dominated by the ion-induced pathway rather than the neutral nucleation, and its spatial and temporal characteristics are similar to that of the HOMs, but the temperature effect on the nucleation rate favors the nucleation in the UT while curbs its intensity in the PBL.

For the condensation of LVOC oxidized from biogenic organic vapors, the simulation results show that it takes an overwhelming role over the HOMs nucleation and HOMs condensation in SOA mass production. The SOA mass from the LVOC condensation is dependent on the yield of the LVOC. A bulk assumption of the LVOC yield used previously in boreal forest fails to reproduce the observed OA mass due to a different condition in the tropics. Sensitivity studies show that a temperature dependant correction of LVOC yield based on laboratory experiments is necessary for correcting the overestimation and underestimation of OA mass by the bulk LVOC yield assumption in the PBL and UT, respectively.

Chapter 5 Summary and Outlook

5.1 Summary

Clouds and precipitation play crucial roles in the radiation balance and hydrological cycle of the Earth. They have been found to be susceptiable to atmospheric aerosols via aerosol-radiation interactions and aerosol-cloud interactions (IPCC, 2013), yet the impacts of ARI and ACI on clouds and precipitation are far from being well understood and accurately assessed. The challenge for this unsolved issue comes both from the complex nature of the aerosol-cloud systems where there are manifold feedbacks between multiple dynamical, thermodynamical, and microphysical processes on a wide range of temporal and special scales, and from the inadequate representation of these processes in numerical models which are used to make assessments of the aerosol impacts. This dissertation focuses on the regional aerosol effects on the clouds and precipitation in the Amazon during the dry season, which not only deepens our understanding of the aerosol-cloud-precipitation interaction mechanisms but also contributes to more accurate assessments of aerosol effects in the Amazon. The studies in this dissertation used the online coupled meteorology-chemistry model, WRF-Chem, which has comprehensive treatments of the atmospheric processes including the aerosol and cloud processes in a high sophistication level and allows the interactions between aerosol, radiation, clouds, and precipitation. This dissertation made a comprehensive assessment and a detailed mechanism analysis of the BB aerosol impacts on the clouds and precipitation in the studied region and period based on the WRF-Chem model shared in the community. Then, the development of the organic nucleation and condensation modules of WRF-Chem significantly improves the simulation of the upper tropospheric SOA-dominated CCN and the ACI representation in this model.

The study in Chapter 2 assessed the BB aerosol impacts on cloud and precipitation by examining the different cloud and precipitation changes at different aerosol emission scenarios

and illustrating the detailed mechanisms through which the ARI and ACI effects on cloud and precipitation are realized. The ARI and ACI of BB aerosols have opposite effects on the cloud LWP. The surface cooling, atmospheric stabilization, and the atmospheric heating from the ARI of BB aerosols inhibit convection development and reduce the cloud LWP. Oppositely, the cloud LWP is enhanced by ACI since the smaller cloud droplet radius caused by ACI inhibits the transformation from cloud droplets to raindrops. The relative importance of the two competing effects is influenced by the aerosol loading, with the ACI dominating when the aerosol concentration is low while the ARI taking the main role at high aerosol loading. The response of the cloud IWP to BB aerosols is a factor of magnitude smaller than that of the cloud LWP. The cloud IWP is consistently enhanced by BB aerosols at all emission scenarios as the ARI takes a dominant role and acts to enhance the upward flux of water vapor. The shortwave RF of BB aerosols is the outcome of a competition between positive RF by the ARI effect and negative RF by the ACI effect, which is driven largely by the cloud response. Such cloud adjustments to the BB aerosols exert a significant influence on the aerosol radiative forcing of BB aerosols in the Amazon. Although BB aerosols themselves cause negative indirect shortwave RF, the cloud reduction by the ARI of BB aerosols results in so strong positive shortwave RF that the ultimate effective shortwave RF of BB aerosols turns to be positive. Contrarily, the ACI of BB aerosols causes a negative indirect shortwave RF because of the increased cloud albedo resulted from more but smaller cloud droplets. Similar to the cloud LWP, the relative role of the ACI and ARI effects in the total BB shortwave RF depends on aerosol loading, with the former dominating at low aerosol emission scenario, while the latter at high emission scenario. The positive longwave RF by BB aerosols is driven by the ARI effect, which corresponds to the enhanced ice cloud by the ARI. Ultimately, the all-band RF of BB aerosols in the Amazon is −0.2 and 1.5 W m^{-2} for the EMIS1 and EMIS6 scenarios, respectively.

The precipitation occurrence is reduced by both the ACI and ARI of BB aerosols. The domain-averaged precipitation rate is diminished substantially by ACI consistently over all the emission scenarios due to strong suppression of warm rain formation, although a weak invigoration of precipitation by the ACI occurs in the lower-emission scenarios possibly due to the mechanism proposed by Rosenfeld et al. (2008). The precipitation response to the ARI effect is nonlinear: enhanced precipitation is found in low-emission scenarios while suppression of precipitation is caused at high BB aerosol emission rates. Ultimately, the overall effects of BB aerosols result in a reduction in the precipitation rate and the reduction intensifies with increasing aerosol concentration, suggesting a positive feedback between the aerosol concentration and the precipitation. The monthly mean precipitation rate is estimated to be reduced by BB aerosols by −5% and −23% in the EMIS1 and EMIS6 scenarios, respectively, which reflects the strong susceptibility of precipitation to BB aerosol concentration. The precipitation susceptibility to aerosol concentration is more pronounced in the intensive precipitation conditions than in the light precipitation regime.

The distinctive responses of cloud and precipitation at different BB aerosol concentrations prove that the whole picture of the aerosol effects in the Amazon where undergoes interannual emission variations needs a comprehensive assessment based on multi-year aerosol emissions. The relative roles of the ACI and ARI effects vary with increasing aerosol loading, manifesting as a saturating trend of the ACI while a continuingly increasing strength of the ARI at high aerosol loadings. This phenomenon highlights the climatic significance of the ARI effect in highly polluted conditions and may provide implications for similar pollution cases such as heavily polluted urban areas and the crop waste burning season in agricultural areas.

The ARI of BB aerosols plays an important role in the precipitation formation in the Amazon, yet the previous investigations of the ARI effect are limited on the macrophysical

scale, leaving the detailed cloud microphysical processes behind the ARI-induced precipitation change unknown. The study in Chapter 3 digs into the cloud microphysical processes underlying the precipitation response to the ARI of BB aerosols using a process analysis method. It proposes the microphysical mechanism for the ARI impact on the precipitation from the locally generated convective clouds on a diurnal cycle. The simulation results show that the overall ARI effect on daily precipitation from the locally generated clouds involves two competing pathways. First, the ARI suppresses convection through surface fluxes reduction and atmospheric heating; the resultant diminished liquid cloud inhibits the raindrop accreting cloud water (RAW) and therefore suppresses precipitation. At this stage, the warm-rain process RAW dominantly causes the precipitation reduction while the cold-rain processes also contribute to but take a less important role. Second, the convection is invigorated by the ARI as the release of previously reserved energy and moisture promotes cloud water and ice formation. Then, the warm rain production from the raindrops accreting cloud droplets (RAW) is enhanced due to increased cloud water. Meantime, more snow generated from the ice crystals through the Bergeron process SFI was converted into more graupel, which together with enhanced graupel accretion of cloud water (GAW) act to boost the graupel concentration and the subsequent graupel melting (GMT), giving rise to more rainwater mass. The two microphysical pathways dominate at an earlier and later stage of a diurnal cloud evolution in the Amazon region, respectively, yielding an attenuated diurnal amplitude of precipitation under the ARI effect of BB aerosols. The two alternating microphysical mechanisms for the precipitation response to ARI persistently occur for different conditions in the Amazon, yet the relative importance of the two phases tends to be sensitive to the aerosol loading and the background conditions. The precipitation invigoration appears more pronounced in less polluted deep convection while the precipitation suppression appears overwhelmingly in shallow or highly polluted conditions. The significant improvement in the diurnal precipitation

simulation by taking the ARI effect into account suggests the inclusion of ARI in models as a potential way to improve the model simulation performance of diurnal convective variation.

The insufficient parameterization of secondary organic aerosol processes in the WRF-Chem aerosol and gas chemistry module, MOSAIC coupled with CRIMECH, limits the model ability to reproduce the upper tropospheric SOA-dominated CCN concentration, affecting the model assessment of the aerosol-cloud interactions. To improve the WRF-Chem simulation of the CCN in the upper troposphere, in Chapter 4, new organic nucleation and condensation schemes were developed and implemented into the WRF-Chem MOSAIC+ CRIMECH aerosol and gas chemistry modules so that the CCN source from the organic nucleation and condensation by BVOCs emitted from the forest canopy could be taken into consideration.

We incorporate the gas chemistry scheme CRIMECH with HOMs- and LVOC-generating reactions, extend the MOSAIC aerosol module to cover aerosol sizes from 0.6 nm to 10 μm in diameter, and integrate the laboratory result-based pure organic nucleation (HOMs-induced nucleation) and LVOC condensation parameterization into the MOSAIC aerosol scheme. Simulations were conducted over the biogenic precursor-rich region, the Amazon Basin, in September−October 2014, and were evaluated in terms of the aerosol number and mass concentrations and their vertical distribution against aircraft measurements during the ACRIDICON-CHUVA. The newly developed modules significantly correct the underestimation of the CCN at 0.52% supersaturation and OA mass in the UT in the default WRF-Chem while maintains the comparable CN concentration to the observation simulated in the default WRF-Chem.

Sensitivity studies isolate and estimate the contribution to the CN number and CCN number concentration from the individual aerosol processes. The organic condensation of LVOC significantly enhances the CCN concentration in the UT by acting as an efficient mechanism for particle growth while it meantime depletes the smaller particles and therefore

has a negative effect on the CN number in the UT. Quantitatively, the LVOC condensation improves the upper tropospheric CCN 0.52% in the default WRF-Chem by about 90%. The HOMs-induced organic nucleation provides additional new particles aside from the existing H_2SO_4-H2O binary nucleation mechanism. The organic nucleation causes an improvement of over 50% and 14% in the CN and CCN number concentration in the UT under the condition of sufficient particle growth.

Characteristics and the driving environmental factors for the HOMs-induced organic nucleation and the condensation of LVOC can be derived from the model simulation. HOMs formed by the oxidation of biogenic organic vapors condensate substantially in the PBL and UT but marginally in the MT in the Amazon Basin. Deep convection controls the occurrence of HOMs production in the UT by controlling the transport of biogenic organic vapors to the UT. The large condensation sink onto preexisting particles limits the HOMs concentration in the PBL and MT while favors the HOMs maintenance in the UT. Generally, the HOMs formation is evident in the daytime corresponding to the hydroxyl radical produced from photolysis reactions. The pure organic nucleation is roughly similar to that of the HOMs in terms of the spatial and temporal characteristics but the significant temperature effect on the nucleation rate ultimately results in distinctively high and low organic nucleation in the UT and in the PBL, respectively. Within the pure organic nucleation mechanisms, the ion-induced pathway takes the dominant role over the neutral nucleation. For the SOA mass production, the condensation of LVOC contributes overwhelmingly over the HOMs nucleation and HOMs condensation. The SOA mass from the LVOC condensation is sensitive to the yield of the LVOC. A temperature dependant correction on the bulk assumption of LVOC yield based on laboratory experiments is suggested to better reproduce the observed OA mass.

5.2 Outlook

To better understand and more accurately assess the aerosol impacts on the cloud and precipitation in the Amazon during the dry season, future work including more numerical simulation experiments and further model improvements is still needed.

Firstly, as stated in Chapter 4, SOA in the upper troposphere is substantial in the Amazon and results in a significant abundance of CCN in the middle to high atmosphere. Such a high concentration of CCN can invoke the secondary in-cloud activation processes, which could be an important CCN activation pathway aside from the already existing cloud-base CCN activation mechanism. Therefore, including the treatment of the secondary in-cloud activation into the numerical model improves the model parameterization of the ACI. The study presented in Chapter 4 integrated newly developed organic nucleation and condensation modules into the WRF-Chem model and significantly improved the simulated CCN concentration in the free troposphere. This ensures correct CCN concentration input for the secondary in-cloud activation process. To fully enable the secondary in-cloud activation of CCN in the WRF-Chem model, an additional in-cloud activation scheme needs to be developed and implemented into the WRF-Chem model.

Including the heterogeneous nucleation of IN would be another worthwhile work for improving the ACI in the WRF-Chem model. By now, the laboratory experiments have not provided adequate results for the exact species, the mechanism, and the parameterization of IN. With the development of the laboratory studies on this topic, it is desirable to include the process of heterogeneous nucleation into WRF-Chem to complete the model treatments of the ACI and to better quantify the aerosol effects on climate.

Furthermore, the response of clouds and precipitation to aerosols was found to be influenced by the meteorological background conditions (Fan et al., 2009). The assessment of BB aerosol impact on cloud and precipitation in Chapter 2 is based on September 2014. Future

model investigations based on varying background meteorology are desired to characterize the influence of meteorological variations on the cloud and precipitation response. Besides, studies based on longer periods are needed to provide long-term climatic assessments.

Another potential future work is to extend the regional model simulation to larger-scale simulation. The study in Chapter 2 and 3 focus on the regional effects of BB aerosols on the clouds and precipitation in the Amazon Basin, which is mainly limited by the computation resources required for cloud-resolving resolution. Modeling studies found that the large-scale dynamical perturbation by aerosols could affect the large-scale circulation and therefore redistribute precipitation spatially (Lee et al., 2014). With adequate computing capability in the future, it would be worthwhile to investigate the aerosol impacts on the cloud and precipitation on a larger-scale with cloud-resolving resolution.

List of Figures

List of Tables

References

Abdul-Razzak, H., & Ghan, S. J. (2002). A parameterization of aerosol activation - 3. Sectional representation. Journal of Geophysical Research-Atmospheres, 107(D3), 6, Article 4026. https://doi.org/10.1029/2001jd000483

Ackerman, A. S., Toon, O. B., Stevens, D. E., Heymsfield, A. J., Ramanathan, V., & Welton, E. J. (2000). Reduction of tropical cloudiness by soot. Science, 288(5468), 1042-1047. https://doi.org/10.1126/science.288.5468.1042

Albrecht, B. A. (1989). AEROSOLS, CLOUD MICROPHYSICS, AND FRACTIONAL CLOUDINESS. Science, 245(4923), 1227-1230. https://doi.org/10.1126/science.245.4923.1227

Andreae, M. O. (2009). Correlation between cloud condensation nuclei concentration and aerosol optical thickness in remote and polluted regions. Atmospheric Chemistry and Physics, 9(2), 543-556. https://doi.org/10.5194/acp-9-543-2009

Andreae, M. O. (2019). Emission of trace gases and aerosols from biomass burning - an updated assessment. Atmospheric Chemistry and Physics, 19(13), 8523-8546. https://doi.org/10.5194/acp-19-8523-2019

Andreae, M. O., Acevedo, O. C., Araujo, A., Artaxo, P., Barbosa, C. G. G., Barbosa, H. M. J., Brito, J., Carbone, S., Chi, X., Cintra, B. B. L., da Silva, N. F., Dias, N. L., Dias, C. Q., Ditas, F., Ditz, R., Godoi, A. F. L., Godoi, R. H. M., Heimann, M., Hoffmann, T., Kesselmeier, J., Konemann, T., Kruger, M. L., Lavric, J. V., Manzi, A. O., Lopes, A. P., Martins, D. L., Mikhailov, E. F., Moran-Zuloaga, D., Nelson, B. W., Nolscher, A. C., Nogueira, D. S., Piedade, M. T. F., Pöhlker, C., Pöschl, U., Quesada, C. A., Rizzo, L. V., Ro, C. U., Ruckteschler, N., Sa, L. D. A., Sa, M. D., Sales, C. B., dos Santos, R. M. N., Saturno, J., Schongart, J., Sorgel, M., de Souza, C. M., de Souza, R. A. F., Su, H., Targhetta, N., Tota, J., Trebs, I., Trumbore, S., van Eijck, A., Walter, D., Wang, Z., Weber, B., Williams, J., Winderlich, J., Wittmann, F., Wolff, S., & Yanez-Serrano, A. M. (2015). The Amazon Tall Tower Observatory (ATTO): overview of pilot measurements on ecosystem ecology, meteorology, trace gases, and aerosols. Atmospheric Chemistry and Physics, 15(18), 10723-10776. https://doi.org/10.5194/acp-15-10723-2015

Andreae, M. O., Afchine, A., Albrecht, R., Holanda, B. A., Artaxo, P., Barbosa, H. M. J., Borrmann, S., Cecchini, M. A., Costa, A., Dollner, M., Futterer, D., Jarvinen, E., Jurkat, T., Klimach, T., Konemann, T., Knote, C., Kramer, M., Krisna, T., Machado,

L. A. T., Mertes, S., Minikin, A., Pöhlker, C., Pöhlker, M. L., Pöschl, U., Rosenfeld, D., Sauer, D., Schlager, H., Schnaiter, M., Schneider, J., Schulz, C., Spanu, A., Sperling, V. B., Voigt, C., Walser, A., Wang, J., Weinzierl, B., Wendisch, M., & Ziereis, H. (2018). Aerosol characteristics and particle production in the upper troposphere over the Amazon Basin. Atmospheric Chemistry and Physics, 18(2), 921-961. https://doi.org/10.5194/acp-18-921-2018

Andreae, M. O., Andreae, T. W., Annegarn, H., Beer, J., Cachier, H., le Canut, P., Elbert, W., Maenhaut, W., Salma, I., Wienhold, F. G., & Zenker, T. (1998). Airborne studies of aerosol emissions from savanna fires in southern Africa: 2. Aerosol chemical composition. Journal of Geophysical Research-Atmospheres, 103(D24), 32119-32128. https://doi.org/10.1029/98jd02280

Andreae, M. O., Artaxo, P., Brandao, C., Carswell, F. E., Ciccioli, P., da Costa, A. L., Culf, A. D., Esteves, J. L., Gash, J. H. C., Grace, J., Kabat, P., Lelieveld, J., Malhi, Y., Manzi, A. O., Meixner, F. X., Nobre, A. D., Nobre, C., Ruivo, M., Silva-Dias, M. A., Stefani, P., Valentini, R., von Jouanne, J., & Waterloo, M. J. (2002). Biogeochemical cycling of carbon, water, energy, trace gases, and aerosols in Amazonia: The LBA-EUSTACH experiments. Journal of Geophysical Research-Atmospheres, 107(D20), 25, Article 8066. https://doi.org/10.1029/2001jd000524

Andreae, M. O., & Merlet, P. (2001). Emission of trace gases and aerosols from biomass burning. Global Biogeochemical Cycles, 15(4), 955-966. https://doi.org/10.1029/2000gb001382

Andreae, M. O., & Rosenfeld, D. (2008). Aerosol-cloud-precipitation interactions. Part 1. The nature and sources of cloud-active aerosols. Earth-Science Reviews, 89(1-2), 13-41. https://doi.org/10.1016/j.earscirev.2008.03.001

Andreae, M. O., Rosenfeld, D., Artaxo, P., Costa, A. A., Frank, G. P., Longo, K. M., & Silva-Dias, M. A. F. (2004). Smoking rain clouds over the Amazon. Science, 303(5662), 1337-1342. https://doi.org/10.1126/science.1092779

Archer-Nicholls, S., Lowe, D., Darbyshire, E., Morgan, W. T., Bela, M. M., Pereira, G., Trembath, J., Kaiser, J. W., Longo, K. M., Freitas, S. R., Coe, H., & McFiggans, G. (2015). Characterising Brazilian biomass burning emissions using WRF-Chem with MOSAIC sectional aerosol. Geoscientific Model Development, 8(3), 549-577. https://doi.org/10.5194/gmd-8-549-2015

Archer-Nicholls, S., Lowe, D., Schultz, D. M., & McFiggans, G. (2016). Aerosol-radiation-cloud interactions in a regional coupled model: the effects of convective

parameterisation and resolution. Atmospheric Chemistry and Physics, 16(9), 5573-5594. https://doi.org/10.5194/acp-16-5573-2016

Archer-Nicholls, S., Lowe, D., Utembe, S., Allan, J., Zaveri, R. A., Fast, J. D., Hodnebrog, O., van der Gon, H. D., & McFiggans, G. (2014). Gaseous chemistry and aerosol mechanism developments for version 3.5.1 of the online regional model, WRF-Chem. Geoscientific Model Development, 7(6), 2557-2579. https://doi.org/10.5194/gmd-7-2557-2014

Artaxo, P., Rizzo, L. V., Brito, J. F., Barbosa, H. M. J., Arana, A., Sena, E. T., Cirino, G. G., Bastos, W., Martin, S. T., & Andreae, M. O. (2013). Atmospheric aerosols in Amazonia and land use change: from natural biogenic to biomass burning conditions. Faraday Discussions, 165, 203-235. https://doi.org/10.1039/c3fd00052d

Barnard, J. C., Fast, J. D., Paredes-Miranda, G., Arnott, W. P., & Laskin, A. (2010). Technical Note: Evaluation of the WRF-Chem "Aerosol Chemical to Aerosol Optical Properties" Module using data from the MILAGRO campaign. Atmospheric Chemistry and Physics, 10(15), 7325-7340. https://doi.org/10.5194/acp-10-7325-2010

Baro, R., Jimenez-Guerrero, P., Stengel, M., Brunner, D., Curci, G., Forkel, R., Nea, L., Palacios-Pena, L., Savage, N., Schaap, M., Tuccella, P., van der Gon, H. D., & Galmarini, S. (2018). Evaluating cloud properties in an ensemble of regional online coupled models against satellite observations. Atmospheric Chemistry and Physics, 18(20), 15183-15199. https://doi.org/10.5194/acp-18-15183-2018

Benmoshe, N., & Khain, A. P. (2014). The effects of turbulence on the microphysics of mixed-phase deep convective clouds investigated with a 2-D cloud model with spectral bin microphysics. Journal of Geophysical Research-Atmospheres, 119(1), 207-221. https://doi.org/10.1002/2013jd020118

Bevan, S. L., North, P. R. J., Grey, W. M. F., Los, S. O., & Plummer, S. E. (2009). Impact of atmospheric aerosol from biomass burning on Amazon dry-season drought. Journal of Geophysical Research-Atmospheres, 114, 11, Article D09204. https://doi.org/10.1029/2008jd011112

Birch, C. E., Webster, S., Peatman, S. C., Parker, D. J., Matthews, A. J., Li, Y., & Hassim, M. E. E. (2016). Scale Interactions between the MJO and the Western Maritime Continent. Journal of Climate, 29(7), 2471-2492. https://doi.org/10.1175/jcli-d-15-0557.1

Bond, T. C., & Bergstrom, R. W. (2006). Light absorption by carbonaceous particles: An investigative review. Aerosol Science and Technology, 40(1), 27-67. https://doi.org/10.1080/02786820500421521

Braga, R. C., Rosenfeld, D., Weigel, R., Jurkat, T., Andreae, M. O., Wendisch, M., Pöschl, U., Voigt, C., Mahnke, C., Borrmann, S., Albrecht, R. I., Molleker, S., Vila, D. A., Machado, L. A. T., & Grulich, L. (2017). Further evidence for CCN aerosol concentrations determining the height of warm rain and ice initiation in convective clouds over the Amazon basin. Atmospheric Chemistry and Physics, 17(23), 14433-14456. https://doi.org/10.5194/acp-17-14433-2017

Breon, F. M., Tanre, D., & Generoso, S. (2002). Aerosol effect on cloud droplet size monitored from satellite. Science, 295(5556), 834-838. https://doi.org/10.1126/science.1066434

Burkholder, J. B., Baynard, T., Ravishankara, A. R., & Lovejoy, E. R. (2007). Particle nucleation following the O-3 and OH initiated oxidation of alpha-pinene and beta-pinene between 278 and 320 K. Journal of Geophysical Research-Atmospheres, 112(D10), 16, Article D10216. https://doi.org/10.1029/2006jd007783

Calvo, A. I., Alves, C., Castro, A., Pont, V., Vicente, A. M., & Fraile, R. (2013). Research on aerosol sources and chemical composition: Past, current and emerging issues. Atmospheric Research, 120, 1-28. https://doi.org/10.1016/j.atmosres.2012.09.021

Carslaw, K. S., Lee, L. A., Reddington, C. L., Pringle, K. J., Rap, A., Forster, P. M., Mann, G. W., Spracklen, D. V., Woodhouse, M. T., Regayre, L. A., & Pierce, J. R. (2013). Large contribution of natural aerosols to uncertainty in indirect forcing. Nature, 503(7474), 67. https://doi.org/10.1038/nature12674

Chameides, W. L., Luo, C., Saylor, R., Streets, D., Huang, Y., Bergin, M., & Giorgi, F. (2002). Correlation between model-calculated anthropogenic aerosols and satellite-derived cloud optical depths: Indication of indirect effect?. Journal of Geophysical Research-Atmospheres, 107(D10), 21, Article 4085. https://doi.org/10.1029/2000jd000208

Chang, D., Cheng, Y., Reutter, P., Trentmann, J., Burrows, S. M., Spichtinger, P., Nordmann, S., Andreae, M. O., Pöschl, U., & Su, H. (2015). Comprehensive mapping and characteristic regimes of aerosol effects on the formation and evolution of pyro-convective clouds. Atmospheric Chemistry and Physics, 15(18), 10325-10348. https://doi.org/10.5194/acp-15-10325-2015

Chapman, E. G., Gustafson, W. I., Easter, R. C., Barnard, J. C., Ghan, S. J., Pekour, M. S., & Fast, J. D. (2009). Coupling aerosol-cloud-radiative processes in the WRF-Chem model: Investigating the radiative impact of elevated point sources. Atmospheric Chemistry and Physics, 9(3), 945-964. https://doi.org/10.5194/acp-9-945-2009

Cheng, C. T., Wang, W. C., & Chen, J. P. (2010). Simulation of the effects of increasing cloud condensation nuclei on mixed-phase clouds and precipitation of a front system [Article; Proceedings Paper]. Atmospheric Research, 96(2-3), 461-476. https://doi.org/10.1016/j.atmosres.2010.02.005

Chow, J. C., Watson, J. G., Edgerton, S. A., & Vega, E. (2002). Chemical composition of PM2.5 and PM10 in Mexico City during winter 1997. Science of the Total Environment, 287(3), 177-201, Article Pii s0048-9697(01)00982-2. https://doi.org/10.1016/s0048-9697(01)00982-2

Cifelli, R., Carey, L., Petersen, W. A., & Rutledge, S. A. (2004). An ensemble study of wet season convection in southwest Amazonia: Kinematics and implications for diabatic heating. Journal of Climate, 17(24), 4692-4707. https://doi.org/10.1175/jcli-3236.1

Cox, P. M., Harris, P. P., Huntingford, C., Betts, R. A., Collins, M., Jones, C. D., Jupp, T. E., Marengo, J. A., & Nobre, C. A. (2008). Increasing risk of Amazonian drought due to decreasing aerosol pollution. Nature, 453(7192), 212-U217. https://doi.org/10.1038/nature06960

Cui, Y. Y., Hodzic, A., Smith, J. N., Ortega, J., Brioude, J., Matsui, H., Levin, E. J. T., Turnipseed, A., Winkler, P., & de Foy, B. (2014). Modeling ultrafine particle growth at a pine forest site influenced by anthropogenic pollution during BEACHON-RoMBAS 2011. Atmospheric Chemistry and Physics, 14(20), 11011-11029. https://doi.org/10.5194/acp-14-11011-2014

D'Andrea, S. D., Hakkinen, S. A. K., Westervelt, D. M., Kuang, C., Levin, E. J. T., Kanawade, V. P., Leaitch, W. R., Spracklen, D. V., Riipinen, I., & Pierce, J. R. (2013). Understanding global secondary organic aerosol amount and size-resolved condensational behavior. Atmospheric Chemistry and Physics, 13(22), 11519-11534. https://doi.org/10.5194/acp-13-11519-2013

Dai, A., Giorgi, F., & Trenberth, K. E. (1999). Observed and model-simulated diurnal cycles of precipitation over the contiguous United States. Journal of Geophysical Research-Atmospheres, 104(D6), 6377-6402. https://doi.org/10.1029/98jd02720

Dai, A., & Trenberth, K. E. (2002). Estimates of freshwater discharge from continents: Latitudinal and seasonal variations. Journal of Hydrometeorology, 3(6), 660-687. https://doi.org/10.1175/1525-7541(2002)003<0660:Eofdfc>2.0.Co;2

Deetz, K., Vogel, H., Knippertz, P., Adler, B., Taylor, J., Coe, H., Bower, K., Haslett, S., Flynn, M., Dorsey, J., Crawford, I., Kottmeier, C., & Vogel, B. (2018). Numerical simulations of aerosol radiative effects and their impact on clouds and atmospheric dynamics over southern West Africa. Atmospheric Chemistry and Physics, 18(13), 9767-9788. https://doi.org/10.5194/acp-18-9767-2018

Dipu, S., Prabha, T. V., Pandithurai, G., Dudhia, J., Pfister, G., Rajesh, K., & Goswami, B. N. (2013). Impact of elevated aerosol layer on the cloud macrophysical properties prior to monsoon onset. Atmospheric Environment, 70, 454-467. https://doi.org/10.1016/j.atmosenv.2012.12.036

Dunne, E. M., Gordon, H., Kurten, A., Almeida, J., Duplissy, J., Williamson, C., Ortega, I. K., Pringle, K. J., Adamov, A., Baltensperger, U., Barmet, P., Benduhn, F., Bianchi, F., Breitenlechner, M., Clarke, A., Curtius, J., Dommen, J., Donahue, N. M., Ehrhart, S., Flagan, R. C., Franchin, A., Guida, R., Hakala, J., Hansel, A., Heinritzi, M., Jokinen, T., Kangasluoma, J., Kirkby, J., Kulmala, M., Kupc, A., Lawler, M. J., Lehtipalo, K., Makhmutov, V., Mann, G., Mathot, S., Merikanto, J., Miettinen, P., Nenes, A., Onnela, A., Rap, A., Reddington, C. L. S., Riccobono, F., Richards, N. A. D., Rissanen, M. P., Rondo, L., Sarnela, N., Schobesberger, S., Sengupta, K., Simon, M., Sipilaa, M., Smith, J. N., Stozkhov, Y., Tome, A., Trostl, J., Wagner, P. E., Wimmer, D., Winkler, P. M., Worsnop, D. R., & Carslaw, K. S. (2016). Global atmospheric particle formation from CERN CLOUD measurements. Science, 354(6316), 1119-1124. https://doi.org/10.1126/science.aaf2649

Easter, R. C., Ghan, S. J., Zhang, Y., Saylor, R. D., Chapman, E. G., Laulainen, N. S., Abdul-Razzak, H., Leung, L. R., Bian, X. D., & Zaveri, R. A. (2004). MIRAGE: Model description and evaluation of aerosols and trace gases. Journal of Geophysical Research-Atmospheres, 109(D20), 46, Article D20210. https://doi.org/10.1029/2004jd004571

Ehn, M., Thornton, J. A., Kleist, E., Sipila, M., Junninen, H., Pullinen, I., Springer, M., Rubach, F., Tillmann, R., Lee, B., Lopez-Hilfiker, F., Andres, S., Acir, I. H., Rissanen, M., Jokinen, T., Schobesberger, S., Kangasluoma, J., Kontkanen, J., Nieminen, T., Kurten, T., Nielsen, L. B., Jorgensen, S., Kjaergaard, H. G., Canagaratna, M., Dal Maso, M., Berndt, T., Petaja, T., Wahner, A., Kerminen, V. M.,

Kulmala, M., Worsnop, D. R., Wildt, J., & Mentel, T. F. (2014). A large source of low-volatility secondary organic aerosol. Nature, 506(7489), 476. https://doi.org/10.1038/nature13032

Ekman, A. M. L., Krejci, R., Engstrom, A., Strom, J., de Reus, M., Williams, J., & Andreae, M. O. (2008). Do organics contribute to small particle formation in the Amazonian upper troposphere?. Geophysical Research Letters, 35(17), 5, Article L17810. https://doi.org/10.1029/2008gl034970

Elbert, W., Taylor, P. E., Andreae, M. O., & Pöschl, U. (2007). Contribution of fungi to primary biogenic aerosols in the atmosphere: wet and dry discharged spores, carbohydrates, and inorganic ions. Atmospheric Chemistry and Physics, 7(17), 4569-4588. https://doi.org/10.5194/acp-7-4569-2007

Emmons, L. K., Walters, S., Hess, P. G., Lamarque, J. F., Pfister, G. G., Fillmore, D., Granier, C., Guenther, A., Kinnison, D., Laepple, T., Orlando, J., Tie, X., Tyndall, G., Wiedinmyer, C., Baughcum, S. L., & Kloster, S. (2010). Description and evaluation of the Model for Ozone and Related chemical Tracers, version 4 (MOZART-4). Geoscientific Model Development, 3(1), 43-67. https://doi.org/10.5194/gmd-3-43-2010

Fahey, K. M., & Pandis, S. N. (2001). Optimizing model performance: variable size resolution in cloud chemistry modeling. Atmospheric Environment, 35(26), 4471-4478. https://doi.org/10.1016/s1352-2310(01)00224-2

Fan, J. W., Rosenfeld, D., Yang, Y., Zhao, C., Leung, L. R., & Li, Z. Q. (2015). Substantial contribution of anthropogenic air pollution to catastrophic floods in Southwest China. Geophysical Research Letters, 42(14), 6066-6075. https://doi.org/10.1002/2015gl064479

Fan, J. W., Rosenfeld, D., Zhang, Y. W., Giangrande, S. E., Li, Z. Q., Machado, L. A. T., Martin, S. T., Yang, Y., Wang, J., Artaxo, P., Barbosa, H. M. J., Braga, R. C., Comstock, J. M., Feng, Z., Gao, W. H., Gomes, H. B., Mei, F., Pöhlker, C., Pöhlker, M. L., Pöschl, U., & de Souza, R. A. F. (2018). Substantial convection and precipitation enhancements by ultrafine aerosol particles. Science, 359(6374), 411. https://doi.org/10.1126/science.aan8461

Fan, J. W., Yuan, T. L., Comstock, J. M., Ghan, S., Khain, A., Leung, L. R., Li, Z. Q., Martins, V. J., & Ovchinnikov, M. (2009). Dominant role by vertical wind shear in regulating aerosol effects on deep convective clouds. Journal of Geophysical

Research-Atmospheres, 114, 9, Article D22206. https://doi.org/10.1029/2009jd012352

Fast, J. D., Gustafson, W. I., Easter, R. C., Zaveri, R. A., Barnard, J. C., Chapman, E. G., Grell, G. A., & Peckham, S. E. (2006). Evolution of ozone, particulates, and aerosol direct radiative forcing in the vicinity of Houston using a fully coupled meteorology-chemistry-aerosol model. Journal of Geophysical Research-Atmospheres, 111(D21), 29, Article D21305. https://doi.org/10.1029/2005jd006721

Feingold, G., Jiang, H. L., & Harrington, J. Y. (2005). On smoke suppression of clouds in Amazonia. Geophysical Research Letters, 32(2), 4, Article L02804. https://doi.org/10.1029/2004gl021369

Fosser, G., Khodayar, S., & Berg, P. (2015). Benefit of convection permitting climate model simulations in the representation of convective precipitation. Climate Dynamics, 44(1-2), 45-60. https://doi.org/10.1007/s00382-014-2242-1

Freitas, S. R., Longo, K. M., Chatfield, R., Latham, D., Dias, M., Andreae, M. O., Prins, E., Santos, J. C., Gielow, R., & Carvalho, J. A. (2007). Including the sub-grid scale plume rise of vegetation fires in low resolution atmospheric transport models. Atmospheric Chemistry and Physics, 7(13), 3385-3398. https://doi.org/10.5194/acp-7-3385-2007

Fu, S. Z., Deng, X., Li, Z., & Xue, H. W. (2017). Radiative effect of black carbon aerosol on a squall line case in North China. Atmospheric Research, 197, 407-414. https://doi.org/10.1016/j.atmosres.2017.07.026

Ge, C., Wang, J., & Reid, J. S. (2014). Mesoscale modeling of smoke transport over the Southeast Asian Maritime Continent: coupling of smoke direct radiative effect below and above the low-level clouds. Atmospheric Chemistry and Physics, 14(1), 159-174. https://doi.org/10.5194/acp-14-159-2014

Gettelman, A., Morrison, H., Terai, C. R., & Wood, R. (2013). Microphysical process rates and global aerosol-cloud interactions. Atmospheric Chemistry and Physics, 13(19), 9855-9867. https://doi.org/10.5194/acp-13-9855-2013

Ghan, S. J., Leung, L. R., Easter, R. C., & AbdulRazzak, K. (1997). Prediction of cloud droplet number in a general circulation model. Journal of Geophysical Research-Atmospheres, 102(D18), 21777-21794. https://doi.org/10.1029/97jd01810

Ghan, S. J., Liu, X., Easter, R. C., Zaveri, R., Rasch, P. J., Yoon, J. H., & Eaton, B. (2012). Toward a Minimal Representation of Aerosols in Climate Models: Comparative

Decomposition of Aerosol Direct, Semidirect, and Indirect Radiative Forcing. Journal of Climate, 25(19), 6461-6476. https://doi.org/10.1175/jcli-d-11-00650.1

Goncalves, W. A., Machado, L. A. T., & Kirstetter, P. E. (2015). Influence of biomass aerosol on precipitation over the Central Amazon: an observational study. Atmospheric Chemistry and Physics, 15(12), 6789-6800. https://doi.org/10.5194/acp-15-6789-2015

Gordon, H., Kirkby, J., Baltensperger, U., Bianchi, F., Breitenlechner, M., Curtius, J., Dias, A., Dommen, J., Donahue, N. M., Dunne, E. M., Duplissy, J., Ehrhart, S., Flagan, R. C., Frege, C., Fuchs, C., Hansel, A., Hoyle, C. R., Kulmala, M., Kurten, A., Lehtipalo, K., Makhmutov, V., Molteni, U., Rissanen, M. P., Stozkhov, Y., Trostl, J., Tsagkogeorgas, G., Wagner, R., Williamson, C., Wimmer, D., Winkler, P. M., Yan, C., & Carslaw, K. S. (2017). Causes and importance of new particle formation in the present-day and preindustrial atmospheres. Journal of Geophysical Research-Atmospheres, 122(16), 8739-8760. https://doi.org/10.1002/2017jd026844

Gordon, H., Sengupta, K., Rap, A., Duplissy, J., Frege, C., Williamson, C., Heinritzi, M., Simon, M., Yan, C., Almeida, J., Trostl, J., Nieminen, T., Ortega, I. K., Wagner, R., Dunne, E. M., Adamov, A., Amorim, A., Bernhammer, A. K., Bianchi, F., Breitenlechner, M., Brilke, S., Chen, X. M., Craven, J. S., Dias, A., Ehrhart, S., Fischer, L., Flagan, R. C., Franchin, A., Fuchs, C., Guida, R., Hakala, J., Hoyle, C. R., Jokinen, T., Junninen, H., Kangasluoma, J., Kim, J., Kirkby, J., Krapf, M., Kurten, A., Laaksonen, A., Lehtipalo, K., Makhmutov, V., Mathot, S., Molteni, U., Monks, S. A., Onnela, A., Perakyla, O., Piel, F., Petaja, T., Praplanh, A. P., Pringle, K. J., Richards, N. A. D., Rissanen, M. P., Rondo, L., Sarnela, N., Schobesberger, S., Scott, C. E., Seinfeldo, J. H., Sharma, S., Sipila, M., Steiner, G., Stozhkov, Y., Stratmann, F., Tome, A., Virtanen, A., Vogel, A. L., Wagner, A. C., Wagner, P. E., Weingartner, E., Wimmer, D., Winkler, P. M., Ye, P. L., Zhang, X., Hansel, A., Dommen, J., Donahue, N. M., Worsnop, D. R., Baltensperger, U., Kulmala, M., Curtius, J., & Carslaw, K. S. (2016). Reduced anthropogenic aerosol radiative forcing caused by biogenic new particle formation. Proceedings of the National Academy of Sciences of the United States of America, 113(43), 12053-12058. https://doi.org/10.1073/pnas.1602360113

Grant, L. D., & van den Heever, S. C. (2014). Aerosol-cloud-land surface interactions within tropical sea breeze convection. Journal of Geophysical Research-Atmospheres, 119(13), 22, Article 2014jd021912. https://doi.org/10.1002/2014jd021912

Greco, S., Swap, R., Garstang, M., Ulanski, S., Shipham, M., Harriss, R. C., Talbot, R., Andreae, M. O., & Artaxo, P. (1990). Rainfall and surface kinematic conditions over central Amazonia during ABLE-2B. Journal of Geophysical Research-Atmospheres, 95(D10), 17001-17014. https://doi.org/10.1029/JD095iD10p17001

Grell, G., Freitas, S. R., Stuefer, M., & Fast, J. (2011). Inclusion of biomass burning in WRF-Chem: impact of wildfires on weather forecasts. Atmospheric Chemistry and Physics, 11(11), 5289-5303. https://doi.org/10.5194/acp-11-5289-2011

Grell, G. A., & Devenyi, D. (2002). A generalized approach to parameterizing convection combining ensemble and data assimilation techniques. Geophysical Research Letters, 29(14), 4, Article 1693. https://doi.org/10.1029/2002gl015311

Grell, G. A., Peckham, S. E., Schmitz, R., McKeen, S. A., Frost, G., Skamarock, W. C., & Eder, B. (2005). Fully coupled "online" chemistry within the WRF model. Atmospheric Environment, 39(37), 6957-6975. https://doi.org/10.1016/j.atmosenv.2005.04.027

Guenther, A., Karl, T., Harley, P., Wiedinmyer, C., Palmer, P. I., & Geron, C. (2006). Estimates of global terrestrial isoprene emissions using MEGAN (Model of Emissions of Gases and Aerosols from Nature). Atmospheric Chemistry and Physics, 6, 3181-3210. https://doi.org/10.5194/acp-6-3181-2006

Guo, J. P., Deng, M. J., Fan, J. W., Li, Z. Q., Chen, Q., Zhai, P. M., Dai, Z. J., & Li, X. W. (2014). Precipitation and air pollution at mountain and plain stations in northern China: Insights gained from observations and modeling. Journal of Geophysical Research-Atmospheres, 119(8), 4793-4807. https://doi.org/10.1002/2013jd021161

Guyon, P., Frank, G. P., Welling, M., Chand, D., Artaxo, P., Rizzo, L., Nishioka, G., Kolle, O., Dias, M., Gatti, L. V., Cordova, A. M., & Andreae, M. O. (2005). Airborne measurements of trace gas and aerosol particle emissions from biomass burning in Amazonia. Atmospheric Chemistry and Physics, 5, 2989-3002. https://doi.org/10.5194/acp-5-2989-2005

Hansen, J., Sato, M., & Ruedy, R. (1997). Radiative forcing and climate response. Journal of Geophysical Research-Atmospheres, 102(D6), 6831-6864. https://doi.org/10.1029/96jd03436

Hartmann, D. L., Ockertbell, M. E., & Michelsen, M. L. (1992). The effect of cloud type on Earths energy balance-global analysis. Journal of Climate, 5(11), 1281-1304. https://doi.org/10.1175/1520-0442(1992)005<1281:Teocto>2.0.Co;2

Holanda, B. A., Pöhlker, M. L., Walter, D., Saturno, J., Sorgel, M., Ditas, J., Ditas, F., Schulz, C., Franco, M. A., Wang, Q. Q., Donth, T., Artaxo, P., Barbosa, H. M. J., Borrmann, S., Braga, R., Brito, J., Cheng, Y. F., Dollner, M., Kaiser, J. W., Klimach, T., Knote, C., Kruger, O. O., Futterer, D., Lavric, J. V., Ma, N., Machado, L. A. T., Ming, J., Morais, F. G., Paulsen, H., Sauer, D., Schlager, H., Schneider, J., Su, H., Weinzierl, B., Walser, A., Wendisch, M., Ziereis, H., Zoger, M., Pöschl, U., Andreae, M. O., & Pöhlker, C. (2020). Influx of African biomass burning aerosol during the Amazonian dry season through layered transatlantic transport of black carbon-rich smoke. Atmospheric Chemistry and Physics, 20(8), 4757-4785. https://doi.org/10.5194/acp-20-4757-2020

Holben, B. N., Tanre, D., Smirnov, A., Eck, T. F., Slutsker, I., Abuhassan, N., Newcomb, W. W., Schafer, J. S., Chatenet, B., Lavenu, F., Kaufman, Y. J., Castle, J. V., Setzer, A., Markham, B., Clark, D., Frouin, R., Halthore, R., Karneli, A., O'Neill, N. T., Pietras, C., Pinker, R. T., Voss, K., & Zibordi, G. (2001). An emerging ground-based aerosol climatology: Aerosol optical depth from AERONET. Journal of Geophysical Research-Atmospheres, 106(D11), 12067-12097. https://doi.org/10.1029/2001jd900014

Holton, J. (1992). An Introduction to Dynamic Meteorology. International Geophysics Series, Academic Press, New York.

Hoose, C., & Mohler, O. (2012). Heterogeneous ice nucleation on atmospheric aerosols: a review of results from laboratory experiments. Atmospheric Chemistry and Physics, 12(20), 9817-9854. https://doi.org/10.5194/acp-12-9817-2012

Horrak, U., Aalto, P. P., Salm, J., Komsaare, K., Tammet, H., Makela, J. M., Laakso, L., & Kulmala, M. (2008). Variation and balance of positive air ion concentrations in a boreal forest. Atmospheric Chemistry and Physics, 8(3), 655-675. https://doi.org/10.5194/acp-8-655-2008

Hsie, E. Y., Farley, R. D., & Orville, H. D. (1980). Numerical simulation of ice-phase convective cloud seeding. Journal of Applied Meteorology, 19(8), 950-977. https://doi.org/10.1175/1520-0450(1980)019<0950:Nsoipc>2.0.Co;2

Huang, C. C., Chen, S. H., Lin, Y. C., Earl, K., Matsui, T., Lee, H. H., Tsai, I. C., Chen, J. P., & Cheng, C. T. (2019). Impacts of Dust-Radiation versus Dust-Cloud Interactions on the Development of a Modeled Mesoscale Convective System over North Africa. Monthly Weather Review, 147(9), 3301-3326. https://doi.org/10.1175/mwr-d-18-0459.1

Huang, X., Ding, A. J., Liu, L. X., Liu, Q., Ding, K., Niu, X. R., Nie, W., Xu, Z., Chi, X. G., Wang, M. H., Sun, J. N., Guo, W. D., & Fu, C. B. (2016). Effects of aerosol-radiation interaction on precipitation during biomass-burning season in East China. Atmospheric Chemistry and Physics, 16(15), 10063-10082. https://doi.org/10.5194/acp-16-10063-2016

Huffman, G. J., Adler, R. F., Bolvin, D. T., Gu, G. J., Nelkin, E. J., Bowman, K. P., Hong, Y., Stocker, E. F., & Wolff, D. B. (2007). The TRMM multisatellite precipitation analysis (TMPA): Quasi-global, multiyear, combined-sensor precipitation estimates at fine scales. Journal of Hydrometeorology, 8(1), 38-55. https://doi.org/10.1175/jhm560.1

IPCC: Climate Change 2013. (2013). The Physical Science Basis. Contribution of Working Group I to the Fifth Assessment Report of the Intergovernmental Panel on Climate Change. Cambridge University Press, Cambridge, United Kingdom and New York, NY, USA. doi:10.1017/CBO9781107415324.

Jacobson, M. Z. (1997). Development and application of a new air pollution modeling system .2. Aerosol module structure and design. Atmospheric Environment, 31(2), 131-144. https://doi.org/10.1016/1352-2310(96)00202-6

Jacobson, M. Z., Turco, R. P., Jensen, E. J., & Toon, O. B. (1994). Modeling coagulation among particles of different composition and size. Atmospheric Environment, 28(7), 1327-1338. https://doi.org/10.1016/1352-2310(94)90280-1

Janssens-Maenhout, G., Crippa, M., Guizzardi, D., Dentener, F., Muntean, M., Pouliot, G., Keating, T., Zhang, Q., Kurokawa, J., Wankmuller, R., van der Gon, H. D., Kuenen, J. J. P., Klimont, Z., Frost, G., Darras, S., Koffi, B., & Li, M. (2015). HTAP_v2.2: a mosaic of regional and global emission grid maps for 2008 and 2010 to study hemispheric transport of air pollution. Atmospheric Chemistry and Physics, 15(19), 11411-11432. https://doi.org/10.5194/acp-15-11411-2015

Jenkin, M. E., Watson, L. A., Utembe, S. R., & Shallcross, D. E. (2008). A Common Representative Intermediates (CRI) mechanism for VOC degradation. Part 1: Gas phase mechanism development. Atmospheric Environment, 42(31), 7185-7195. https://doi.org/10.1016/j.atmosenv.2008.07.028

Jiang, B. L., Huang, B., Lin, W. S., & Xu, S. S. (2016). Investigation of the Effects of Anthropogenic Pollution on Typhoon Precipitation and Microphysical Processes Using WRF-Chem. Journal of the Atmospheric Sciences, 73(4), 1593-1610. https://doi.org/10.1175/jas-d-15-0202.1

Jiang, H. L., & Feingold, G. (2006). Effect of aerosol on warm convective clouds: Aerosol-cloud-surface flux feedbacks in a new coupled large eddy model. Journal of Geophysical Research-Atmospheres, 111(D1), 12, Article D01202. https://doi.org/10.1029/2005jd006138

Johnson, B. T., Shine, K. P., & Forster, P. M. (2004). The semi-direct aerosol effect: Impact of absorbing aerosols on marine stratocumulus. Quarterly Journal of the Royal Meteorological Society, 130(599), 1407-1422. https://doi.org/10.1256/qj.03.61

Jokinen, T., Berndt, T., Makkonen, R., Kerminen, V. M., Junninen, H., Paasonen, P., Stratmann, F., Herrmann, H., Guenther, A. B., Worsnop, D. R., Kulmala, M., Ehn, M., & Sipila, M. (2015). Production of extremely low volatile organic compounds from biogenic emissions: Measured yields and atmospheric implications. Proceedings of the National Academy of Sciences of the United States of America, 112(23), 7123-7128. https://doi.org/10.1073/pnas.1423977112

Kaufman, Y. J., & Fraser, R. S. (1997). The effect of smoke particles on clouds and climate forcing. Science, 277(5332), 1636-1639. https://doi.org/10.1126/science.277.5332.1636

Kaufman, Y. J., & Koren, I. (2006). Smoke and pollution aerosol effect on cloud cover. Science, 313(5787), 655-658. https://doi.org/10.1126/science.1126232

Kaufman, Y. J., Koren, I., Remer, L. A., Rosenfeld, D., & Rudich, Y. (2005). The effect of smoke, dust, and pollution aerosol on shallow cloud development over the Atlantic Ocean. Proceedings of the National Academy of Sciences of the United States of America, 102(32), 11207-11212. https://doi.org/10.1073/pnas.0505191102

Kerminen, V. M., Anttila, T., Lehtinen, K. E. J., & Kulmala, M. (2004). Parameterization for atmospheric new-particle formation: Application to a system involving sulfuric acid and condensable water-soluble organic vapors. Aerosol Science and Technology, 38(10), 1001-1008. https://doi.org/10.1080/027868290519085

Khain, A., Rosenfeld, D., & Pokrovsky, A. (2005). Aerosol impact on the dynamics and microphysics of deep convective clouds. Quarterly Journal of the Royal Meteorological Society, 131(611), 2639-2663. https://doi.org/10.1256/qj.04.62

Khain, A. P., Phillips, V., Benmoshe, N., & Pokrovsky, A. (2012). The Role of Small Soluble Aerosols in the Microphysics of Deep Maritime Clouds. Journal of the Atmospheric Sciences, 69(9), 2787-2807. https://doi.org/10.1175/2011jas3649.1

Kirkby, J., Duplissy, J., Sengupta, K., Frege, C., Gordon, H., Williamson, C., Heinritzi, M., Simon, M., Yan, C., Almeida, J., Trostl, J., Nieminen, T., Ortega, I. K., Wagner, R.,

Adamov, A., Amorim, A., Bernhammer, A. K., Bianchi, F., Breitenlechner, M., Brilke, S., Chen, X. M., Craven, J., Dias, A., Ehrhart, S., Flagan, R. C., Franchin, A., Fuchs, C., Guida, R., Hakala, J., Hoyle, C. R., Jokinen, T., Junninen, H., Kangasluoma, J., Kim, J., Krapf, M., Kurten, A., Laaksonen, A., Lehtipalo, K., Makhmutov, V., Mathot, S., Molteni, U., Onnela, A., Perakyla, O., Piel, F., Petaja, T., Praplan, A. P., Pringle, K., Rap, A., Richards, N. A. D., Riipinen, I., Rissanen, M. P., Rondo, L., Sarnela, N., Schobesberger, S., Scott, C. E., Seinfeld, J. H., Sipila, M., Steiner, G., Stozhkov, Y., Stratmann, F., Tome, A., Virtanen, A., Vogel, A. L., Wagner, A. C., Wagner, P. E., Weingartner, E., Wimmer, D., Winkler, P. M., Ye, P. L., Zhang, X., Hansel, A., Dommen, J., Donahue, N. M., Worsnop, D. R., Baltensperger, U., Kulmala, M., Carslaw, K. S., & Curtius, J. (2016). Ion-induced nucleation of pure biogenic particles. Nature, 533(7604), 521. https://doi.org/10.1038/nature17953

Koch, D., & Del Genio, A. D. (2010). Black carbon semi-direct effects on cloud cover: review and synthesis. Atmospheric Chemistry and Physics, 10(16), 7685-7696. https://doi.org/10.5194/acp-10-7685-2010

Kogan, Y. L., Mechem, D. B., & Choi, K. (2012). Effects of Sea-Salt Aerosols on Precipitation in Simulations of Shallow Cumulus. Journal of the Atmospheric Sciences, 69(2), 463-483. https://doi.org/10.1175/jas-d-11-031.1

Kohler, H. (1936). The nucleus in and the growth of hygroscopic droplets. Transactions of the Faraday Society, 32(2), 1152-1161. https://doi.org/10.1039/tf9363201152

Kolusu, S. R., Marsham, J. H., Mulcahy, J., Johnson, B., Dunning, C., Bush, M., & Spracklen, D. V. (2015). Impacts of Amazonia biomass burning aerosols assessed from short-range weather forecasts. Atmospheric Chemistry and Physics, 15(21), 12251-12266. https://doi.org/10.5194/acp-15-12251-2015

Koren, I., Kaufman, Y. J., Remer, L. A., & Martins, J. V. (2004). Measurement of the effect of Amazon smoke on inhibition of cloud formation. Science, 303(5662), 1342-1345. https://doi.org/10.1126/science.1089424

Koren, I., Martins, J. V., Remer, L. A., & Afargan, H. (2008). Smoke invigoration versus inhibition of clouds over the Amazon. Science, 321(5891), 946-949. https://doi.org/10.1126/science.1159185

Koren, I., Remer, L. A., Altaratz, O., Martins, J. V., & Davidi, A. (2010). Aerosol-induced changes of convective cloud anvils produce strong climate warming. Atmospheric Chemistry and Physics, 10(10), 5001-5010. https://doi.org/10.5194/acp-10-5001-2010

Krejci, R., Strom, J., de Reus, M., Williams, J., Fischer, H., Andreae, M. O., & Hansson, H. C. (2005). Spatial and temporal distribution of atmospheric aerosols in the lowermost troposphere over the Amazonian tropical rainforest. Atmospheric Chemistry and Physics, 5, 1527-1543. https://doi.org/10.5194/acp-5-1527-2005

Krishnakumar, V., Satyanarayana, M., Radhakrishnan, S. R., Dhaman, R. K., Pillai, V. P. M., Raghunath, K., Ratnam, M. V., Rao, D. R., & Sudhakar, P. (2011). Investigations on the physical and optical properties of cirrus clouds and their relationship with ice nuclei concentration using LIDAR at Gadanki, India (13.5 degrees N, 79.2 degrees E). Journal of Applied Remote Sensing, 5, 14, Article 053567. https://doi.org/10.1117/1.3662877

Kroll, J. H., Ng, N. L., Murphy, S. M., Flagan, R. C., & Seinfeld, J. H. (2005). Secondary organic aerosol formation from isoprene photooxidation under high-NOx conditions. Geophysical Research Letters, 32(18), 4, Article L18808. https://doi.org/10.1029/2005gl023637

Kuhn, U., Ganzeveld, L., Thielmann, A., Dindorf, T., Schebeske, G., Welling, M., Sciare, J., Roberts, G., Meixner, F. X., Kesselmeier, J., Lelieveld, J., Kolle, O., Ciccioli, P., Lloyd, J., Trentmann, J., Artaxo, P., & Andreae, M. O. (2010). Impact of Manaus City on the Amazon Green Ocean atmosphere: ozone production, precursor sensitivity and aerosol load. Atmospheric Chemistry and Physics, 10(19), 9251-9282. https://doi.org/10.5194/acp-10-9251-2010

Kulmala, M. (2003). How particles nucleate and grow. Science, 302(5647), 1000-1001. https://doi.org/10.1126/science.1090848

Kulmala, M., Kerminen, V. M., Anttila, T., Laaksonen, A., & O'Dowd, C. D. (2004). Organic aerosol formation via sulphate cluster activation. Journal of Geophysical Research-Atmospheres, 109(D4), 7, Article D04205. https://doi.org/10.1029/2003jd003961

Kulmala, M., Reissell, A., Sipila, M., Bonn, B., Ruuskanen, T. M., Lehtinen, K. E. J., Kerminen, V. M., & Strom, J. (2006). Deep convective clouds as aerosol production engines: Role of insoluble organics. Journal of Geophysical Research-Atmospheres, 111(D17), 7, Article D17202. https://doi.org/10.1029/2005jd006963

Lee, H. H., Chen, S. H., Kleeman, M. J., Zhang, H. L., DeNero, S. P., & Joe, D. K. (2016). Implementation of warm-cloud processes in a source- oriented WRF/Chem model to study the effect of aerosol mixing state on fog formation in the Central Valley of California. Atmospheric Chemistry and Physics, 16(13), 8353-8374. https://doi.org/10.5194/acp-16-8353-2016

Lee, S. S., Kim, B. G., Lee, C., Yum, S. S., & Posselt, D. (2014). Effect of aerosol pollution on clouds and its dependence on precipitation intensity. Climate Dynamics, 42(3-4), 557-577. https://doi.org/10.1007/s00382-013-1898-2

Lelieveld, J., Butler, T. M., Crowley, J. N., Dillon, T. J., Fischer, H., Ganzeveld, L., Harder, H., Lawrence, M. G., Martinez, M., Taraborrelli, D., & Williams, J. (2008). Atmospheric oxidation capacity sustained by a tropical forest. Nature, 452(7188), 737-740. https://doi.org/10.1038/nature06870

Levin, Z., & Cotton, W. R. (2009). Aerosol Pollution Impact on Precipitation: A Scientific Review. Springer. Berlin.

Lin, J. C., Matsui, T., Pielke, R. A., & Kummerow, C. (2006). Effects of biomass-burning-derived aerosols on precipitation and clouds in the Amazon Basin: a satellite-based empirical study. Journal of Geophysical Research-Atmospheres, 111(D19), 14, Article D19204. https://doi.org/10.1029/2005jd006884

Lin, Y., Wang, Y., Pan, B. W., Hu, J. X., Liu, Y. G., & Zhang, R. Y. (2016). Distinct Impacts of Aerosols on an Evolving Continental Cloud Complex during the RACORO Field Campaign. Journal of the Atmospheric Sciences, 73(9), 3681-3700. https://doi.org/10.1175/jas-d-15-0361.1

Lin, Y. L., Farley, R. D., & Orville, H. D. (1983). BULK PARAMETERIZATION OF THE SNOW FIELD IN A CLOUD MODEL. Journal of Climate and Applied Meteorology, 22(6), 1065-1092. https://doi.org/10.1175/1520-0450(1983)022<1065:Bpotsf>2.0.Co;2

Liu, Y. G., Daum, P. H., & McGraw, R. L. (2005). Size truncation effect, threshold behavior, and a new type of autoconversion parameterization. Geophysical Research Letters, 32(11), 5, Article L11811. https://doi.org/10.1029/2005gl022636

Lu, C. G., Schultz, P., & Browning, G. L. (2002). Scaling the microphysics equations and analyzing the variability of hydrometeor production rates in a controlled parameter space. Advances in Atmospheric Sciences, 19(4), 619-650. https://doi.org/10.1007/s00376-002-0004-1

Malhi, Y., Wood, D., Baker, T. R., Wright, J., Phillips, O. L., Cochrane, T., Meir, P., Chave, J., Almeida, S., Arroyo, L., Higuchi, N., Killeen, T. J., Laurance, S. G., Laurance, W. F., Lewis, S. L., Monteagudo, A., Neill, D. A., Vargas, P. N., Pitman, N. C. A., Quesada, C. A., Salomao, R., Silva, J. N. M., Lezama, A. T., Terborgh, J., Martinez, R. V., & Vinceti, B. (2006). The regional variation of aboveground live biomass in

old-growth Amazonian forests. Global Change Biology, 12(7), 1107-1138. https://doi.org/10.1111/j.1365-2486.2006.01120.x

Mann, G. W., Carslaw, K. S., Ridley, D. A., Spracklen, D. V., Pringle, K. J., Merikanto, J., Korhonen, H., Schwarz, J. P., Lee, L. A., Manktelow, P. T., Woodhouse, M. T., Schmidt, A., Breider, T. J., Emmerson, K. M., Reddington, C. L., Chipperfield, M. P., & Pickering, S. J. (2012). Intercomparison of modal and sectional aerosol microphysics representations within the same 3-D global chemical transport model. Atmospheric Chemistry and Physics, 12(10), 4449-4476. https://doi.org/10.5194/acp-12-4449-2012

Mao, J. H., Ping, F., Yin, L., & Qiu, X. F. (2018). A Study of Cloud Microphysical Processes Associated With Torrential Rainfall Event Over Beijing. Journal of Geophysical Research-Atmospheres, 123(16), 8768-8791. https://doi.org/10.1029/2018jd028490

Martin, S. T., Andreae, M. O., Artaxo, P., Baumgardner, D., Chen, Q., Goldstein, A. H., Guenther, A., Heald, C. L., Mayol-Bracero, O. L., McMurry, P. H., Pauliquevis, T., Pöschl, U., Prather, K. A., Roberts, G. C., Saleska, S. R., Dias, M. A. S., Spracklen, D. V., Swietlicki, E., & Trebs, I. (2010). SOURCES AND PROPERTIES OF AMAZONIAN AEROSOL PARTICLES. Reviews of Geophysics, 48, 42, Article Rg2002. https://doi.org/10.1029/2008rg000280

Martinez, I. R., & Chaboureau, J. P. (2018). Precipitation and Mesoscale Convective Systems: Radiative Impact of Dust over Northern Africa. Monthly Weather Review, 146(9), 3011-3029. https://doi.org/10.1175/mwr-d-18-0103.1

Martins, J. A., Dias, M., & Goncalves, F. L. T. (2009). Impact of biomass burning aerosols on precipitation in the Amazon: A modeling case study. Journal of Geophysical Research-Atmospheres, 114, 19, Article D02207. https://doi.org/10.1029/2007jd009587

McCluskey, C. S., DeMott, P. J., Prenni, A. J., Levin, E. J. T., McMeeking, G. R., Sullivan, A. P., Hill, T. C. J., Nakao, S., Carrico, C. M., & Kreidenweis, S. M. (2014). Characteristics of atmospheric ice nucleating particles associated with biomass burning in the US: Prescribed burns and wildfires. Journal of Geophysical Research-Atmospheres, 119(17), 13. https://doi.org/10.1002/2014jd021980

Metzger, A., Verheggen, B., Dommen, J., Duplissy, J., Prevot, A. S. H., Weingartner, E., Riipinen, I., Kulmala, M., Spracklen, D. V., Carslaw, K. S., & Baltensperger, U. (2010). Evidence for the role of organics in aerosol particle formation under atmospheric conditions. Proceedings of the National Academy of Sciences of the

United States of America, 107(15), 6646-6651. https://doi.org/10.1073/pnas.0911330107

Mlawer, E. J., Taubman, S. J., Brown, P. D., Iacono, M. J., & Clough, S. A. (1997). Radiative transfer for inhomogeneous atmospheres: RRTM, a validated correlated-k model for the longwave. Journal of Geophysical Research-Atmospheres, 102(D14), 16663-16682. https://doi.org/10.1029/97jd00237

Morrison, H., & Grabowski, W. W. (2011). Cloud-system resolving model simulations of aerosol indirect effects on tropical deep convection and its thermodynamic environment. Atmospheric Chemistry and Physics, 11(20), 10503-10523. https://doi.org/10.5194/acp-11-10503-2011

Nobre, P., Malagutti, M., Urbano, D. F., de Almeida, R. A. F., & Giarolla, E. (2009). Amazon Deforestation and Climate Change in a Coupled Model Simulation. Journal of Climate, 22(21), 5686-5697. https://doi.org/10.1175/2009jcli2757.1

Nobre, P., & Shukla, J. (1996). Variations of sea surface temperature, wind stress, and rainfall over the tropical Atlantic and South America. Journal of Climate, 9(10), 2464-2479. https://doi.org/10.1175/1520-0442(1996)009<2464:Vosstw>2.0.Co;2

Norris, J. R. (2001). Has northern Indian Ocean cloud cover changed due to increasing anthropogenic aerosol?. Geophysical Research Letters, 28(17), 3271-3274. https://doi.org/10.1029/2001gl013547

Otte, T. L., Nolte, C. G., Otte, M. J., & Bowden, J. H. (2012). Does Nudging Squelch the Extremes in Regional Climate Modeling?. Journal of Climate, 25(20), 7046-7066. https://doi.org/10.1175/jcli-d-12-00048.1

Paluch, I. R., & Baumgardner, D. G. (1989). ENTRAINMENT AND FINE-SCALE MIXING IN A CONTINENTAL CONVECTIVE CLOUD. Journal of the Atmospheric Sciences, 46(2), 261-278. https://doi.org/10.1175/1520-0469(1989)046<0261:Eafsmi>2.0.Co;2

Pan, X. H., Ichoku, C., Chin, M., Bian, H. S., Darmenov, A., Colarco, P., Ellison, L., Kucsera, T., da Silva, A., Wang, J., Oda, T., & Cui, G. (2020). Six global biomass burning emission datasets: intercomparison and application in one global aerosol model. Atmospheric Chemistry and Physics, 20(2), 969-994. https://doi.org/10.5194/acp-20-969-2020

Peng, J. F., Hu, M., Guo, S., Du, Z. F., Zheng, J., Shang, D. J., Zamora, M. L., Zeng, L. M., Shao, M., Wu, Y. S., Zheng, J., Wang, Y., Glen, C. R., Collins, D. R., Molina, M. J., & Zhang, R. Y. (2016). Markedly enhanced absorption and direct radiative forcing of

black carbon under polluted urban environments. Proceedings of the National Academy of Sciences of the United States of America, 113(16), 4266-4271. https://doi.org/10.1073/pnas.1602310113

Petersen, W. A., & Rutledge, S. A. (2001). Regional variability in tropical convection: Observations from TRMM. Journal of Climate, 14(17), 3566-3586. https://doi.org/10.1175/1520-0442(2001)014<3566:Rvitco>2.0.Co;2

Petty, G. W. (1999). Prevalence of precipitation from warm-topped clouds over eastern Asia and the western Pacific. Journal of Climate, 12(1), 220-229. https://doi.org/10.1175/1520-0442-12.1.220

Phillips, V. T. J., Andronache, C., Sherwood, S. C., Bansemer, A., Conant, W. C., Demott, P. J., Flagan, R. C., Heymsfield, A., Jonsson, H., Poellot, M., Rissman, T. A., Seinfeld, J. H., Vanreken, T., Varutbangkul, V., & Wilson, J. C. (2005). Anvil glaciation in a deep cumulus updraught over Florida simulated with the Explicit Microphysics Model. I: Impact of various nucleation processes. Quarterly Journal of the Royal Meteorological Society, 131(609), 2019-2046. https://doi.org/10.1256/qj.04.85

Phillips, V. T. J., Donner, L. J., & Garner, S. T. (2007). Nucleation processes in deep convection simulated by a cloud-system-resolving model with double-moment bulk microphysics. Journal of the Atmospheric Sciences, 64(3), 738-761. https://doi.org/10.1175/jas3869.1

Pincus, R., Barker, H. W., & Morcrette, J. J. (2003). A fast, flexible, approximate technique for computing radiative transfer in inhomogeneous cloud fields. Journal of Geophysical Research-Atmospheres, 108(D13), 5, Article 4376. https://doi.org/10.1029/2002jd003322

Planche, C., Wobrock, W., Flossmann, A. I., Tridon, F., Van Baelen, J., Pointin, Y., & Hagen, M. (2010). The influence of aerosol particle number and hygroscopicity on the evolution of convective cloud systems and their precipitation: A numerical study based on the COPS observations on 12 August 2007. Atmospheric Research, 98(1), 40-56. https://doi.org/10.1016/j.atmosres.2010.05.003

Platnick, S., & Twomey, S. (1994). DETERMINING THE SUSCEPTIBILITY OF CLOUD ALBEDO TO CHANGES IN DROPLET CONCENTRATION WITH THE ADVANCED VERY HIGH-RESOLUTION RADIOMETER. Journal of Applied Meteorology, 33(3), 334-347. https://doi.org/10.1175/1520-0450(1994)033<0334:Dtsoca>2.0.Co;2

Pöhlker, M. L., Ditas, F., Saturno, J., Klimach, T., de Angelis, I. H., Araujo, A. C., Brito, J., Carbone, S., Cheng, Y. F., Chi, X. G., Ditz, R., Gunthe, S. S., Holanda, B. A., Kandler, K., Kesselmeier, J., Konemann, T., Kruger, O. O., Lavric, J. V., Martin, S. T., Mikhailov, E., Moran-Zuloaga, D., Rizzo, L. V., Rose, D., Su, H., Thalman, R., Walter, D., Wang, J., Wolff, S., Barbosa, H. M. J., Artaxo, P., Andreae, M. O., Pöschl, U., & Pöhlker, C. (2018). Long-term observations of cloud condensation nuclei over the Amazon rain forest - Part 2: Variability and characteristics of biomass burning, long-range transport, and pristine rain forest aerosols. Atmospheric Chemistry and Physics, 18(14), 10289-10331. https://doi.org/10.5194/acp-18-10289-2018

Pöhlker, M. L., Pöhlker, C., Ditas, F., Klimach, T., de Angelis, I. H., Araujo, A., Brito, J., Carbone, S., Cheng, Y. F., Chi, X. G., Ditz, R., Gunthe, S. S., Kesselmeier, J., Konemann, T., Lavric, J. V., Martin, S. T., Mikhailov, E., Moran-Zuloaga, D., Rose, D., Saturno, J., Su, H., Thalman, R., Walter, D., Wang, J., Wolff, S., Barbosa, H. M. J., Artaxo, P., Andreae, M. O., & Pöschl, U. (2016). Long-term observations of cloud condensation nuclei in the Amazon rain forest - Part 1: Aerosol size distribution, hygroscopicity, and new model parametrizations for CCN prediction. Atmospheric Chemistry and Physics, 16(24), 15709-15740. https://doi.org/10.5194/acp-16-15709-2016

Pontikis, C. A., & Hicks, E. M. (1993). DROPLET ACTIVATION AS RELATED TO ENTRAINMENT AND MIXING IN WARM TROPICAL MARITIME CLOUDS. Journal of the Atmospheric Sciences, 50(13), 1888-1896. https://doi.org/10.1175/1520-0469(1993)050<1888:Daarte>2.0.Co;2

Pöschl, U., Martin, S. T., Sinha, B., Chen, Q., Gunthe, S. S., Huffman, J. A., Borrmann, S., Farmer, D. K., Garland, R. M., Helas, G., Jimenez, J. L., King, S. M., Manzi, A., Mikhailov, E., Pauliquevis, T., Petters, M. D., Prenni, A. J., Roldin, P., Rose, D., Schneider, J., Su, H., Zorn, S. R., Artaxo, P., & Andreae, M. O. (2010). Rainforest Aerosols as Biogenic Nuclei of Clouds and Precipitation in the Amazon. Science, 329(5998), 1513-1516. https://doi.org/10.1126/science.1191056

Prenni, A. J., Petters, M. D., Kreidenweis, S. M., Heald, C. L., Martin, S. T., Artaxo, P., Garland, R. M., Wollny, A. G., & Pöschl, U. (2009). Relative roles of biogenic emissions and Saharan dust as ice nuclei in the Amazon basin. Nature Geoscience, 2(6), 401-404. https://doi.org/10.1038/ngeo517

Procopio, A. S., Artaxo, P., Kaufman, Y. J., Remer, L. A., Schafer, J. S., & Holben, B. N. (2004). Multiyear analysis of amazonian biomass burning smoke radiative forcing of climate. Geophysical Research Letters, 31(3), 4, Article L03108. https://doi.org/10.1029/2003gl018646

Pruppacher, H.R. & Klett, J.D. (2010). Microphysics of clouds and precipitation. Springer. New York.

Ramachandran, S., & Kedia, S. (2010). Black carbon aerosols over an urban region: Radiative forcing and climate impact. Journal of Geophysical Research-Atmospheres, 115, 11, Article D10202. https://doi.org/10.1029/2009jd013560

Ramanathan, V., & Carmichael, G. (2008). Global and regional climate changes due to black carbon. Nature Geoscience, 1(4), 221-227. https://doi.org/10.1038/ngeo156

Rasmussen, R. A., & Khalil, M. A. K. (1988). ISOPRENE OVER THE AMAZON BASIN. Journal of Geophysical Research-Atmospheres, 93(D2), 1417-1421. https://doi.org/10.1029/JD093iD02p01417

Reddington, C. L., Morgan, W. T., Darbyshire, E., Brito, J., Coe, H., Artaxo, P., Scott, C. E., Marsham, J., & Spracklen, D. V. (2019). Biomass burning aerosol over the Amazon: analysis of aircraft, surface and satellite observations using a global aerosol model. Atmospheric Chemistry and Physics, 19(14), 9125-9152. https://doi.org/10.5194/acp-19-9125-2019

Reid, J. S., Koppmann, R., Eck, T. F., & Eleuterio, D. P. (2005). A review of biomass burning emissions part II: intensive physical properties of biomass burning particles. Atmospheric Chemistry and Physics, 5, 799-825. https://doi.org/10.5194/acp-5-799-2005

Reutter, P., Su, H., Trentmann, J., Simmel, M., Rose, D., Gunthe, S. S., Wernli, H., Andreae, M. O., & Pöschl, U. (2009). Aerosol- and updraft-limited regimes of cloud droplet formation: influence of particle number, size and hygroscopicity on the activation of cloud condensation nuclei (CCN). Atmospheric Chemistry and Physics, 9(18), 7067-7080. https://doi.org/10.5194/acp-9-7067-2009

Riccobono, F., Schobesberger, S., Scott, C. E., Dommen, J., Ortega, I. K., Rondo, L., Almeida, J., Amorim, A., Bianchi, F., Breitenlechner, M., David, A., Downard, A., Dunne, E. M., Duplissy, J., Ehrhart, S., Flagan, R. C., Franchin, A., Hansel, A., Junninen, H., Kajos, M., Keskinen, H., Kupc, A., Kurten, A., Kvashin, A. N., Laaksonen, A., Lehtipalo, K., Makhmutov, V., Mathot, S., Nieminen, T., Onnela, A., Petaja, T., Praplan, A. P., Santos, F. D., Schallhart, S., Seinfeld, J. H., Sipila, M.,

Spracklen, D. V., Stozhkov, Y., Stratmann, F., Tome, A., Tsagkogeorgas, G., Vaattovaara, P., Viisanen, Y., Vrtala, A., Wagner, P. E., Weingartner, E., Wex, H., Wimmer, D., Carslaw, K. S., Curtius, J., Donahue, N. M., Kirkby, J., Kulmala, M., Worsnop, D. R., & Baltensperger, U. (2014). Oxidation Products of Biogenic Emissions Contribute to Nucleation of Atmospheric Particles. Science, 344(6185), 717-721. https://doi.org/10.1126/science.1243527

Rickenbach, T. M. (2004). Nocturnal cloud systems and the diurnal variation of clouds and rainfall in southwestern Amazonia. Monthly Weather Review, 132(5), 1201-1219. https://doi.org/10.1175/1520-0493(2004)132<1201:Ncsatd>2.0.Co;2

Rissler, J., Vestin, A., Swietlicki, E., Fisch, G., Zhou, J., Artaxo, P., & Andreae, M. O. (2006). Size distribution and hygroscopic properties of aerosol particles from dry-season biomass burning in Amazonia. Atmospheric Chemistry and Physics, 6, 471-491. https://doi.org/10.5194/acp-6-471-2006

Rizzo, L. V., Artaxo, P., Muller, T., Wiedensohler, A., Paixao, M., Cirino, G. G., Arana, A., Swietlicki, E., Roldin, P., Fors, E. O., Wiedemann, K. T., Leal, L. S. M., & Kulmala, M. (2013). Long term measurements of aerosol optical properties at a primary forest site in Amazonia. Atmospheric Chemistry and Physics, 13(5), 2391-2413. https://doi.org/10.5194/acp-13-2391-2013

Roberts, G. C., Nenes, A., Seinfeld, J. H., & Andreae, M. O. (2003). Impact of biomass burning on cloud properties in the Amazon Basin. Journal of Geophysical Research-Atmospheres, 108(D2), 19, Article 4062. https://doi.org/10.1029/2001jd000985

Ropelewski, C. F., & Halpert, M. S. (1987). GLOBAL AND REGIONAL SCALE PRECIPITATION PATTERNS ASSOCIATED WITH THE EL-NINO SOUTHERN OSCILLATION. Monthly Weather Review, 115(8), 1606-1626. https://doi.org/10.1175/1520-0493(1987)115<1606:Garspp>2.0.Co;2

Rosario, N. E., Longo, K. M., Freitas, S. R., Yamasoe, M. A., & Fonseca, R. M. (2013). Modeling the South American regional smoke plume: aerosol optical depth variability and surface shortwave flux perturbation. Atmospheric Chemistry and Physics, 13(6), 2923-2938. https://doi.org/10.5194/acp-13-2923-2013

Rosenfeld, D., Lohmann, U., Raga, G. B., O'Dowd, C. D., Kulmala, M., Fuzzi, S., Reissell, A., & Andreae, M. O. (2008). Flood or drought: How do aerosols affect precipitation? Science, 321(5894), 1309-1313. https://doi.org/10.1126/science.1160606

Rutledge, S. A., & Hobbs, P. V. (1984). THE MESOSCALE AND MICROSCALE STRUCTURE AND ORGANIZATION OF CLOUDS AND PRECIPITATION IN

MIDLATITUDE CYCLONES .12. A DIAGNOSTIC MODELING STUDY OF PRECIPITATION DEVELOPMENT IN NARROW COLD-FRONTAL RAINBANDS. Journal of the Atmospheric Sciences, 41(20), 2949-2972. https://doi.org/10.1175/1520-0469(1984)041<2949:Tmamsa>2.0.Co;2

Saathoff, H., Naumann, K. H., Mohler, O., Jonsson, A. M., Hallquist, M., Kiendler-Scharr, A., Mentel, T. F., Tillmann, R., & Schurath, U. (2009). Temperature dependence of yields of secondary organic aerosols from the ozonolysis of alpha-pinene and limonene. Atmospheric Chemistry and Physics, 9(5), 1551-1577. https://doi.org/10.5194/acp-9-1551-2009

Saide, P. E., Spak, S. N., Pierce, R. B., Otkin, J. A., Schaack, T. K., Heidinger, A. K., da Silva, A. M., Kacenelenbogen, M., Redemann, J., & Carmichael, G. R. (2015). Central American biomass burning smoke can increase tornado severity in the US. Geophysical Research Letters, 42(3), 956-965. https://doi.org/10.1002/2014gl062826

Saturno, J., Holanda, B. A., Pöhlker, C., Ditas, F., Wang, Q. Q., Moran-Zuloaga, D., Brito, J., Carbone, S., Cheng, Y. F., Chi, X. G., Ditas, J., Hoffmann, T., de Angelis, I. H., Konemann, T., Lavric, J. V., Ma, N., Ming, J., Paulsen, H., Pöhlker, M. L., Rizzo, L. V., Schlag, P., Su, H., Walter, D., Wolff, S., Zhang, Y. X., Artaxo, P., Pöschl, U., & Andreae, M. O. (2018). Black and brown carbon over central Amazonia: long-term aerosol measurements at the ATTO site. Atmospheric Chemistry and Physics, 18(17), 12817-12843. https://doi.org/10.5194/acp-18-12817-2018

Schell, B., Ackermann, I. J., Hass, H., Binkowski, F. S., & Ebel, A. (2001). Modeling the formation of secondary organic aerosol within a comprehensive air quality model system. Journal of Geophysical Research-Atmospheres, 106(D22), 28275-28293. https://doi.org/10.1029/2001jd000384

Schulz, C., Schneider, J., Holanda, B. A., Appel, O., Costa, A., de Sa, S. S., Dreiling, V., Futterer, D., Jurkat-Witschas, T., Klimach, T., Knote, C., Kramer, M., Martin, S. T., Mertes, S., Pöhlker, M. L., Sauer, D., Voigt, C., Walser, A., Weinzierl, B., Ziereis, H., Zoger, M., Andreae, M. O., Artaxo, P., Machado, L. A. T., Pöschl, U., Wendisch, M., & Borrmann, S. (2018). Aircraft-based observations of isoprene-epoxydiol-derived secondary organic aerosol (IEPOX-SOA) in the tropical upper troposphere over the Amazon region. Atmospheric Chemistry and Physics, 18(20), 14979-15001. https://doi.org/10.5194/acp-18-14979-2018

Schumacher, C., & Houze, R. A. (2003). The TRMM precipitation radar's view of shallow, isolated rain. Journal of Applied Meteorology, 42(10), 1519-1524. https://doi.org/10.1175/1520-0450(2003)042<1519:Ttprvo>2.0.Co;2

Scott, C. E., Rap, A., Spracklen, D. V., Forster, P. M., Carslaw, K. S., Mann, G. W., Pringle, K. J., Kivekas, N., Kulmala, M., Lihavainen, H., & Tunved, P. (2014). The direct and indirect radiative effects of biogenic secondary organic aerosol. Atmospheric Chemistry and Physics, 14(1), 447-470. https://doi.org/10.5194/acp-14-447-2014

Seinfeld, J. H. & Pandis, S. N. (2016). Atmospheric chemistry and physics: from air pollution to climate change. Wiley & Sons. Hoboken, New Jersey.

Sena, E. T., Artaxo, P., & Correia, A. L. (2013). Spatial variability of the direct radiative forcing of biomass burning aerosols and the effects of land use change in Amazonia. Atmospheric Chemistry and Physics, 13(3), 1261-1275. https://doi.org/10.5194/acp-13-1261-2013

Shi, J. J., Matsui, T., Tao, W. K., Tan, Q., Peters-Lidard, C., Chin, M., Pickering, K., Guy, N., Lang, S., & Kemp, E. M. (2014). Implementation of an aerosol-cloud-microphysics-radiation coupling into the NASA unified WRF: Simulation results for the 6-7 August 2006 AMMA special observing period. Quarterly Journal of the Royal Meteorological Society, 140(684), 2158-2175. https://doi.org/10.1002/qj.2286

Short, D. A., & Nakamura, K. (2000). TRMM radar observations of shallow precipitation over the tropical oceans. Journal of Climate, 13(23), 4107-4124. https://doi.org/10.1175/1520-0442(2000)013<4107:Troosp>2.0.Co;2

Shrivastava, M., Cappa, C. D., Fan, J. W., Goldstein, A. H., Guenther, A. B., Jimenez, J. L., Kuang, C., Laskin, A., Martin, S. T., Ng, N. L., Petaja, T., Pierce, J. R., Rasch, P. J., Roldin, P., Seinfeld, J. H., Shilling, J., Smith, J. N., Thornton, J. A., Volkamer, R., Wang, J., Worsnop, D. R., Zaveri, R. A., Zelenyuk, A., & Zhang, Q. (2017). Recent advances in understanding secondary organic aerosol: Implications for global climate forcing. Reviews of Geophysics, 55(2), 509-559. https://doi.org/10.1002/2016rg000540

Slawinska, J., Grabowski, W. W., Pawlowska, H., & Morrison, H. (2012). Droplet Activation and Mixing in Large-Eddy Simulation of a Shallow Cumulus Field. Journal of the Atmospheric Sciences, 69(2), 444-462. https://doi.org/10.1175/jas-d-11-054.1

Stevens, B., & Feingold, G. (2009). Untangling aerosol effects on clouds and precipitation in a buffered system. Nature, 461(7264), 607-613. https://doi.org/10.1038/nature08281

Streets, D. G. (2007). Dissecting future aerosol emissions: Warming tendencies and mitigation opportunities. Climatic Change, 81(3-4), 313-330. https://doi.org/10.1007/s10584-006-9112-8

Streets, D. G., Yarber, K. F., Woo, J. H., & Carmichael, G. R. (2003). Biomass burning in Asia: Annual and seasonal estimates and atmospheric emissions. Global Biogeochemical Cycles, 17(4), 20, Article 1099. https://doi.org/10.1029/2003gb002040

Su, H., Rose, D., Cheng, Y. F., Gunthe, S. S., Massling, A., Stock, M., Wiedensohler, A., Andreae, M. O., & Pöschl, U. (2010). Hygroscopicity distribution concept for measurement data analysis and modeling of aerosol particle mixing state with regard to hygroscopic growth and CCN activation. Atmospheric Chemistry and Physics, 10(15), 7489-7503. https://doi.org/10.5194/acp-10-7489-2010

Su, L., & Fung, J. C. H. (2018). Investigating the role of dust in ice nucleation within clouds and further effects on the regional weather system over East Asia - Part 1: model development and validation. Atmospheric Chemistry and Physics, 18(12), 8707-8725. https://doi.org/10.5194/acp-18-8707-2018

Sui, C. H., Lau, K. M., Tao, W. K., & Simpson, J. (1994). THE TROPICAL WATER AND ENERGY CYCLES IN A CUMULUS ENSEMBLE MODEL .1. EQUILIBRIUM CLIMATE. Journal of the Atmospheric Sciences, 51(5), 711-728. https://doi.org/10.1175/1520-0469(1994)051<0711:Ttwaec>2.0.Co;2

Suzuki, K., Stephens, G. L., & Lebsock, M. D. (2013). Aerosol effect on the warm rain formation process: Satellite observations and modeling. Journal of Geophysical Research-Atmospheres, 118(1), 170-184. https://doi.org/10.1002/jgrd.50043

Tackett, J. L., Winker, D. M., Getzewich, B. J., Vaughan, M. A., Young, S. A., & Kar, J. (2018). CALIPSO lidar level 3 aerosol profile product: version 3 algorithm design. Atmospheric Measurement Techniques, 11(7), 4129-4152. https://doi.org/10.5194/amt-11-4129-2018

Tanaka, L., Satyamurty, P., & Machado, L. A. T. (2014). Diurnal variation of precipitation in central Amazon Basin. International Journal of Climatology, 34(13), 3574-3584. https://doi.org/10.1002/joc.3929

Tao, W. K., Chen, J. P., Li, Z. Q., Wang, C., & Zhang, C. D. (2012). IMPACT OF AEROSOLS ON CONVECTIVE CLOUDS AND PRECIPITATION. Reviews of Geophysics, 50, 62, Article Rg2001. https://doi.org/10.1029/2011rg000369

Tegen, I., Hollrig, P., Chin, M., Fung, I., Jacob, D., & Penner, J. (1997). Contribution of different aerosol species to the global aerosol extinction optical thickness: Estimates from model results. Journal of Geophysical Research-Atmospheres, 102(D20), 23895-23915. https://doi.org/10.1029/97jd01864

Teller, A., & Levin, Z. (2006). The effects of aerosols on precipitation and dimensions of subtropical clouds: a sensitivity study using a numerical cloud model. Atmospheric Chemistry and Physics, 6, 67-80. https://doi.org/10.5194/acp-6-67-2006

Ten Hoeve, J. E., Jacobson, M. Z., & Remer, L. A. (2012). Comparing results from a physical model with satellite and in situ observations to determine whether biomass burning aerosols over the Amazon brighten or burn off clouds. Journal of Geophysical Research-Atmospheres, 117, 19, Article D08203. https://doi.org/10.1029/2011jd016856

Thornhill, G. D., Ryder, C. L., Highwood, E. J., Shaffrey, L. C., & Johnson, B. T. (2018). The effect of South American biomass burning aerosol emissions on the regional climate. Atmospheric Chemistry and Physics, 18(8), 5321-5342. https://doi.org/10.5194/acp-18-5321-2018

Trostl, J., Chuang, W. K., Gordon, H., Heinritzi, M., Yan, C., Molteni, U., Ahlm, L., Frege, C., Bianchi, F., Wagner, R., Simon, M., Lehtipalo, K., Williamson, C., Craven, J. S., Duplissy, J., Adamov, A., Almeida, J., Bernhammer, A. K., Breitenlechner, M., Brilke, S., Dias, A., Ehrhart, S., Flagan, R. C., Franchin, A., Fuchs, C., Guida, R., Gysel, M., Hansel, A., Hoyle, C. R., Jokinen, T., Junninen, H., Kangasluoma, J., Keskinen, H., Kim, J., Krapf, M., Kurten, A., Laaksonen, A., Lawler, M., Leiminger, M., Mathot, S., Mohler, O., Nieminen, T., Onnela, A., Petaja, T., Piel, F. M., Miettinen, P., Rissanen, M. P., Rondo, L., Sarnela, N., Schobesberger, S., Sengupta, K., Sipila, M., Smith, J. N., Steiner, G., Tome, A., Virtanen, A., Wagner, A. C., Weingartner, E., Wimmer, D., Winkler, P. M., Ye, P. L., Carslaw, K. S., Curtius, J., Dommen, J., Kirkby, J., Kulmala, M., Riipinen, I., Worsnop, D. R., Donahue, N. M., & Baltensperger, U. (2016). The role of low-volatility organic compounds in initial particle growth in the atmosphere. Nature, 533(7604), 527-+. https://doi.org/10.1038/nature18271

Twohy, C. H., Petters, M. D., Snider, J. R., Stevens, B., Tahnk, W., Wetzel, M., Russell, L., & Burnet, F. (2005). Evaluation of the aerosol indirect effect in marine stratocumulus clouds: Droplet number, size, liquid water path, and radiative impact. Journal of

Geophysical Research-Atmospheres, 110(D8), 16, Article D08203. https://doi.org/10.1029/2004jd005116

Twomey, S. (1977). INFLUENCE OF POLLUTION ON SHORTWAVE ALBEDO OF CLOUDS. Journal of the Atmospheric Sciences, 34(7), 1149-1152. https://doi.org/10.1175/1520-0469(1977)034<1149:Tiopot>2.0.Co;2

Uvo, C. B., Repelli, C. A., Zebiak, S. E., & Kushnir, Y. (1998). The relationships between tropical Pacific and Atlantic SST and northeast Brazil monthly precipitation. Journal of Climate, 11(4), 551-562. https://doi.org/10.1175/1520-0442(1998)011<0551:Trbtpa>2.0.Co;2

Wallace, J. M. & Hobbs, P. V. (2006). Atmospheric science: an introductory survey. Academic press.

Wang, H., & Fu, R. (2002). Cross-equatorial flow and seasonal cycle of precipitation over South America. Journal of Climate, 15(13), 1591-1608. https://doi.org/10.1175/1520-0442(2002)015<1591:Cefasc>2.0.Co;2

Wang, M., Ghan, S., Easter, R., Ovchinnikov, M., Liu, X., Kassianov, E., Qian, Y., Gustafson, W. I., Larson, V. E., Schanen, D. P., Khairoutdinov, M., & Morrison, H. (2011). The multi-scale aerosol-climate model PNNL-MMF: model description and evaluation. Geoscientific Model Development, 4(1), 137-168. https://doi.org/10.5194/gmd-4-137-2011

Wang, Y., Khalizov, A., Levy, M., & Zhang, R. Y. (2013). New Directions: Light absorbing aerosols and their atmospheric impacts. Atmospheric Environment, 81, 713-715. https://doi.org/10.1016/j.atmosenv.2013.09.034

Wang, Y., Ma, P. L., Peng, J. F., Zhang, R. Y., Jiang, J. H., Easter, R. C., & Yung, Y. L. (2018). Constraining Aging Processes of Black Carbon in the Community Atmosphere Model Using Environmental Chamber Measurements. Journal of Advances in Modeling Earth Systems, 10(10), 2514-2526. https://doi.org/10.1029/2018ms001387

Warner, J. (1969a). MICROSTRUCTURE OF CUMULUS CLOUD .2. EFFECT ON DROPLET SIZE DISTRIBUTION OF CLOUD NUCLEUS SPECTRUM AND UPDRAFT VELOCITY. Journal of the Atmospheric Sciences, 26(6), 1272-&. https://doi.org/10.1175/1520-0469(1969)026<1272:Tmoccp>2.0.Co;2

Warner, J. (1969b). MICROSTRUCTURE OF CUMULUS CLOUD .I. GENERAL FEATURES OF DROPLET SPECTRUM. Journal of the Atmospheric Sciences,

26(5P2), 1049-&. https://doi.org/10.1175/1520-0469(1969)026<1049:Tmoccp>2.0.Co;2

Watson-Parris, D., Schutgens, N., Reddington, C., Pringle, K. J., Liu, D. T., Allan, J. D., Coe, H., Carslaw, K. S., & Stier, P. (2019). In situ constraints on the vertical distribution of global aerosol. Atmospheric Chemistry and Physics, 19(18), 11765-11790. https://doi.org/10.5194/acp-19-11765-2019

Watson, L. A., Shallcross, D. E., Utembe, S. R., & Jenkin, M. E. (2008). A Common Representative Intermediates (CRI) mechanism for VOC degradation. Part 2: Gas phase mechanism reduction. Atmospheric Environment, 42(31), 7196-7204. https://doi.org/10.1016/j.atmosenv.2008.07.034

Wendisch, M., Pöschl, U., Andreae, M. O., Machado, L. A. T., Albrecht, R., Schlager, H., Rosenfeld, D., Martin, S. T., Abdelmomonem, A., Afchine, A., Araujo, A. C., Artaxo, P., Aufmhoff, H., Barbosa, H. M. J., Borrmann, S., Braga, R., Buchholz, B., Cecchini, M. A., Costa, A., Curtius, J., Dollner, M., Dorf, M., Dreiling, V., Ebert, V., Ehrlich, A., Ewald, F., Fisch, G., Fix, A., Frank, F., Futterer, D., Heckl, C., Heidelberg, F., Huneke, T., Jakel, E., Jarvinen, E., Jurkat, T., Kanter, S., Kastner, U., Kenntner, M., Kesselmeier, J., Klimach, T., Knecht, M., Kohl, R., Kolling, T., Kramer, M., Kruger, M., Krisna, T. C., Lavric, J. V., Longo, K., Mahnke, C., Manzi, A. O., Mayer, B., Mertes, S., Minikin, A., Molleker, S., Munch, S., Nillius, B., Pfeilsticker, K., Pöhlker, C., Roiger, A., Rose, D., Rosenowow, D., Sauer, D., Schnaiter, M., Schneider, J., Schulz, C., de Souza, R. A. F., Spanu, A., Stock, P., Vila, D., Voigt, C., Walser, A., Walter, D., Weigel, R., Weinzierl, B., Werner, F., Yamasoe, M. A., Ziereis, H., Zinner, T., & Zoger, M. (2016). ACRIDICON-CHUVA CAMPAIGN Studying Tropical Deep Convective Clouds and Precipitation over Amazonia Using the New German Research Aircraft HALO. Bulletin of the American Meteorological Society, 97(10), 1885-1908. https://doi.org/10.1175/bams-d-14-00255.1

Wexler, A. S., Lurmann, F. W., & Seinfeld, J. H. (1994). MODELING URBAN AND REGIONAL AEROSOLS .1. MODEL DEVELOPMENT. Atmospheric Environment, 28(3), 531-546. https://doi.org/10.1016/1352-2310(94)90129-5

Wiedinmyer, C., Akagi, S. K., Yokelson, R. J., Emmons, L. K., Al-Saadi, J. A., Orlando, J. J., & Soja, A. J. (2011). The Fire INventory from NCAR (FINN): a high resolution global model to estimate the emissions from open burning. Geoscientific Model Development, 4(3), 625-641. https://doi.org/10.5194/gmd-4-625-2011

Williams, E., Rosenfeld, D., Madden, N., Gerlach, J., Gears, N., Atkinson, L., Dunnemann, N., Frostrom, G., Antonio, M., Biazon, B., Camargo, R., Franca, H., Gomes, A., Lima, M., Machado, R., Manhaes, S., Nachtigall, L., Piva, H., Quintiliano, W., Machado, L., Artaxo, P., Roberts, G., Renno, N., Blakeslee, R., Bailey, J., Boccippio, D., Betts, A., Wolff, D., Roy, B., Halverson, J., Rickenbach, T., Fuentes, J., & Avelino, E. (2002). Contrasting convective regimes over the Amazon: Implications for cloud electrification. Journal of Geophysical Research-Atmospheres, 107(D20), 19, Article 8082. https://doi.org/10.1029/2001jd000380

Williamson, C. J., Kupc, A., Axisa, D., Bilsback, K. R., Bui, T., Campuzano-Jost, P., Dollner, M., Froyd, K. D., Hodshire, A. L., Jimenez, J. L., Kodros, J. K., Luo, G., Murphy, D. M., Nault, B. A., Ray, E. A., Weinzierl, B., Wilson, J. C., Yu, F. Q., Yu, P. F., Pierce, J. R., & Brock, C. A. (2019). A large source of cloud condensation nuclei from new particle formation in the tropics. Nature, 574(7778), 399. https://doi.org/10.1038/s41586-019-1638-9

Wright, J. S., Fu, R., Worden, J. R., Chakraborty, S., Clinton, N. E., Risi, C., Sun, Y., & Yin, L. (2017). Rainforest-initiated wet season onset over the southern Amazon. Proceedings of the National Academy of Sciences of the United States of America, 114(32), 8481-8486. https://doi.org/10.1073/pnas.1621516114

Wu, L. T., Su, H., & Jiang, J. H. (2011a). Regional simulations of deep convection and biomass burning over South America: 1. Model evaluations using multiple satellite data sets. Journal of Geophysical Research-Atmospheres, 116, 14, Article D17208. https://doi.org/10.1029/2011jd016105

Wu, L. T., Su, H., & Jiang, J. H. (2011b). Regional simulations of deep convection and biomass burning over South America: 2. Biomass burning aerosol effects on clouds and precipitation. Journal of Geophysical Research-Atmospheres, 116, 11, Article D17209. https://doi.org/10.1029/2011jd016106

Yang, G. Y., & Slingo, J. (2001). The diurnal cycle in the Tropics. Monthly Weather Review, 129(4), 784-801. https://doi.org/10.1175/1520-0493(2001)129<0784:Tdcitt>2.0.Co;2

Ye, X. Y., Cao, Q. M., Jiang, B. L., & Lin, W. S. (2019). Numerical Simulation of the Effect of Cloud Condensation Nuclei Concentration on the Microphysical Processes in Typhoon Usagi. Advances in Meteorology, 2019, 9, Article 8293062. https://doi.org/10.1155/2019/8293062

Yin, Y., Levin, Z., Reisin, T. G., & Tzivion, S. (2000). The effects of giant cloud condensation nuclei on the development of precipitation in convective clouds - a

numerical study. Atmospheric Research, 53(1-3), 91-116. https://doi.org/10.1016/s0169-8095(99)00046-0

Yu, F. Q., Luo, G., Nadykto, A. B., & Herb, J. (2017). Impact of temperature dependence on the possible contribution of organics to new particle formation in the atmosphere. Atmospheric Chemistry and Physics, 17(8), 4997-5005. https://doi.org/10.5194/acp-17-4997-2017

Zaveri, R. A., Easter, R. C., Fast, J. D., & Peters, L. K. (2008). Model for Simulating Aerosol Interactions and Chemistry (MOSAIC). Journal of Geophysical Research-Atmospheres, 113(D13), 29, Article D13204. https://doi.org/10.1029/2007jd008782

Zaveri, R. A., & Peters, L. K. (1999). A new lumped structure photochemical mechanism for large-scale applications. Journal of Geophysical Research-Atmospheres, 104(D23), 30387-30415. https://doi.org/10.1029/1999jd900876

Zhang, Y., Dubey, M. K., Olsen, S. C., Zheng, J., & Zhang, R. (2009). Comparisons of WRF/Chem simulations in Mexico City with ground-based RAMA measurements during the 2006-MILAGRO. Atmospheric Chemistry and Physics, 9(11), 3777-3798. https://doi.org/10.5194/acp-9-3777-2009

Zhang, Y., Fu, R., Yu, H. B., Dickinson, R. E., Juarez, R. N., Chin, M., & Wang, H. (2008). A regional climate model study of how biomass burning aerosol impacts land-atmosphere interactions over the Amazon. Journal of Geophysical Research-Atmospheres, 113(D14), 13, Article D14s15. https://doi.org/10.1029/2007jd009449

Zhang, Y., Fu, R., Yu, H. B., Qian, Y., Dickinson, R., Dias, M., Dias, P. L. D., & Fernandes, K. (2009). Impact of biomass burning aerosol on the monsoon circulation transition over Amazonia. Geophysical Research Letters, 36, 6, Article L10814. https://doi.org/10.1029/2009gl037180

Zhao, B., Shrivastava, M., Donahue, N. M., Gordon, H., Schervish, M., Shilling, J. E., . . . Fast, J. D. (2020). High concentration of ultrafine particles in the Amazon free troposphere produced by organic new particle formation. Proc Natl Acad Sci U S A, 117(41), 25344-25351. doi:10.1073/pnas.2006716117

Zhao, C., Leung, L. R., Easter, R., Hand, J., & Avise, J. (2013). Characterization of speciated aerosol direct radiative forcing over California. Journal of Geophysical Research-Atmospheres, 118(5), 2372-2388. https://doi.org/10.1029/2012jd018364

Zhu, J. L., & Penner, J. E. (2019). Global Modeling of Secondary Organic Aerosol With Organic Nucleation. Journal of Geophysical Research-Atmospheres, 124(14), 8260-8286. https://doi.org/10.1029/2019jd030414

Zhu, J. L., & Penner, J. E. (2020). Radiative forcing of anthropogenic aerosols on cirrus clouds using a hybrid ice nucleation scheme. Atmospheric Chemistry and Physics, 20(13), 7801-7827. https://doi.org/10.5194/acp-20-7801-2020

Zhu, J. L., Penner, J. E., Yu, F. Q., Sillman, S., Andreae, M. O., & Coe, H. (2019). Decrease in radiative forcing by organic aerosol nucleation, climate, and land use change. Nature Communications, 10, 7, Article 423. https://doi.org/10.1038/s41467-019-08407-7

Zhuang, Y. Z., Fu, R., Marengo, J. A., & Wang, H. Q. (2017). Seasonal variation of shallow-to-deep convection transition and its link to the environmental conditions over the Central Amazon. Journal of Geophysical Research-Atmospheres, 122(5), 2649-2666. https://doi.org/10.1002/2016jd025993

Zipser, E. J., & Lutz, K. R. (1994). THE VERTICAL PROFILE OF RADAR REFLECTIVITY OF CONVECTIVE CELLS - A STRONG INDICATOR OF STORM INTENSITY AND LIGHTNING PROBABILITY. Monthly Weather Review, 122(8), 1751-1759. https://doi.org/10.1175/1520-0493(1994)122<1751:Tvporr>2.0.Co;2